

# Important Notice

This copy may be used only for the purposes of research and private study, and any use of the copy for a purpose other than research or private study may require the authorization of the copyright owner of the work in question. Responsibility regarding questions of copyright that may arise in the use of this copy is assumed by the recipient.

UNIVERSITY OF CALGARY

Interpretation of 3D multicomponent seismic data for investigating natural fractures in  
the Horn River Basin, northeast British Columbia

by

Abdallah A. Al-Zahrani

A THESIS

SUBMITTED TO THE FACULTY OF GRADUATE STUDIES  
IN PARTIAL FULFILMENT OF THE REQUIREMENTS FOR THE  
DEGREE OF MASTER OF SCIENCE

DEPARTMENT OF GEOSCIENCE

CALGARY, ALBERTA

September, 2011

© Abdallah Al-Zahrani 2011

UNIVERSITY OF CALGARY  
FACULTY OF GRADUATE STUDIES

The undersigned certify that they have read, and recommend to the Faculty of Graduate Studies for acceptance, a thesis entitled "Interpretation of 3D multicomponent seismic data for investigating natural fractures in the Horn River Basin, northeast British Columbia" submitted by Abdallah Al-Zahrani in partial fulfilment of the requirements of the degree of Master of science.

---

*Supervisor, Dr. Don. C. Lawton, Department of Geoscience*

---

*Co-Supervisor, Dr. Gary F. Margrave, Department of Geoscience*

---

*Dr. Christopher R. Clarkson, Department of Geoscience*

---

*Dr. Larry R. Lines, Department of Geoscience*

---

*Dr. Roberto Aguilera, Department of Chemical and  
Petroleum Engineering*

---

*Date*

## **Abstract**

A 3D multicomponent seismic dataset from the Horn River Basin was assessed for mapping fractures. The data had good fold, offset and azimuth distributions and several approaches were used to interpret the distribution of natural fractures. In addition to amplitude mapping, PP and PS curvature maps enhanced the structural interpretation of the data and enabled the lateral continuity of faults and fractures to be mapped across the area of the seismic survey. Both horizon and volume based most negative curvature were effective in mapping fault and fracture trends within both Exshaw and Muskwa shale gas targets.

At the Exshaw level, the curvature shows one main fault trend: northwest-southeast trending normal faults that dip toward the southwest. At the Muskwa level, the curvature image shows different major fault trends, namely north-south trending normal fault, northeast-southwest trending reverse fault, and northwest-southeast trending strike-slip fault. Fractures interpreted using curvature attributes are close to the major faults and their dominant trends are generally parallel to the major faults in the area.

The integration of curvature, interval  $V_p/V_s$ , scaled Poisson's ratio computed from the AVO analysis, instantaneous frequency and amplitude attributes yields an improved overall structural and rock properties interpretation. The most negative curvature map highlights the major fault and fracture trends and the  $V_p/V_s$  map, the instantaneous frequency map as well as the amplitude maps highlights potential highly fractured areas within the shale reservoir that have been induced by the major faults. The

high spatial correlation of the scaled Poisson's ratio computed from the AVO analysis with interval  $V_p/V_s$  maps computed at the level of Exshaw and Muskwa reservoir suggest areas of possible increased reservoir potential from these maps. Areas of low interval  $V_p/V_s$  are interpreted to outline possible better porosity development within the Exshaw and Muskwa formations.

## **Acknowledgements**

I sincerely would like to thank my supervisor, Dr. Don Lawton for his guidance and help on the research for my Master program. I also would like to express my gratitude to the committee members, Dr. Chris Clarkson, Dr. Larry Lines and Dr. Roberto Aguilera for their highly appreciated advice. In addition, I would like to thank the directors, staffs and students of the CREWES Project at the University of Calgary for various help, especially Rolf Maier and Kevin Hall for varied assistance.

Thanks to the Olympic Seismic Ltd. for providing the 3D multicomponent data. Software that used in this research was provided to the University of Calgary by Seismic Micro Technology and Hampson-Russell. The important support for my Master program by Saudi Aramco is highly appreciated.

Finally, I would like to thank my wife, Norah, for her patience, support, and encouragement during my study.

## **Dedication**

To my family and friends for their prayers specially my dear wife, Norah and children,

Hanin, Fay and Auwais

## Table of Contents

Approval Page.....	ii
Abstract.....	iii
Acknowledgements.....	v
Dedication.....	vi
Table of Contents.....	vii
List of Tables.....	ix
List of Figures and Illustrations.....	x
List of Symbols, Abbreviations and Nomenclature.....	xviii
CHAPTER 1: INTRODUCTION.....	1
1.1 Shale gas.....	1
1.2 Natural fractured reservoirs.....	4
1.2.1 Natural fracture classification.....	5
1.2.2 Factors controlling fracture intensity.....	8
1.3 Objectives of this thesis.....	11
1.4 The significance of this thesis.....	12
1.5 Structure of this thesis.....	12
1.6 Software used.....	12
CHAPTER 2: INTERPRETATION OF 3D MULTICOMPONENT SEISMIC DATA FROM THE HORN RIVER BASIN, NORTHEAST BRITISH COLUMBIA.....	13
2.1 Introduction.....	13
2.2 Geologic setting.....	13
2.3 Exshaw Formation.....	16
2.4 Muskwa Formation.....	21
2.5 PP interpretation.....	25
2.6 Combined PP and PS interpretation.....	33
2.7 Summary.....	47
CHAPTER 3: 3D CURVATURE ANALYSIS AND VP/Vs INTERVAL MAPPING.....	48
3.1 Introduction.....	48
3.2 Theory.....	48
3.3 Curvature analysis and results.....	50
3.4 3D visualization.....	56
3.5 Fracture interpretation.....	58
3.6 Interval Vp/Vs analysis, amplitude, and instantaneous frequency.....	60
3.7 Results for Exshaw Formation.....	62
3.8 Result for the base of Muskwa shale reservoir.....	68
3.9 Summary.....	72
CHAPTER 4: AVO ANALYSIS AND ATTRIBUTES.....	73
4.1 Introduction.....	73
4.2 Theory.....	73

4.3 AVO and rock properties in shale gas .....	76
4.4 AVO analysis of the top of Exshaw shale event.....	78
4.5 AVO analysis of the base of Muskwa shale event.....	84
4.6 Summary.....	91
CHAPTER 5: CONCLUSIONS AND RECOMMENDED FUTURE WORK.....	92
REFERENCES .....	95

## List of Tables

<b>Table 1.1: Summary data for each formation analyzed. The solid red rectangles indicate the main shale gas reservoir on the Horn River Basin (British Columbia Ministry of Energy and Mines, 2005).....</b>	<b>3</b>
<b>Table 1.2: Experimental and Natural Fracture Classifications (after Nelson, 1985). .....</b>	<b>6</b>
<b>Table 1.3: Relative mineralogy percentages determined from XRD analyzes for Exshaw shale formation (British Columbia Ministry of Energy and Mines, 2006). .....</b>	<b>10</b>
<b>Table 1.4: Relative mineralogy percentages determined from XRD analyzes for Muskwa shale (British Columbia Ministry of Energy and Mines, 2006). .....</b>	<b>10</b>

## List of Figures and Illustrations

<b>Figure 1.1: Multipad-horizontal drilling through the shale gas.</b> .....	2
<b>Source:</b> <a href="http://www.intragaz.com/en/geophysics_drilling.html">http://www.intragaz.com/en/geophysics_drilling.html</a> .....	2
<b>Figure 1.2: Location and limits of the Horn River Basin (highlighted in red), which is located in northeast British Columbia. Source:</b> <a href="http://www.northernrockies.org/Departments/Leg_Admin/Bulletin_Board/HRB%20Symposium/HRB%20FAQ2.pdf">http://www.northernrockies.org/Departments/Leg_Admin/Bulletin_Board/HRB%20Symposium/HRB%20FAQ2.pdf</a> .....	3
<b>Figure 1.3: Stratigraphic section of Devonian-Mississippian strata in northern British Columbia. Dashed blue lines show Horn River Basin stratigraphy and the red solid boxes highlight the Exshaw and Muskwa shale reservoirs (from Ross and Bustin, 2008).</b> .....	4
<b>Figure 1.4: Block diagram showing the fracture types: (1) extensional fracture (green), (2) shear fractures (blue) and stylolites (red). <math>\sigma_1</math>, <math>\sigma_2</math> and <math>\sigma_3</math> are maximum, intermediate, and minimum principal stresses, respectively (from Al Duhailan, 2008).</b> .....	6
<b>Figure 1.5: rose diagram of shear fractures associated with normal fault (From Stearns 1968b).</b> .....	7
<b>Figure 1.6: Outcrop example from Guatemala, of normal fault that consists of multiple shear fractures.</b> .....	8
<a href="http://www.webpages.uidaho.edu/~simkat/geol345_files/fault_zone.jpg">http://www.webpages.uidaho.edu/~simkat/geol345_files/fault_zone.jpg</a> .....	8
<b>Figure 1.7: Histogram showing the relative relationship between fracture intensity and lithology (mineral composition and grain size). Modified after Nelson (2001).</b> .....	9
<b>Figure 2.1: Devonian to Lower Mississippian stratigraphy of the study area (from British Columbia Ministry of Energy and Mines, 2006).</b> .....	15
<b>Figure 2.2: Map of the Slave Point Formation which is the base of the Muskwa Formation in the area of Horn River Basin. This map, shows the Bovie Fault and several other dominant faults that trend in the area (SW-NE and NW-SE) indicated by the blue dashed lines (from Nieto et al., 2009).</b> .....	16
<b>Figure 2.3: Typical log signatures for the Exshaw Formation. High gamma ray response is characteristic (from British Columbia Ministry of Energy and Mines and CBM Solutions, 2005).</b> .....	18
<b>Figure 2.4: West to east stratigraphic section of Banff and Exshaw Formations in northeastern British Columbia (B-B') (from British Columbia Ministry of Energy and Mines and CBM Solutions, 2005).</b> .....	19

<b>Figure 2.5: Depth map of the top of the Exshaw Formation showing the depths from surface (from British Columbia Ministry of Energy and Mines and CBM Solutions, 2005) .....</b>	<b>20</b>
<b>Figure 2.6: Typical log signatures of the Muskwa Formation which is highlighted in yellow (from British Columbia Ministry of Energy and Mines and CBM Solutions, 2005) .....</b>	<b>22</b>
<b>Figure 2.7: North to south stratigraphic cross section of the Muskwa Formation in the eastern portion of the study area (A-A') (B – B') (from British Columbia Ministry of Energy and Mines and CBM Solutions, 2005). .....</b>	<b>23</b>
<b>Figure 2.8: Upper surface of the Muskwa Formation showing the drill depths from surface (British Columbia Ministry of Energy and Mines and CBM Solutions, 2005). .....</b>	<b>24</b>
<b>Figure 2.9: P-wave velocity versus S-wave velocity crossplot for a well near the 3C-3D survey. The mudrock line is indicated by dashed yellow line. The upper left corner shows the vertical cross section of all points and the highlighted zone1, and zone2 indicated by red and yellow rectangular; respectively. The color bar indicates gamma-ray values. ....</b>	<b>26</b>
<b>Figure 2.10: Statistically extracted wavelet from PP volume for seismic-well tie, the top shows the wavelet in time domain and bottom in frequency domain. ..</b>	<b>27</b>
<b>Figure 2.11: Seismic-well tie for PP data showing from left to right: Gamma-ray (green), P-wave velocity log (red), density log (blue), calculated impedance log (pink), reflectivity (black), the synthetic seismogram with six traces (blue), the extracted wavelet and 14 traces that have been extracted from the 3D dataset for the PP volume near the wellbore (black).....</b>	<b>28</b>
<b>Figure 2.12: A zoom view of logs and seismic-well tie for PP data at the Exshaw shale reservoir. ....</b>	<b>29</b>
<b>Figure 2.13: (a) Log plots showing Gamma Ray and Vp/Vs for well A; the red color highlights the high gamma-ray values of the Exshaw shale that exceeded the 150 API, the orange color indicates the gamma-ray value less than 150 API value and higher than 75 API of both Exshaw shale and Lower Banff shale, and the shaded blue color point towards the limestone of the Kotcho Formation which has the values less than 75 API, (b) Crossplot: Vp/Vs versus GR. The color bar (right) shows the GR values in API. ....</b>	<b>30</b>
<b>Figure 2.14: A detail view of logs and seismic-well tie for PP data at the Muskwa shale reservoir. ....</b>	<b>31</b>
<b>Figure 2.15: (a) Log plots showing Gamma Ray and the calculated Vp/Vs for well A from equation 2.2; the red color highlights the high gamma-ray values of the Muskwa shale that exceeded the 125 API, the orange color</b>	

indicates the gamma-ray value less than 125 API value and higher than 75 API of both Muskwa shale and Fort Simpson shale. The shaded blue color indicates the limestone of the Kotcho Formation which has the values less than 75 API (b) Crossplot:  $V_p/V_s$  versus GR. The color bar (right) shows the GR values in API. .... 32

**Figure 2.16: Seismic-well tie for PS data showing from left to right: Gamma-ray log (green), S-wave velocity log calculated by Equation 2.2 (red), density log (blue), calculated shear impedance log (red), reflectivity (black), the synthetic seismogram with six traces (blue), the extracted wavelet and 12 traces that have been extracted from the 3D dataset near the wellbore (black)..... 34**

**Figure 2.17: Statistically extracted wavelet from PS volume for Seismic-well tie, the top shows the wavelet in time domain and bottom in frequency domain. .. 35**

**Figure 2.18: Example of in-line section from PP volume (above) and PS volume (below) showing the seismic-well tie for well A and the seven key interpreted seismic horizons..... 36**

**Figure 2.19 Inline 73: PP section (left) and PS section (right) stretched in PP time at well A. a) Unzoomed section after PP and PS registration (domain conversion, strata velocity model, and plus horizons matching applied). b) Zoomed view on the shallower horizons (Debolt Fm., and Banff Fm.). c) Zoomed view on the Exshaw Fm., Tetcho Fm., and Fort Simpson shale Fm. d) Zoomed view on the deep horizons (Muskwa Fm., and Evie Fm.). ..... 37**

**Figure 2.20: Exshaw shale PP time structure map (a) and PS time structure map (b) showing the interpreted faults (black solid lines) that cut this surface in the area. Cross sections A-A` shown in Fig. 2.22 (through the channel artifacts) and B-B` shown in Fig. 2.23 (through the faults) are indicated by dashed red lines. The channel artifacts are highlighted by dotted black lines) ..... 39**

**Figure 2.21: The base of weathering map which highlights the near surface channels in blue (Olympic Seismic Ltd., 2009)..... 40**

**Figure 2.22: A-A' traverse through PP section (above) and PS section (below) showing the imprint of the near surface channels (red rectangular) on the imaging below it. Refer to Figure 2.20 for the location of this cross section. .... 41**

**Figure 2.23: B-B' traverse through PP section (above) and PS section (below), showing the four normal faults (yellow ellipses) that cut the shallow horizons including the Exshaw shale. Refer to Figure 2.20 for the location of this cross section. .... 42**

**Figure 2.24: Base Muskwa shale PP time structure map (upper) and PS time structure map (lower) showing the interpreted faults (black solid lines) that**

cut this surface in the area and the location of the two cross sections C-C` and D-D` .....	44
<b>Figure 2.25: C-C` traverse through PP section, shows the strike slip fault (yellow ellipse) and the normal faults (black solid lines) that cut the deep horizons including Muskwa shale. Refer to Figure 2.24 for the location of the cross section.....</b>	<b>45</b>
<b>Figure 2.26: D-D` traverse through PP section (above) and PS section (below), shows the reverse fault indicated by black solid lines that cut the deep horizons including Muskwa shale. Refer to Figure 2.24 for the location of the cross section.....</b>	<b>46</b>
<b>Figure 3.1: (a) illustrates a 2D curvature of a line and the sign convention for curvature attributes. The arrows represent vectors, that are normal to the surface. When vectors are parallel on flat or planar dipping surfaces, the curvature is zero. When vectors diverge over anticlines, the curvature is defined as positive and every time they converge over synclines, the curvature is defined as negative. (b) Showing the two orthogonal set that intersect with the 3D surface.....</b>	<b>49</b>
<b>Figure 3.2: (a) Horizon-based most negative curvature for the top of Exshaw horizon (b) 0.894 second time slice of the volume-based most negative curvature computed on PP volume. Red ellipses indicate acquisition footprint. The blue arrows show the four normal faults and the white arrows show the two possible strike-slip faults.....</b>	<b>52</b>
<b>Figure 3.3: (a) 1.208 second volume-based most negative curvature computed on PS volume (b) base of weathering layer map. ....</b>	<b>53</b>
<b>Figure 3.4: (a) 0.820 second volume-based most negative curvature computed on PP Volume (b) 0.820 second volume-based most positive curvature computed on PP Volume. ....</b>	<b>54</b>
<b>Figure 3.5: (a) Horizon-based most negative curvature on the PP volume for the base of Muskwa horizon (b) 1.52 second time slice of the volume-based most negative curvature computed on PP volume. The black arrows indicate the two major faults and the white arrows show circular features which are interpreted to be possible mounds or karsting features.....</b>	<b>55</b>
<b>Figure 3.6: Horizon-slice through most negative curvature volume at the base of the Muskwa shale horizon. The color bar indicates dark blue for most negative curvature value and red for positive curvature value. (a) Top view (b) the same horizon slice but looking at it from the southeast corner (c) top view from the northeast corner (d) zoomed 3D view showing the mound feature. The strike slip fault is indicated by red arrows. ....</b>	<b>57</b>

**Figure 3.7: Horizon-slice extracted from most negative curvature PS volume at the top of the Exshaw shale horizon. The color bar indicates blue and black colors for most negative curvature value and white color for positive curvature value. (a) top view looking north (b) the same horizon slice but looking south with angle to show the 3D view (c) top view from the northwest corner and with using light to indicate the four normal faults (green arrows) intercepting possible other faults (red arrows) orthogonally. The artifacts generated by a significant channel system within the near surface are indicated by negative curvature values shown by the blue color. .. 59**

**Figure 3.8: Horizon-slice through most negative curvature PP volume at the base of the Muskwa shale horizon; the color bar indicates dark blue for most negative curvature value and red for positive curvature value. (a) Top view for the whole surface (b) Zoomed view of high fractured density area. The location of this area is shown in white dashed rectangular in the above figure. (c) Zoomed view of low fractured density area indicated by curvature. The location of this area is shown in black dashed rectangular in the above figure. .... 60**

**Figure 3.9: Example from Powder River Basin showing the fracture signature using amplitude and instantaneous frequency seismic attributes. (a) Instantaneous frequency map shows that the fractures are present in low frequency area, indicated by blue color. (b) Amplitude map values shows fractured area are characterized by low amplitude values highlighted by blue and green colors (from Mavko, 2010). .... 62**

**Figure 3.10: SW-NE seismic line showing the intervals used for interval Vp/Vs calculation. Interval 1 is from the Banff Formation to the Tetcho Formation; interval 2 is from the Banff Formation to the Fort Simpson Formation; interval 3 is from the Fort Simpson Formation to the Base of Muskwa Formation ; interval 4 is from the Fort Simpson Formation to the Evie Formation. Vp/Vs extrapolated from well values superimposed on the seismic sections. Refer to Figure 3.10 for the location of the line. Black solid lines indicate interpreted faults. .... 63**

**Figure 3.11: (a) Interval Vp/Vs map from the Banff Formation to the Tetcho Formation. (b) Interval Vp/Vs map from the Banff Formation to the Fort Simpson Formation. Dashed white line indicates the location of the seismic line shown in Figure 3.9. Dashed white ellipses show high Vp/Vs trends..... 64**

**Figure 3.12: (a) Instantaneous frequency map extracted with a 30 ms window centered at the top of Exshaw seismic horizon. (b) Amplitude map extracted at 30 ms window centered at top of the Exshaw seismic horizon. Black ellipses highlight low values of both maps that correlate with high Vp/Vs areas shown in Figure 3.10. Dashed blue polygons indicate artifacts generated by the channel system within the near surface. .... 66**

- Figure 3.13: (a) Horizon-slice through most negative curvature volume at the top of the Exshaw shale horizon. Black indicates negative curvature values. (b) Interval Vp/Vs map from the Banff Formation to the Fort Simpson Formation. Blue color indicate higher Vp/Vs values and black solid lines indicate interpreted faults that have been mapped using curvature at this level. .... 67**
- Figure 3.14: (a) Interval Vp/Vs map from the Fort Simpson Formation to the base of Muskwa Formation. (b) Interval Vp/Vs map from the Fort Simpson Formation to the Evie Formation. Dashed white line indicates the location of the seismic line shown in Figure 3.9. .... 69**
- Figure 3.15: (a) RMS Amplitude extracted with a 30 ms window centered at the base of Muskwa shale horizon. Blue color indicates low amplitude area. (b) Instantaneous frequency map extracted with a 30 ms window centered at the base of Muskwa shale seismic horizon. Red & yellow colors indicate, areas of low instantaneous frequency. .... 70**
- Figure 3.16: (a) Horizon-slice through most negative curvature volume at the base of the Muskwa shale horizon. Blue color indicates negative curvature values. (b) Interval Vp/Vs map from the Fort Simpson Formation to the Evie Formation. Blue color indicates high Vp/Vs values. Black solid lines indicate interpreted faults that have been mapped using curvature at this level and dashed black & white circles identify circular features which are interpreted to be possible mounds. .... 71**
- Figure 4.1: An incident P-wave on a boundary separating two layers converts into four waves: reflected P-wave (Rpp), reflected S-wave (Rps), transmitted P-wave (Tpp) and transmitted S-wave (Tps)..... 74**
- Figure 4.2: Plot showing how the intercept and gradient values have been obtained from the pre-stack gathers after the AVO analysis (from Hampson-Russell, 2007). .... 75**
- Figure 4.3: Map of Vp/Vs ratio and porosity-height from 8 wells through the Lower Doig and Upper Montney. The red arrows highlight wells with very low porosity-height values and correspond in general to areas of higher Vp/Vs. The blue arrow highlights a well with a large porosity-height at the edge of the seismic data where the inversion is adversely affected by decreased fold. The yellow line is the approximate location of a horizontal well where micro-seismic data were recorded (from Close et al., 2010). .... 77**
- Figure 4.4: The AVO classification (Rutherford and Williams, 1989, and Castagna et al, 1998). .... 79**
- Figure 4.5: CDP Super Gather near the key well in the area. The background color indicates the incident angle (on the left). The gradient behaviour at the**

top of the Exshaw shale reservoir (upper right) shows class IV AVO. The gradient versus intercept crossplot is shown on lower right (700-950 ms)..... 80

Figure 4.6: AVO intercept (A) map extracted at the top of Exshaw shale reservoir..... 80

Figure 4.7: AVO gradient (B) map extracted at the top of Exshaw shale reservoir..... 81

Figure 4.8: AVO scaled Poisson's ratio (A+B) map extracted at the top of Exshaw shale reservoir..... 81

Figure 4.9: (a) Scaled Poisson's ratio (A+B), 30 ms RMS window AVO attribute extraction map centered at the top of Exshaw shale reservoir (above). (b) A-B cross section of the super stack generated using Hampson - Russell's AVO software (below). Faults are indicated by red solid lines. .... 82

Figure 4.10: (a) AVO scaled Poisson's ratio (A+B) map extracted at the top of Exshaw shale reservoir. (b) Interval Vp/Vs map from the Banff Formation to the Tetcho Formation which represents the Vp/Vs interval at the top Exshaw of shale. Cold colors indicate low values of both attributes. Note the yellow circles are showing the location of two CDP that are showing in Figure 4.11. .... 83

Figure 4.11: (a) CDP super gather chosen from the high gradient values area. (b) CDP Super Gather chosen from the low gradient values area. The background color of the gather indicates the incident angle (on the left). The gradient behaviour at the top of the Exshaw shale reservoir (upper right of both CDPs) shows how the gradient decreases from high value (upper CDP) to low gradient value (Lower CDP). The gradient versus intercept crossplot is shown on lower right of both CDPs (750-900 ms).Refer to Figure 4.10 for the location of these two CDPs..... 85

Figure 4.12: CDP gather near the key well in the area and the background color indicates the incident angel (on the left). The gradient behaviour at the base of the base Muskwa shale reservoir (upper right) shows the amplitude is decreasing with angle. The gradient versus intercept crossplot is shown on lower right for interval at the level of Base Muskwa event between 1300 to 1600 ms..... 86

Figure 4.13: RMS AVO intercept map extracted over a 30 ms window centred at the base of Muskwa shale event. The solid lines indicate the interpreted major faults at this level. The dotted black lines identify artifacts generated by channels within the near surface. .... 86

Figure 4.14: RMS AVO gradient attribute map extracted over a 30 ms window centred at the base of Muskwa shale event..... 88

**Figure 4.15: RMS scaled Poisson's ratio map extracted over a 30 ms window centred at the base of Muskwa shale event..... 88**

**Figure 4.16: (a) AVO scaled Poisson's ratio (A+B) map extracted at the base of Muskwa shale reservoir. (b) Interval Vp/Vs map from the Fort Simpson Formation to the Evie Formation which represents the Vp/Vs interval at the base of the Muskwa shale. Cold colors (purple and blue) indicate low values of both attributes..... 89**

**Figure 4.17: (a) CDP super gather chosen from the high scaled Poisson's ratio value area. (b) CDP super gather chosen from the low scaled Poisson's ratio value area. The background color of the gather indicates the incident angle (on the left). The gradient behaviour at the base of the Muskwa shale reservoir (upper right of both CDPs) shows how the gradient decreases from high value (upper CDP) to low gradient value (lower CDP). The gradient versus intercept crossplot is shown on lower right of both CDPs (1300-1600 ms). Refer to Figure 4.16 for the location of these two CDPs highlighted by red circles. .... 90**

## List of Symbols, Abbreviations and Nomenclature

$\sigma_1$	Maximum vertical stress
$\sigma_2$	Intermediate horizontal stress
$\sigma_3$	Minimum horizontal stress
AVO	Amplitude Versus Offset
$V_p$	Compressional wave velocity
$V_s$	Shear wave velocity
$\theta$	P-wave Incident angle
$R_0$	Normal incident reflection coefficient
$A$	AVO Intercept
$B$	AVO Gradient
3C	Three-component
3D	Three-dimensional
RMS	Root Mean Square
MS	Millisecond
CDP	Common Depth Point
PP, PS	Reflected to pure compressional, compressional to shear reflection
$\omega(t)$	Instantaneous Frequency
BCMEM	British Columbia Ministry of Energy and Mines
HRB	Horn River Basin
F	Fourier transform
$u$	Inline or crossline component of reflector dip
$\alpha$	Fractional real number that typically range between 0 and 1
TCF	Trillion cubic feet

## CHAPTER 1:. INTRODUCTION

### 1.1 Shale gas

Shale gas is one of the four types of unconventional gas plays that are growing rapidly in North America and the (Kuuskraa and Stevens, 2009). The other three are tight gas sand, Coal bed methane and gas hydrates. What makes this play attractive to oil and gas companies compared with conventional resources is that the shale gas formations are continuous over large areas, with giant reserves, and the gas is enclosed within microporosity of the shales, and the rock, in this case act as source, reservoir and trap (Kuuskraa and Stevens, 2009). The challenge in this play is how to flow the gas from these tiny pores. One of the current solutions to this problem is the use of the new drilling technology such as multi-pad horizontal wells and multi-stage hydraulic fracturing (Figure 1.1). For example, this technology helped to double the gas productivity of the Barnett shale field in Texas and make it the largest gas field in that state (Beaudoin and Shaw, 2009). However this technology alone is not enough for optimum exploration and development. More advanced multi-disciplinary specialized techniques such as spectrographic, petrophysical, geochemical and geophysical analysis are needed in order to get a detailed picture of the shale gas complexity and heterogeneity. Data integration of all these methods will help to minimize the cost of these horizontal wells by locating them in the optimum location and direction (Beaudoin and Shaw, 2009).

In Canada, the Horn River Basin, which is located in northeast British Columbia (Figure 1.2), is an area where this shale gas play is being intensely explored. The areal extent of this basin is about 1.28 million hectares and the estimated total gas-in-place is 500 trillion cubic feet (Beaudoin and Shaw, 2009). Intensive core analysis was carried

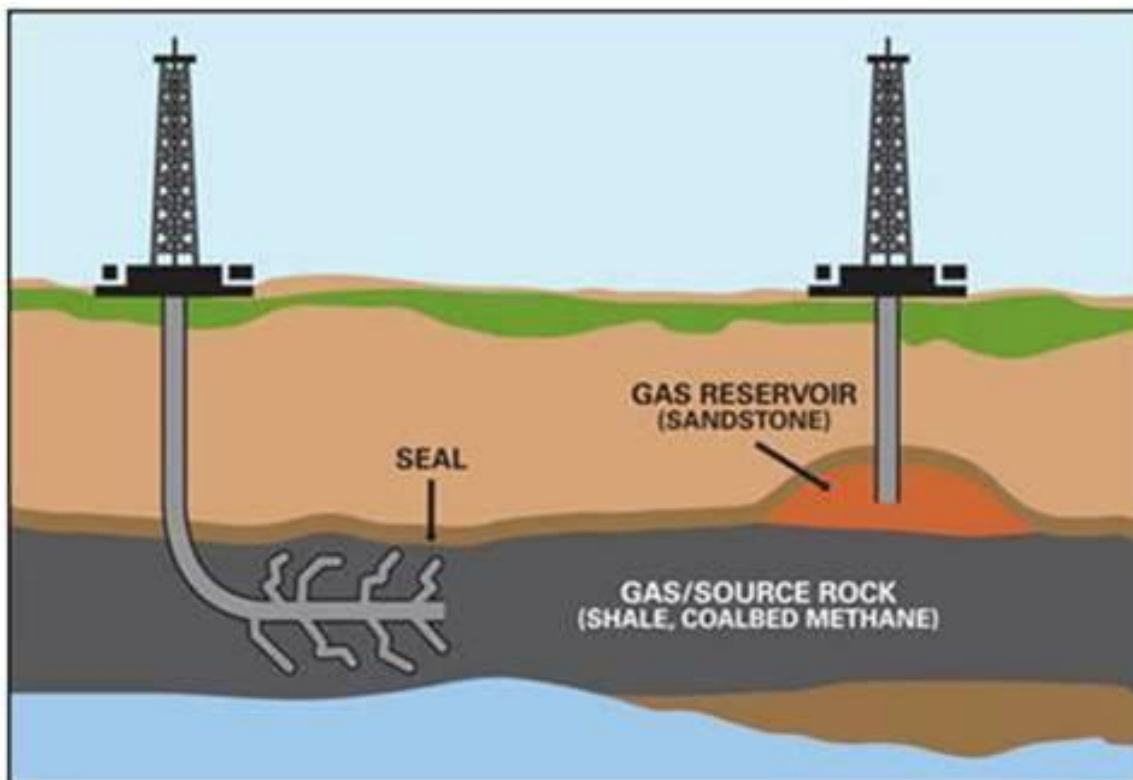


**Figure 1.1: Multipad-horizontal drilling through the shale gas.**

**Source: [http://www.intragaz.com/en/geophysics\\_drilling.html](http://www.intragaz.com/en/geophysics_drilling.html)**

out by CBM Solutions Ltd., for the British Columbia Ministry of Energy and Mines, Oil and Gas Division, Resource Development and Geoscience Branch to highlight the gas shale potential in the area (British Columbia Ministry of Energy and Mines and CBM Solutions, 2005). The analysis was focused on four properties that are important characteristics in each shale gas play. These are the total organic carbon content, the thermal maturity, sorption capacity, and mineralogy. The results of BCMEM study are summarized in Table 1.1, and the potential shale gas reservoirs are designated in it (British Columbia Ministry of Energy and Mines and CBM Solutions, 2005). These

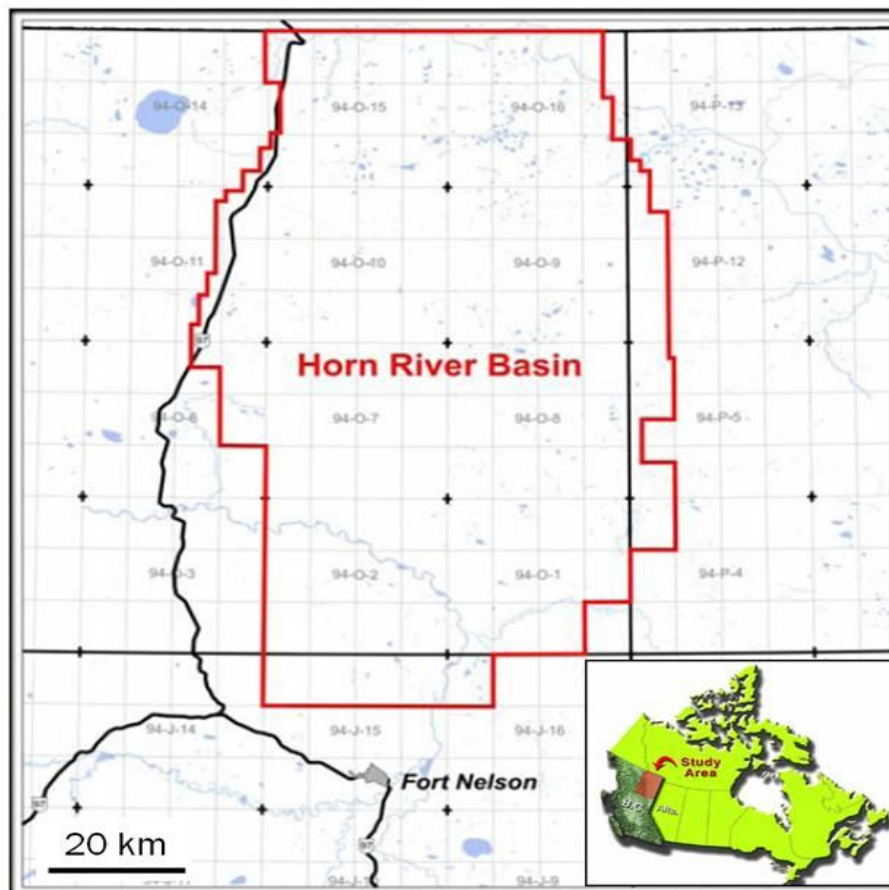


Figure 1.2: Location and limits of the Horn River Basin (highlighted in red), which is located in northeast British Columbia.

Source: [http://www.northernrockies.org/Departments/Leg\\_Admin/Bulletin\\_Board/HRB%20Symposium/HRB%20FAQ2.pdf](http://www.northernrockies.org/Departments/Leg_Admin/Bulletin_Board/HRB%20Symposium/HRB%20FAQ2.pdf)

Table 1.1: Summary data for each formation analyzed. The solid red rectangles indicate the main shale gas reservoir on the Horn River Basin (British Columbia Ministry of Energy and Mines, 2005).

Formation	# of Core Wells	Average Thickness (m)	Average TOC (wt%)	Average Porosity (%)	Mineralogy	Average Gas Capacity at 11 MPa (cc/g)
Exshaw	4	5-10	5.0	4.4	Quartz, Kolinite, Illite	1.3
Besa River	2	450-500	4.3	4.6	Quartz, Kolinite, Illite	0.8
Fort Simpson	3	475-525	0.4	3.3	Quartz, Kolinite, Illite	0.3
Muskwa	8	15-25	3.1	3.2	Quartz, Kolinite, Illite	0.7

targets are the Upper Devonian/Lower Mississippian Exshaw shale and the Muskwa shale member of the Middle Devonian Horn River Basin Formation (Figure 1.3). There are targets other than the Exshaw and the Muskwa shale within the basin and these are the Evie and Otter Park shale (Figure 1.3)(British Columbia Ministry of Energy and Mines and CBM Solutions, 2010).

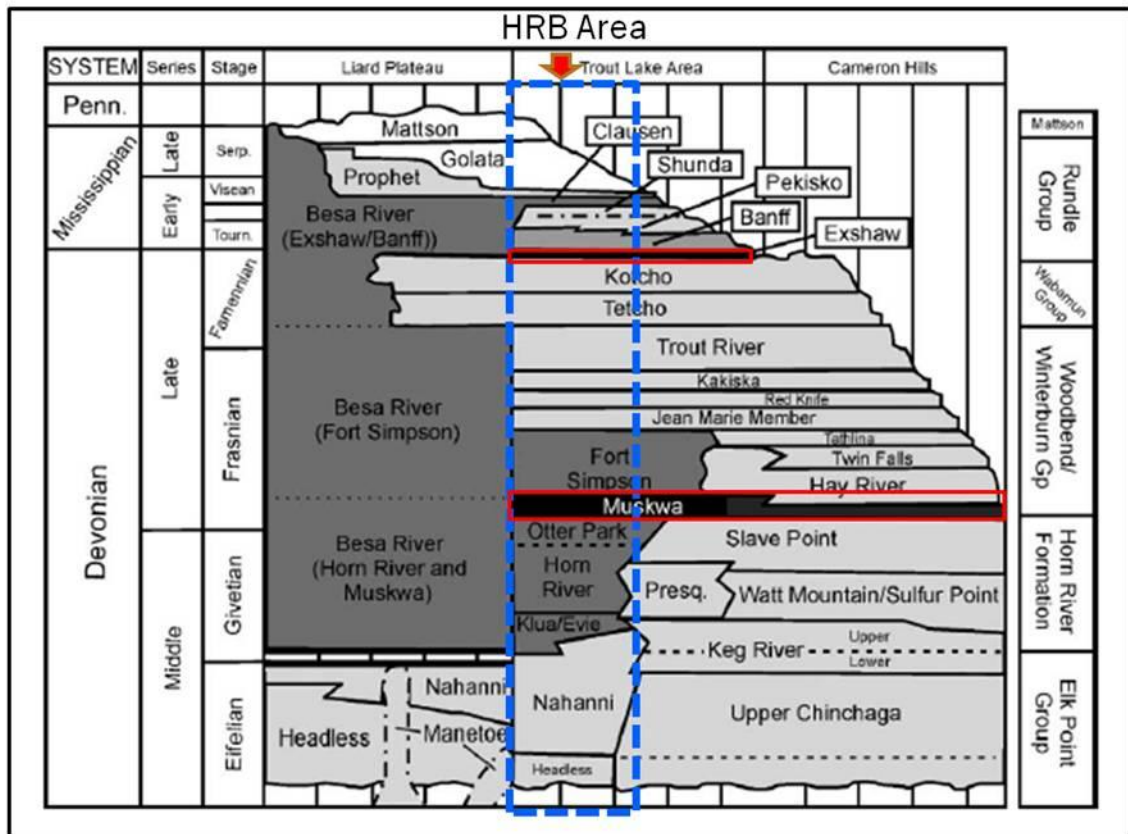


**Figure 1.3: Stratigraphic section of Devonian-Mississippian strata in northern British Columbia. Dashed blue lines show Horn River Basin stratigraphy and the red solid boxes highlight the Exshaw and Muskwa shale reservoirs (from Ross and Bustin, 2008).**

## 1.2 Natural fractured reservoirs

A natural fracture is defined as a macroscopic crack that results naturally from the accumulated stresses that break the rock (Nelson, 1985). These natural fractures can have

a positive or negative effect on fluid flow throughout the reservoir (Nelson 1985). These subgeological features increase the complexity and the heterogeneity of any reservoir ranging from microscopic cracks to kilometre-long fracture swarms. They can be open corridors for fluid flow or barriers. Therefore, they may play a significant role in reservoir production and reservoir performance. In order to succeed in this kind of play, extensive evaluation studies are needed, including geological, geophysical and petroleum components. The end result of this study will allow the exploration and development program to be designed to target these fractures or to avoid them.

Stearns and Friedman (1972), and Nelson (1979) studied the origins of fractures in laboratory experiments and then they applied what they observed from these experiments to both outcrop and subsurface natural fractures. Their assumption was that the natural fracture patterns that describe the status of stress at the time of the breaking of the rock in the subsurface setting are similar to those obtained from rocks in laboratory experiments.

### ***1.2.1 Natural fracture classification***

Nelson (1985) classified natural fractures into two groups, summarized in Table 1.2. Group one is the experimental fracture classification and the second group is the natural fracture classification. The experimental fracture classification is divided into three types of fractures: shear, extension and tensile fractures. A shear fracture consists of two fractures making an x shape and their relative movements are opposite to each other. They make an acute angle to the maximum principal stress ( $\sigma_1$ ), and an obtuse angle to the minimum principal stress ( $\sigma_3$ ) (Nelson, 1985) (Figure 1.4). In comparison, an

extension fracture consists of one crack that is parallel to the maximum principal stress ( $\sigma_1$ ) and perpendicular to the minimum principal stress ( $\sigma_3$ ).

**Table 1.2: Experimental and Natural Fracture Classifications (after Nelson, 1985).**

Experimental Fracture Classification:	Naturally Occurring Fracture Classification
1- Shear fractures 2- Extension fractures 3- Tensile fractures	1-Tectonic Fractures (due to surface forces) 2- Regional fractures (due to surface forces or body forces) 3- Contractional forces ( due to body forces) 4- Surface-related fractures ( due to body forces)

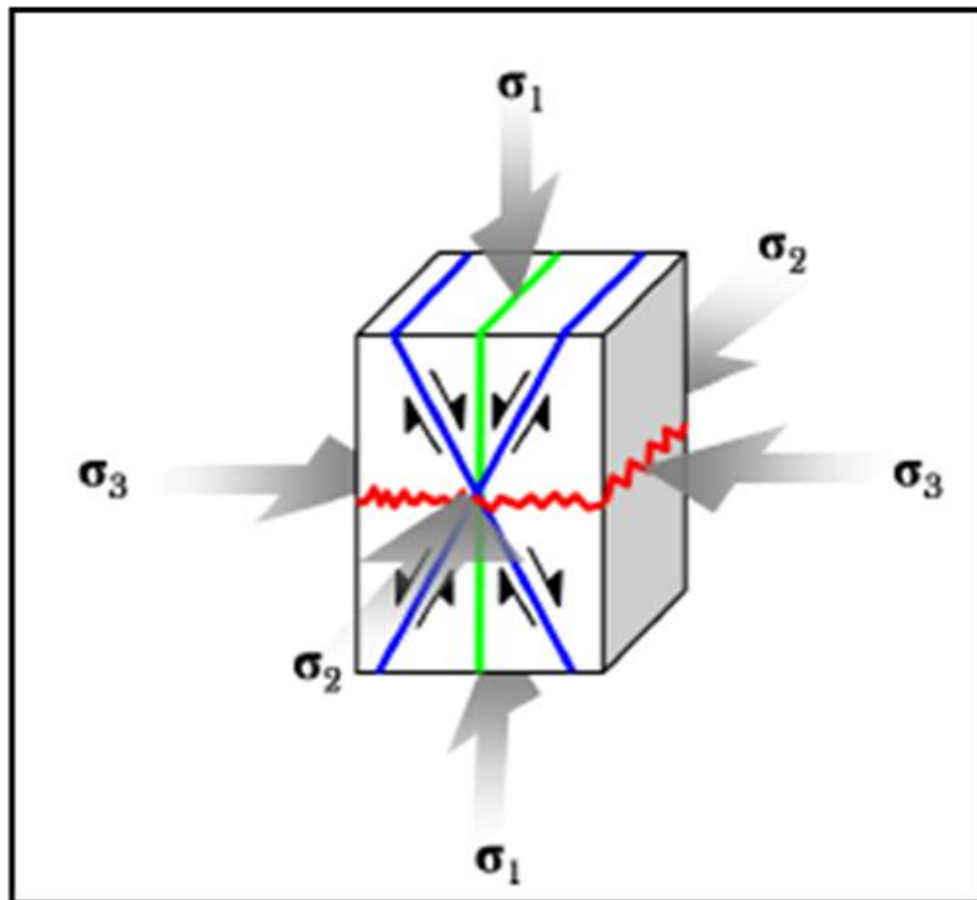


**Figure 1.4: Block diagram showing the fracture types: (1) extensional fracture (green), (2) shear fractures (blue) and stylolites (red).  $\sigma_1$ ,  $\sigma_2$  and  $\sigma_3$  are maximum, intermediate, and minimum principal stresses, respectively (from Al Duhailan, 2008).**

A tensile fracture is similar to an extension fracture but the difference between them is the sign of the minimum principal stress ( $\sigma_3$ ). When the sign is negative it indicates a tensile fracture and when it is positive it indicates an extension fracture.

Tectonic fractures are those associated with local tectonic events and are formed by the application of surface forces (Nelson, 1985). Two types of fractures are associated with these kinds of fractures. These are fault-related fractures and fold-related fractures. Three common types of fracture orientations are associated with fault-related fractures; shear fractures which are parallel to the fault, shear fractures which are conjugate with the fault and extension fractures which bisect the acute angle between the shear fractures trends (Figure 1.5) (Nelson, 1985).

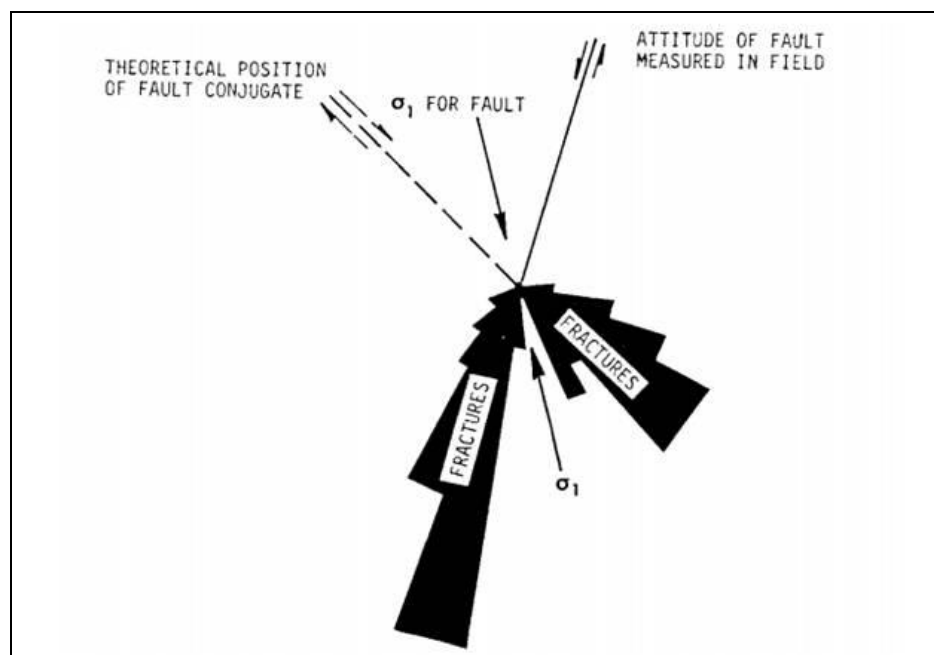


**Figure 1.5: rose diagram of shear fractures associated with normal fault (From Stearns 1968b).**

Figure 1.6 shows an outcrop example from Guatemala of a normal fault (red arrows) with some multiple shear fractures that are conjugate to the fault and making an obtuse angle to the fault plane (green arrows).



**Figure 1.6: Outcrop example from Guatemala, of normal fault that consists of multiple shear fractures.**

[http://www.webpages.uidaho.edu/~simkat/geol345\\_files/fault\\_zone.jpg](http://www.webpages.uidaho.edu/~simkat/geol345_files/fault_zone.jpg)

### ***1.2.2 Factors controlling fracture intensity***

There are five main factors which affect fracture intensity (fracture spacing) in subsurface as summarized below by Nelson (2001). These are :

- 1- Rock composition
- 2- Grain size
- 3- Porosity

- 4- Bed thickness
- 5- Structural position

In general, rocks that contain a high percentage of brittle ingredients such as quartz, feldspar, dolomite, and calcite, have a higher fracture intensity than those that have low percentage of brittle ingredients (Stearns, 1968b; Stearns and Friedman, 1972; Currie, 1974, and Nelson, 2001) (Figure 1.7). Grain size is also is another factor that controls fracture spacing.

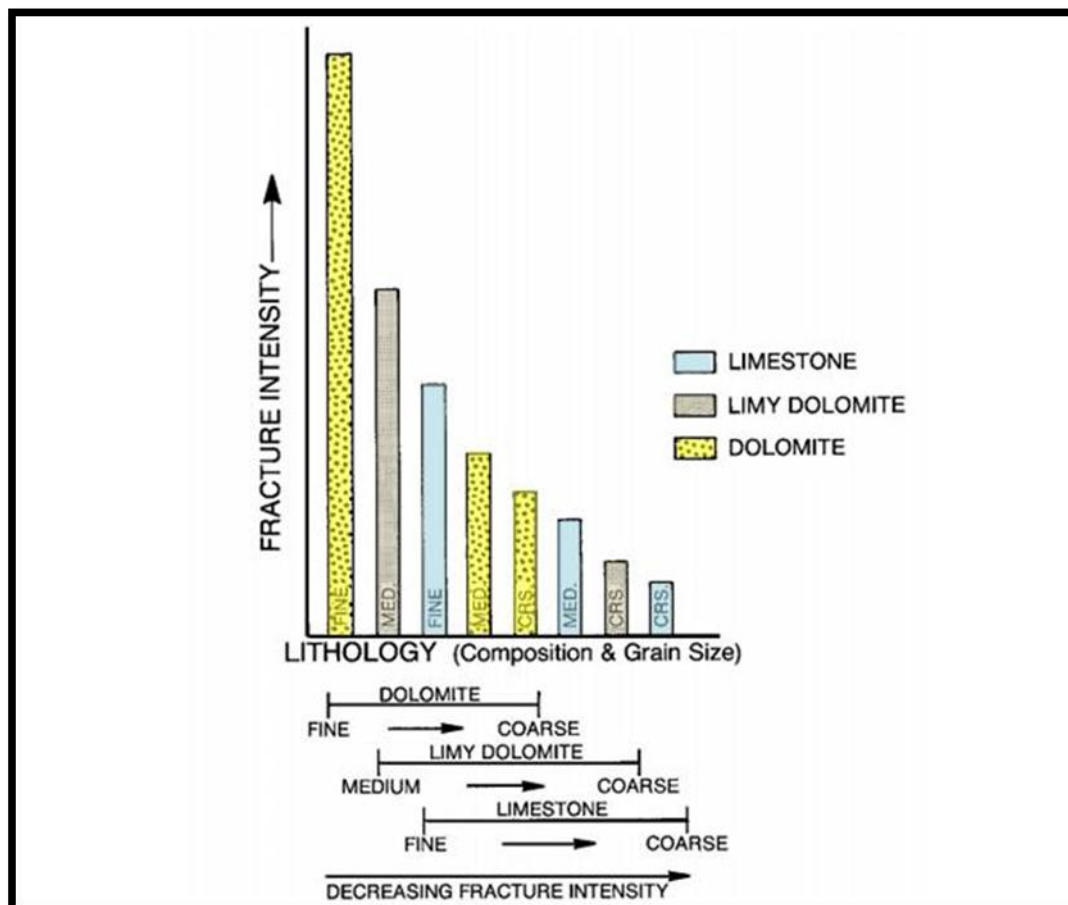


**Figure 1.7: Histogram showing the relative relationship between fracture intensity and lithology (mineral composition and grain size). Modified after Nelson (2001).**

Nelson (2001), showed the relationship between grain size and fracture intensity (Figure 1.7). As the grain size of the rock decreases, the fracture intensity increases. Similarly the porosity and thickness of the rock bed will affect the fracture intensity of the rock, with intensity increasing as thickness and porosity decrease (Nelson, 2001). Knowing all these factors and by examining Tables 1.1, through 1.4, suggests that both shale targets (Muskwa, and Exshaw formations), have a high potential to be fractured. Together they have a high percentage of Quartz (60% to 70% of their mineral composition). Their thicknesses range between 5 to 25 meters, with a low porosity, ranging from 3% to 4% (.

**Table 1.3: Relative mineralogy percentages determined from XRD analyzes for Exshaw shale formation (British Columbia Ministry of Energy and Mines, 2006).**

<b>EXSHAW XRD</b>			<b>Mineralogy (% Relative)</b>					
<b>Name</b>	<b>Location</b>	<b>Depth (m)</b>	<b>Illite/Mica (d=10.00)</b>	<b>Kaolinite (d=7.10)</b>	<b>Quartz (d=4.23)</b>	<b>Calcite (d=3.03)</b>	<b>Pyrite (d=2.71)</b>	<b>Dolomite (d=2.89)</b>
Golata	8-29-83-15W6	3386.55	10	13	71	0	6	0
		3390.10	2	2	43	0	3	49
Sikanni Chief	b-92-D/94-I-4	1573.80	14	15	62	0	0	5

**Table 1.4: Relative mineralogy percentages determined from XRD analyzes for Muskwa shale (British Columbia Ministry of Energy and Mines, 2006).**

<b>Muskwa XRD</b>			<b>Mineralogy (% Relative)</b>					
<b>Name</b>	<b>Location</b>	<b>Depth (m)</b>	<b>Illite/Mica (d=10.00)</b>	<b>Kaolinite (d=7.10)</b>	<b>Quartz (d=4.23)</b>	<b>Calcite (d=3.03)</b>	<b>Pyrite (d=2.71)</b>	<b>Dolomite (d=2.89)</b>
Snake River	c-28-D/94-O-1	1949.70	17	4	77	0	0	0
		1951.10	10	3	84	0	3	0
		1952.60	19	0	64	13	0	4
Shekilie	a-94-G/94-P-8	1539.60	16	1	79	0	2	2
		1542.00	22	2	76	0	0	0
		1545.60	18	0	82	0	0	0
		1548.60	8	3	88	0	2	0
		1551.50	11	2	87	0	0	0
		1553.60	1	0	0	99	0	0

### **1.3 Objectives of this thesis**

The geophysical dataset investigated for this study was from a 3D multicomponent seismic survey which provided good fold, offset, and azimuth distribution with the overall goal to map natural fracture orientations and density with these shale units of the Exshaw and Muskwa formations. Acquiring converted-wave P-S data can provide lithological information and possibly detect fracture networks, whereas conventional P-wave data can reflect matrix and fluid characteristics (Stewart et al., 2003). Wide-azimuth multicomponent data can provide several methods to detect a fracture network. These are seismic attributes such as curvature, and amplitude variation with offset (AVO) analysis (Jianming et al., 2009). Although each method has its own limitations, the integration of all these methods with well data will lead to better fracture prediction (Jianming et al., 2009).

The main objective of the study was to map the shale gas reservoirs and attempt to predict fracture orientation, and possibly fracture areas using seismic attributes. Three approaches were undertaken in order to meet the objectives of this thesis:

- Mapping faults and fracture trends at the level of Exshaw, and Muskwa formations by using both horizon and volumetric based curvature analysis;
- Analysis of full-wave seismic attributes, particularly interval  $V_p/V_s$ ;
- Studying amplitude variation with offset for both shale targets, to locate seismic anomalies that might indicate higher porosity reservoirs;

#### **1.4 The significance of this thesis**

This research integrates all these data analyses with the existing well data that has penetrated both shale targets (Exshaw and Muskwa shales). The end result of all this work is to create a 3D fracture cube, combined with other seismic attributes, to highlight the shale gas sweet spots that are favourable for drilling.

#### **1.5 Structure of this thesis**

Chapter 1 presents an introduction to the thesis by describing a general review of the main concepts in this thesis. Also, it reviews the purpose and the significance of the thesis. Chapter 2 discusses the interpretation of 3-D multicomponent data in the HRB, which include geological setting, seismic-well tie, horizons picks, and time structure maps. Chapter 3 reviews the curvature theory and analysis as well as the  $V_p/V_s$  analysis between the main key horizons in the 3D survey is included. Also, in this chapter, the interpretation results of faults and fractures mapping in terms of orientations using curvature analysis and  $V_p/V_s$  is assessed. The study of the AVO analysis of a top of the Exshaw shale reflector and base of the Muskwa shale reflector is included in Chapter 4. Chapter 5 presents the conclusions achieved from this thesis and recommended future work.

#### **1.6 Software used**

Seismic interpretation and curvature attribute analysis were performed using Kingdom suite software. The computed  $V_p/V_s$  interval, the AVO analysis and the post stack seismic attributes extraction were computed using Geoview -Hampson-Russell's software.

## **CHAPTER 2.: INTERPRETATION OF 3D MULTICOMPONENT SEISMIC DATA FROM THE HORN RIVER BASIN, NORTHEAST BRITISH COLUMBIA**

### **2.1 Introduction**

For a gas shale play to be commercially successful, these tight rocks need to be mechanically stimulated in order to introduce sufficient fracture corridors so that the gas can flow freely to the wellbore. Based on the industry experience, the shale gas wells are difficult to complete and they require specific technologies for completion that are dependent on the reservoir heterogeneity, the physical properties of the shale, and the type of fluids present in the shale. Therefore acquiring accurate results of elastic and mechanical properties, such as porosity, lithology, Poisson's ratio ( $\sigma$ ), faults, fractures trends,  $V_p$ ,  $V_s$  and their ratio, are very important (Li et al., 2009).

In this chapter, well logs and synthetic seismograms are used to correlate the PP and PS seismic sections, from a 3C-3D seismic survey which was interpreted to map major faults and fracture trends at the Exshaw and Muskwa reservoir shales. Detailed registration of multicomponent seismic data aims to highlight lithology and fluid discrimination based on  $V_p/V_s$  values and seismic attributes extracted from the PP and PS (registered in PP time) sections. The end result will assist in directing horizontal well trajectories to avoid crossing faults and fracture systems, and to possibly help identify sweet spot areas that are favourable for drilling.

### **2.2 Geologic setting**

A stratigraphic column of northeast British Columbia is presented in Figure 1.3 and Figure 2.1. The Devonian-Mississippian strata of northeast of British Columbia is interpreted to be deposited in a ramp and basin setting (Richards, 1989). The shaly units

(black and dark gray color) represent the basinal deposits of the Besa River, Exshaw, and Muskwa formations, whereas the carbonate units (light gray color) represent the ramp deposits of the Slave Point, Trout River, and Kotcho formations (Figure 1.3). The Exshaw and Muskwa shales are thin and are present throughout the basin. They are characterized by high gamma ray values on the logs due to their high organic content (British Columbia Ministry of Energy and Mines and CBM Solutions, 2005).

Structurally, the area was subject to north-south extension followed by a compressional period in pre-Proterozoic time which resulted in erosion of sediments towards the southeast (Ross and Stephenson, 1989). During late Paleozoic time, two main fault trends were documented in the area: northwest-southeast trending normal faults that dip toward the southwest and linked in depth with a detachment fault (McClay et al., 1989), and northeast-southwest transverse faults that are associated with compression (Churcher and Majid, 1989) (Figure 2.2).

During Cretaceous-Eocene time, the area was subject to a compressional regime that reactivated old normal faults above a deep detachment in the Upper Devonian-Carboniferous section, forming thrust faults, related fault-bend folds and detachment folds (Eaton et al., 1999).

		Northern NEBC		Southern NEBC	
Mississippian	Lower	<i>Besa River</i>	<i>Banff</i>	<i>Besa River</i>	<i>Banff</i>
			<i>Exshaw</i>		<i>Exshaw</i>
Kotcho	Wabamun				
Trout River					
Devonian	Upper	Redknife	RedKnife		
		<i>Fort Simpson/ Muskwa</i>	Mt Hawk	<i>Fort Simpson/ Muskwa</i>	
			Perdrix		

Figure 2.1: Devonian to Lower Mississippian stratigraphy of the study area (from British Columbia Ministry of Energy and Mines, 2006).

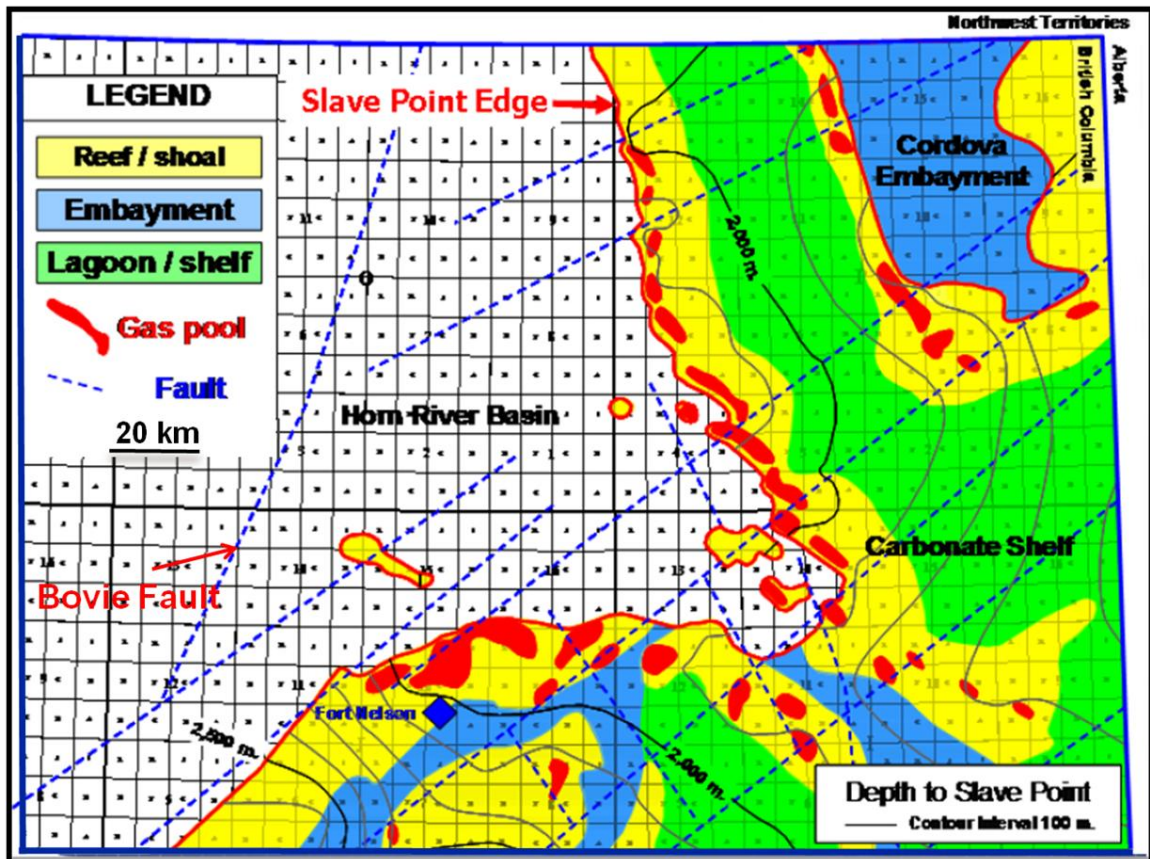


Figure 2.2: Map of the Slave Point Formation which is the base of the Muskwa Formation in the area of Horn River Basin. This map, shows the Bovie Fault and several other dominant faults that trend in the area (SW-NE and NW-SE) indicated by the blue dashed lines (from Nieto et al., 2009).

### 2.3 Exshaw Formation

The Exshaw Formation is generally of Upper Devonian to Lower Mississippian age (British Columbia Ministry of Energy and Mines and CBM Solutions, 2005). However in the study area the Exshaw Formation and the lower part of overlying Banff Formation is interpreted to be of completely Devonian age (Richards et al., 1994). The Exshaw Formation lies unconformably above the Kotcho Formation and it is stratigraphically time equivalent to the Besa River Formation towards the Liard Basin (Figure 2.1).

From the lithological point of view, the Exshaw shale is described from cores as a black, hard, carbonaceous shale with siltstone stringers and significant amounts of pyrite. These thin siltstone layers are interpreted to be deposited during a regressive system tract that is associated with a drop of sea-level at the Devonian-Carboniferous boundary (Sandberg, et al., 1988) and resulted in a shoreface progradation. In addition, a number of localized fractures and brecciation have been observed in some cores (British Columbia Ministry of Energy and Mines and CBM Solutions, 2005). The Exshaw shale is characterized by high gamma ray values on the geophysical logs (Figure 2.3) (British Columbia Ministry of Energy and Mines and CBM Solutions, 2005).

The Exshaw Formation thickens from east to west, based on 1200 wells that have penetrated this formation (Figure 2.4). The thinnest area is located in the northeast of the HRB and it is of the order of 1 meter of thickness. The thickest part is nearly 80 m thick and is located in both the southwest and the northwest part of the basin (British Columbia Ministry of Energy and Mines and CBM Solutions, 2005). In the 3D survey area, the vertical thickness of the Exshaw Formation ranges from 5 to 15 meters and it can be found over a depth range between 1105-1120 meters

The present day structure map of the top of the Exshaw Formation is shown in Figure 2.5. It shows that the Exshaw shale generally dips from north to south. The deepest penetration of this formation, located in the southeastern area, is approximately at a depth of 3000 m and the shallowest is around 120 m, located in the northeast. The porosity ranges from 2% to 6% and the average TOC (Total Organic Carbon) content is 5% on the study area (British Columbia Ministry of Energy and Mines and CBM Solutions, 2005).

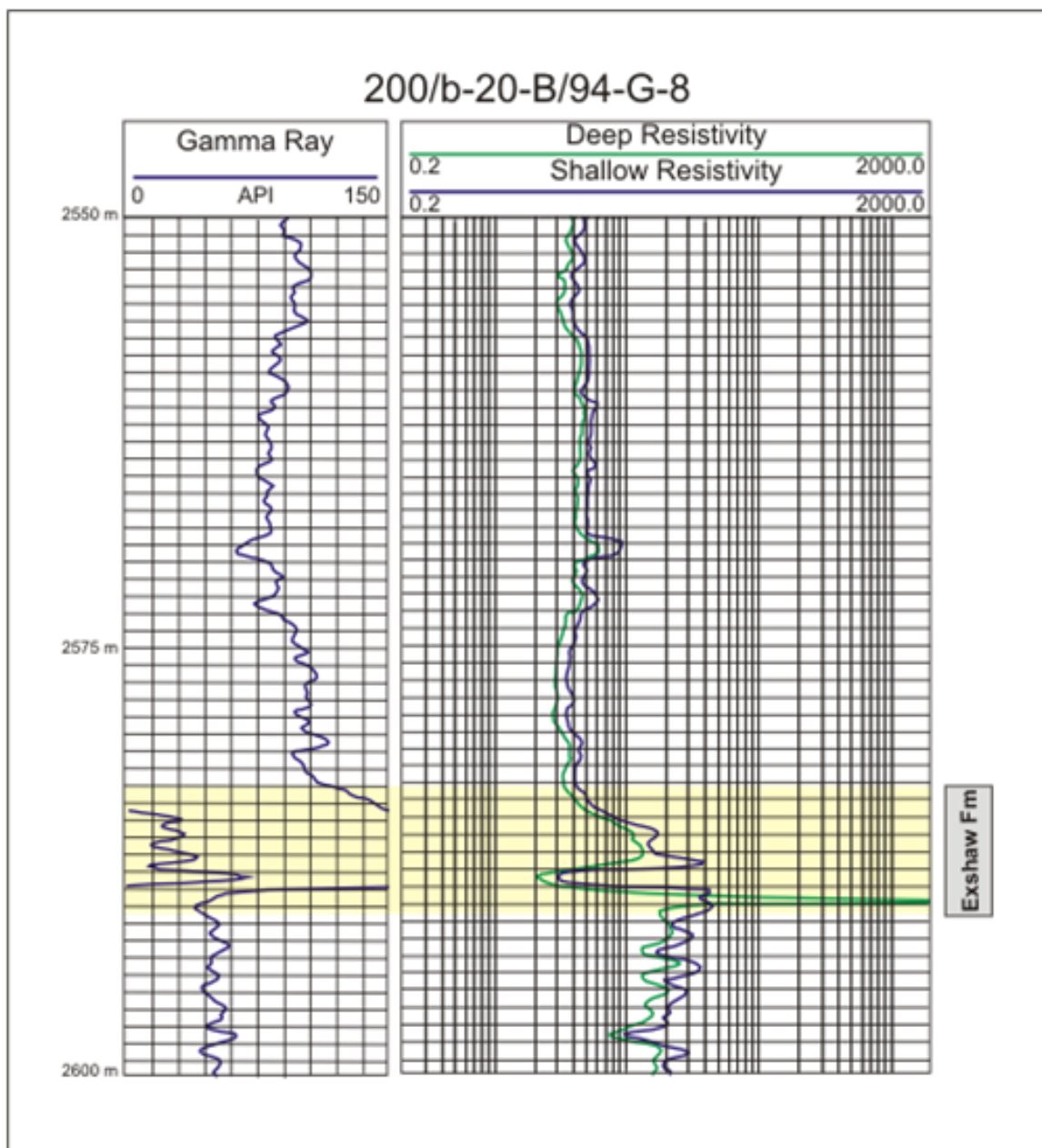


**Figure 2.3: Typical log signatures for the Exshaw Formation. High gamma ray response is characteristic (from British Columbia Ministry of Energy and Mines and CBM Solutions, 2005).**

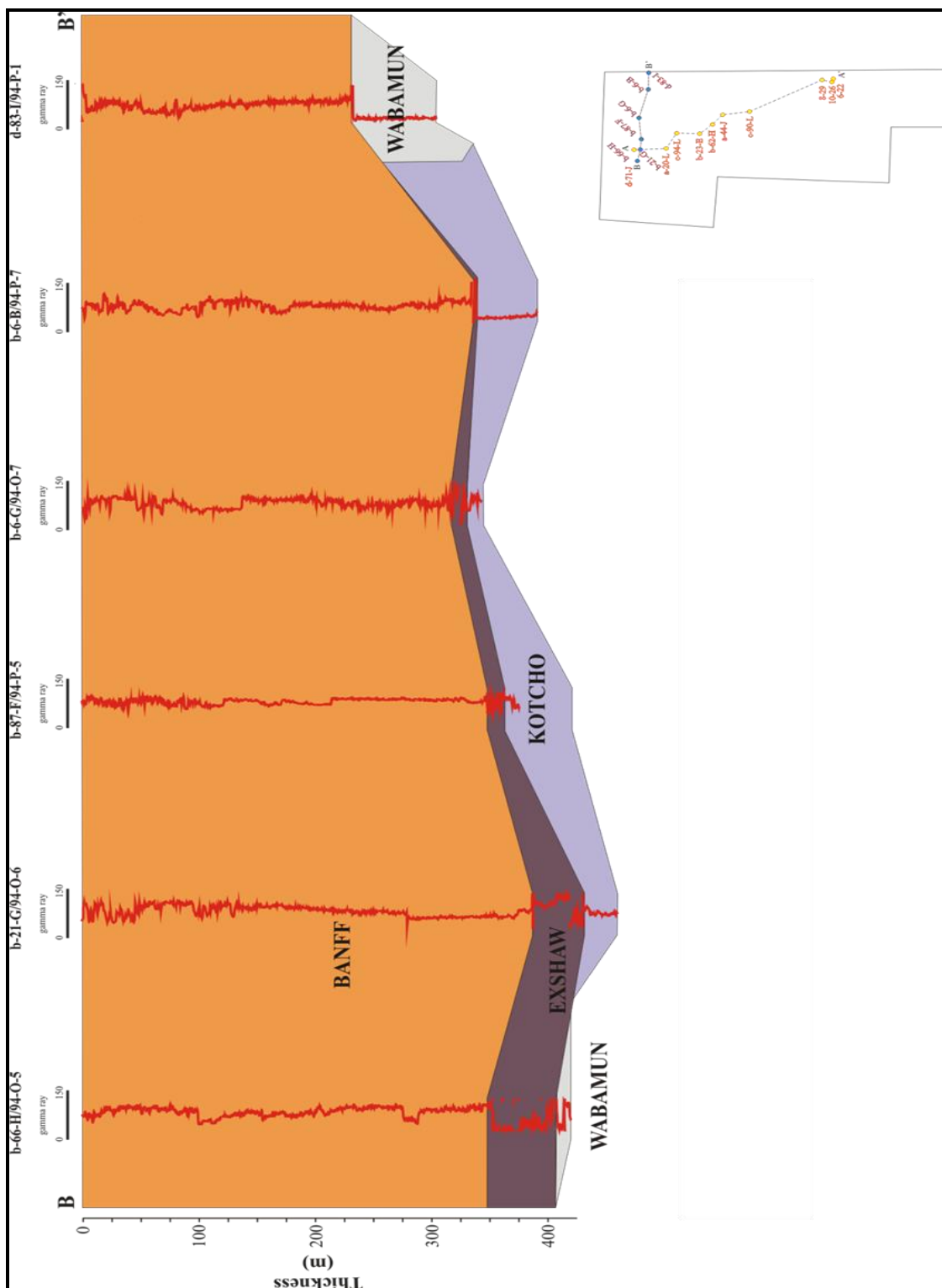


**Figure 2.4: West to east stratigraphic section of Banff and Exshaw Formations in northeastern British Columbia (B-B') (from British Columbia Ministry of Energy and Mines and CBM Solutions, 2005).**

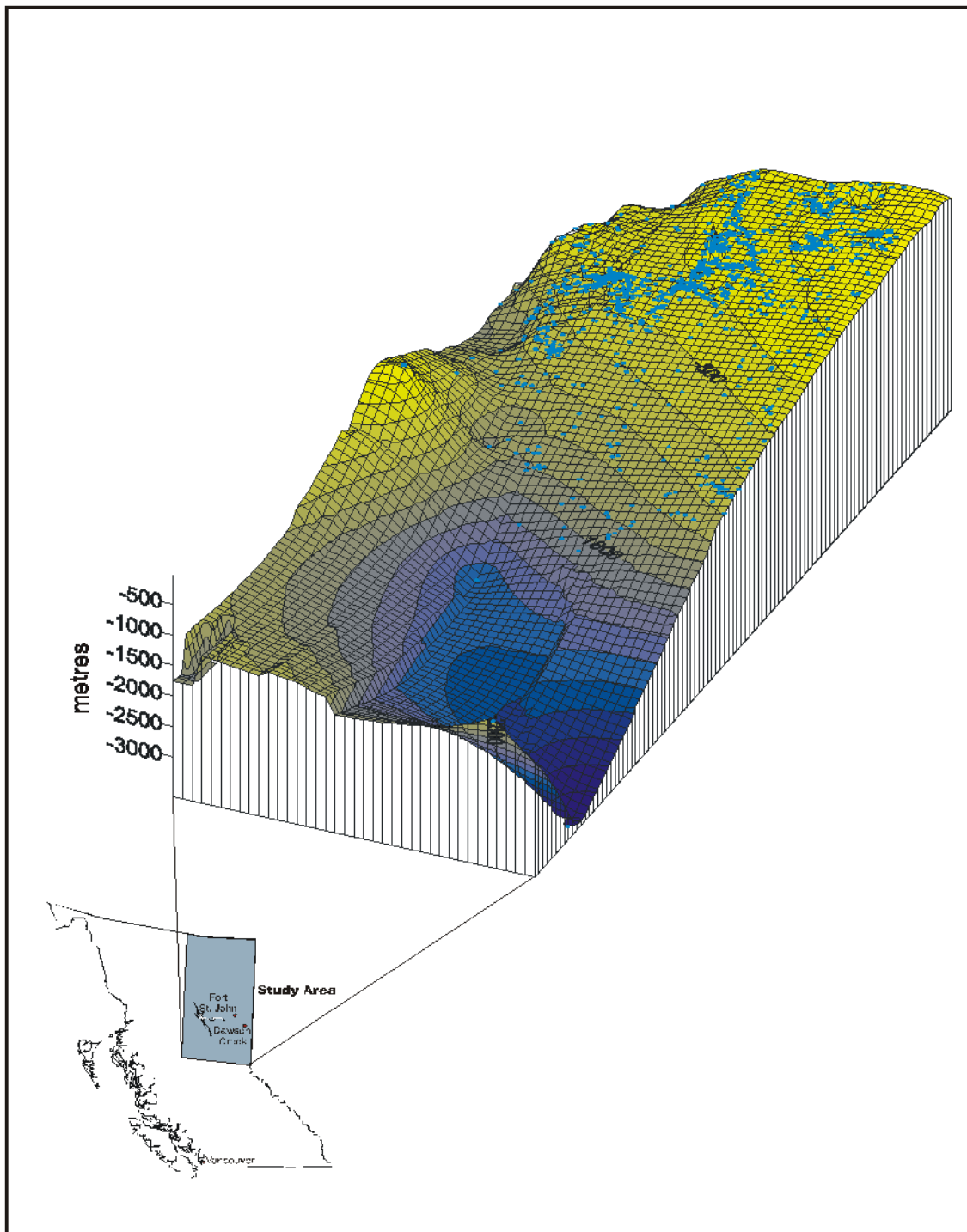


**Figure 2.5: Depth map of the top of the Exshaw Formation showing the depths from surface (from British Columbia Ministry of Energy and Mines and CBM Solutions, 2005)**

## **2.4 Muskwa Formation**

The Muskwa Formation was interpreted initially as a member of the Middle Devonian Horn River Basin Formation (Gray and Kassube, 1963). However, Griffin, (1965) studied the Muskwa shale and he suggested that it is a separate formation. Torrie (1973); Savoy and Mountjoy (1995), suggested that the Muskwa Formation was deposited in high sea level periods on the continental shelf regions. Morrow and Geldsetzer, (1988), related the extensive deposition and the preservation of these organic rich matrs of the Muskwa Formation, to a starved basin that originated by low sedimentation rates and increased subsidence through its depositional history. The Muskwa shale is characterized by high gamma ray values which correlate to high organic content (Figure 2.6) (British Columbia Ministry of Energy and Mines and CBM Solutions, 2005).

The Muskwa Formation is conformably topped by the Fort Simpson Formation (Figure 2.6), and unconformably overlies both the Slave Point Formation in the north of the study area as well as the Otter Park Formation in the south of the study (Figure 2.7), (British Columbia Ministry of Energy and Mines and CBM Solutions, 2005). The Duvernay Formation is the time equivalent to Muskwa Formation toward the east. The Muskwa Formation thickens from southeast to northwest, based on the wells that penetrated this formation (Figure 2.7). The thinnest part is located in the southeast area, whereas the thickest part (up to 75 meter of thickness) is located in the northwest area (Figure 2.7) (British Columbia Ministry of Energy and Mines and CBM Solutions, 2005).

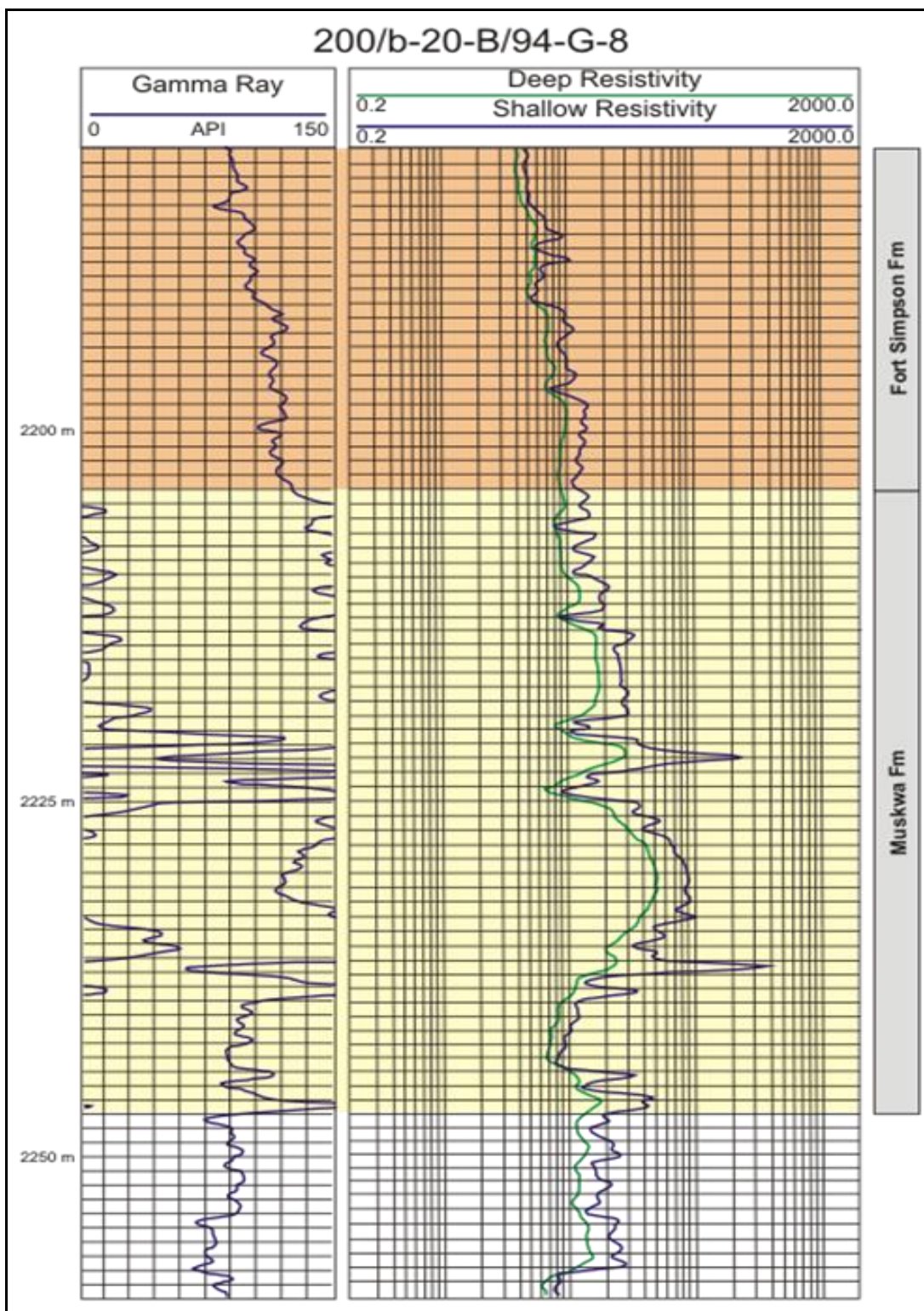


**Figure 2.6: Typical log signatures of the Muskwa Formation which is highlighted in yellow (from British Columbia Ministry of Energy and Mines and CBM Solutions, 2005)**

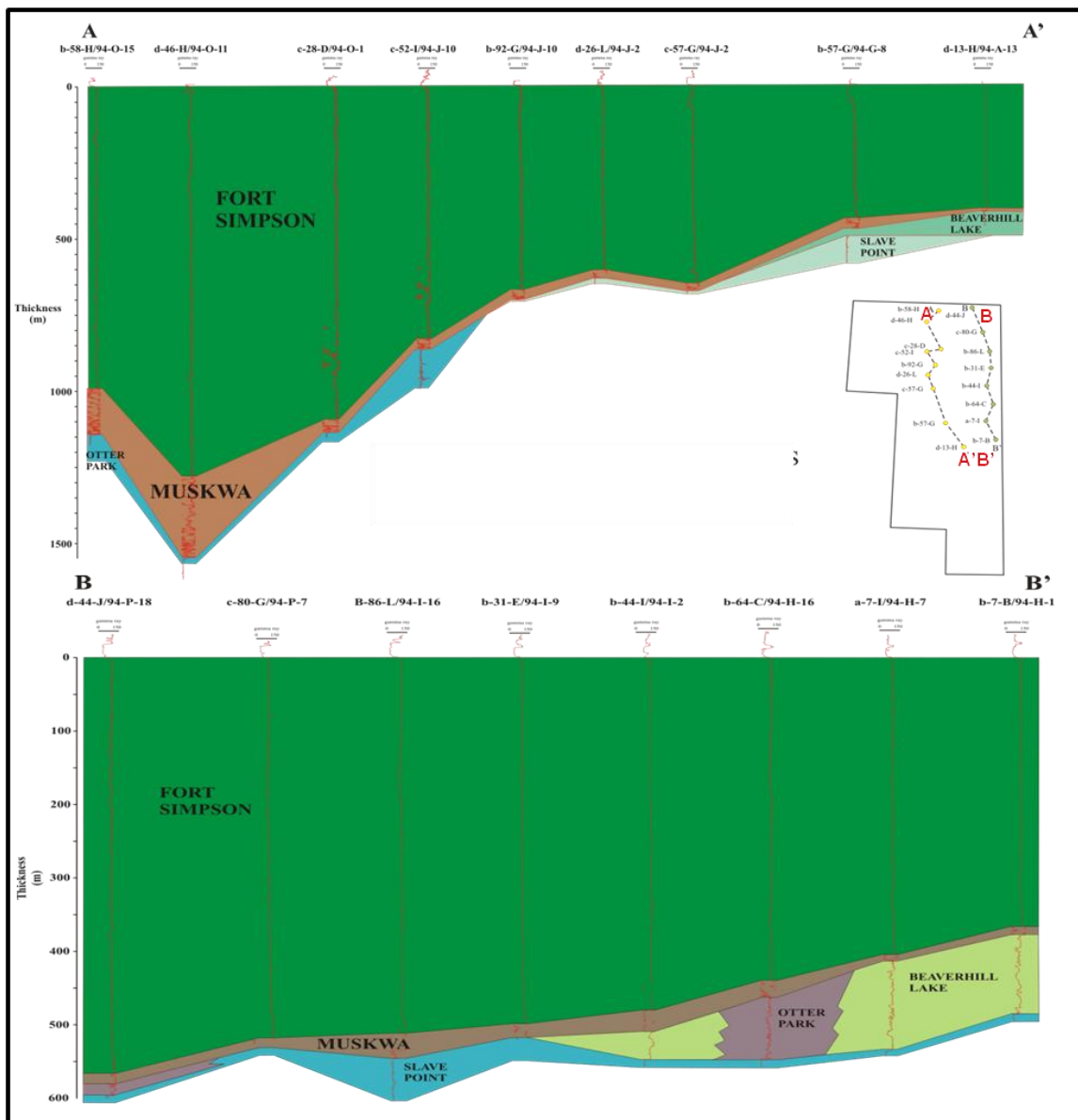


**Figure 2.7: North to south stratigraphic cross section of the Muskwa Formation in the eastern portion of the study area (A-A') (B – B') (from British Columbia Ministry of Energy and Mines and CBM Solutions, 2005).**

In the 3D study area, the vertical thickness of the Muskwa Formation ranges from 25 to 50 meters and it can be found over a depth range between 2175-2250 meters.

Structurally, the Muskwa Formation dips from north to south. The deepest penetration of this formation, located in the southern area, is approximately 3000 m and the shallowest is around 200 meters, located in the northeastern part of the basin.

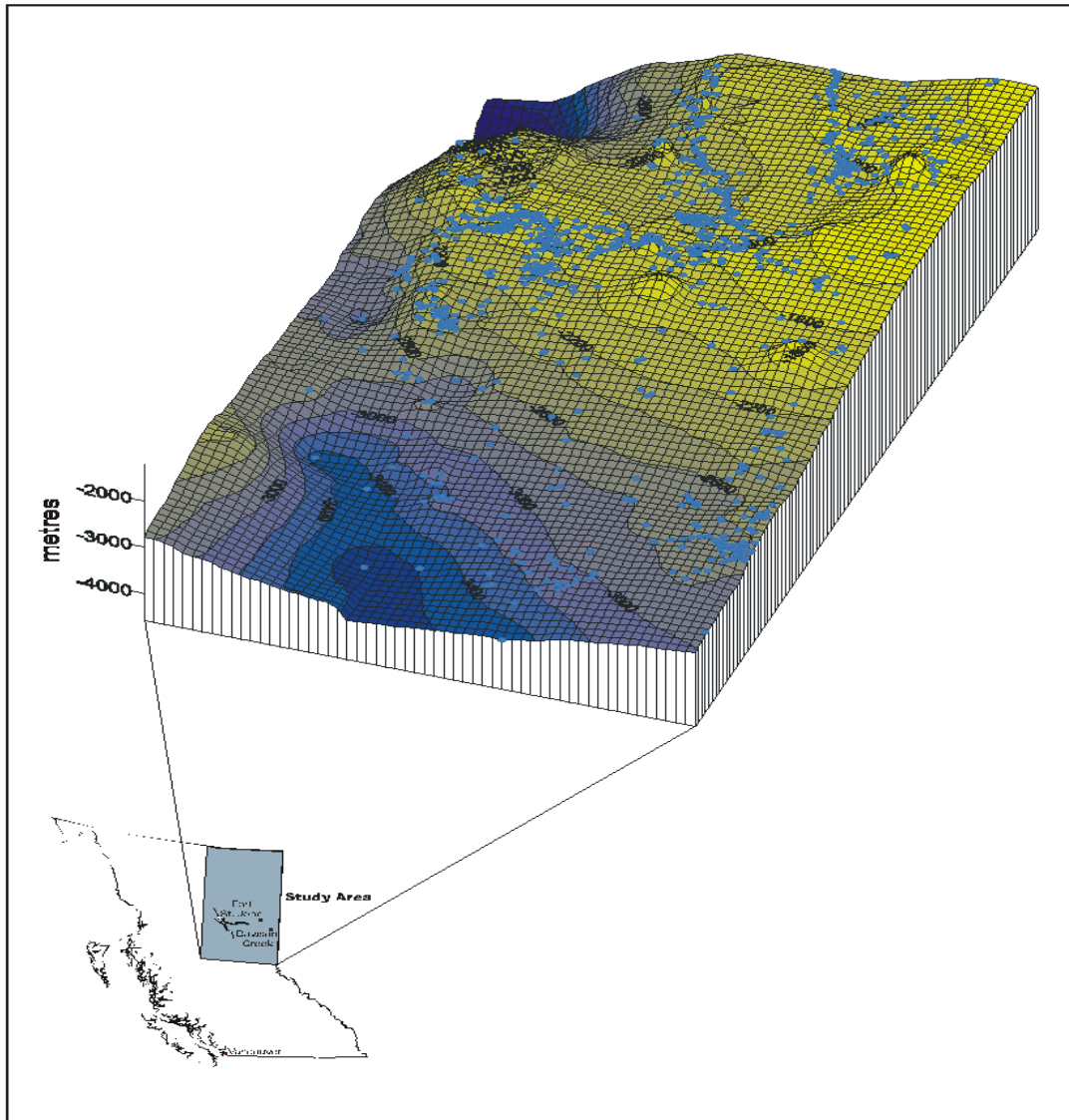


**Figure 2.8: Upper surface of the Muskwa Formation showing the drill depths from surface (British Columbia Ministry of Energy and Mines and CBM Solutions, 2005).**

The porosity of the Muskwa Formation ranges from 2% to 4.5% and the average TOC (Total Organic Carbon) content is 3.1% with a maximum of approximately 5.9% in the study area (British Columbia Ministry of Energy and Mines and CBM Solutions, 2005).

## 2.5 PP interpretation

Olympic Seismic Ltd acquired the 3D3C dataset that was interpreted for this study. It was recorded as a multicomponent survey and was processed by Sensor Geophysical Ltd. Only one well was available for the seismic-well tie in this survey and it is called well A. It is the only well located within the survey and contains a log dataset of the gamma ray curve, density curve and P wave velocity curve. The S wave curve has been calculated using Castagna's equation (Equation 2.1), where the velocities are in km/s:

$$V_p = 1.16V_s + 1.36 \quad (2.1)$$

This relation is generally defined as the mudrock line (Castagna et al., 1985). Figure 2.9 shows a least-squares fit of the P wave and S-wave velocities from another well near the survey area which has a dipole sonic log. The crossplot results in a slope of 1.32 and an intercept of 1.34 which are very similar to the parameters defined by Castagna et al (1985) in equation 2.1 and the shear wave velocity for well A calculated using the following equation (for  $V_p$  and  $V_s$  in km/s):

$$V_s = \frac{V_p - 1.34}{1.32} \quad (2.2)$$

Both seismic and well data were imported into the Kingdom Suite and Hampson Russell software. A synthetic seismogram was computed to tie the PP seismic volume to the formation tops as the first step of seismic interpretation. Seismic reflections were

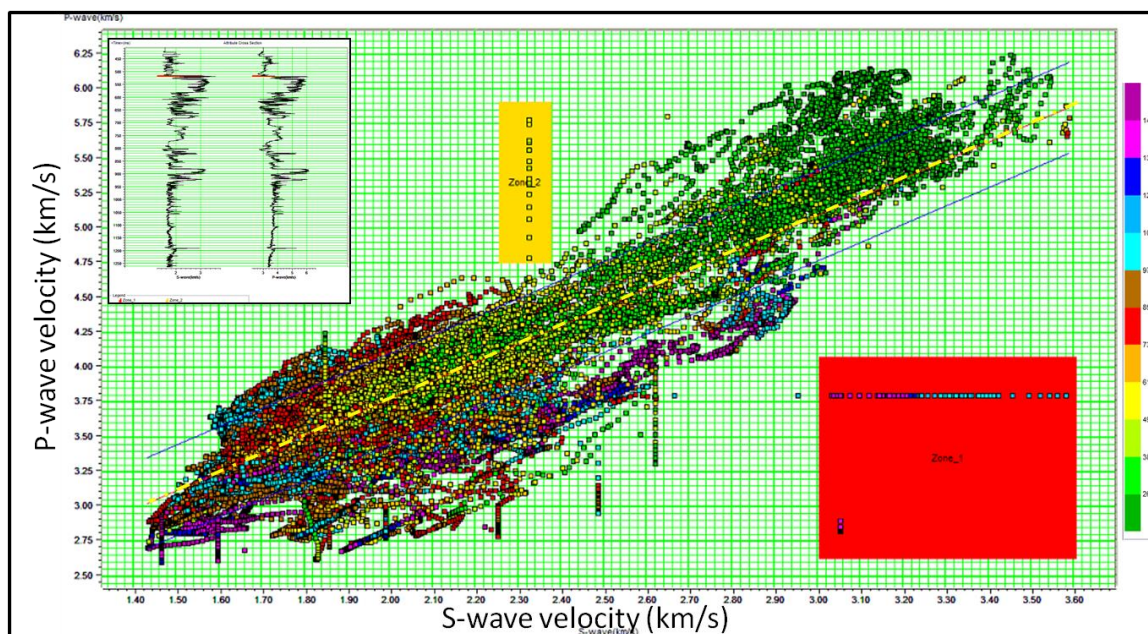


**Figure 2.9: P-wave velocity versus S-wave velocity crossplot for a well near the 3C-3D survey. The mudrock line is indicated by dashed yellow line. The upper left corner shows the vertical cross section of all points and the highlighted zone1, and zone2 indicated by red and yellow rectangular; respectively. The color bar indicates gamma-ray values.**

correlated to well formation tops first by matching the P-wave and density logs to the seismic datum. Figure 2.10 shows the statistically extracted wavelet from the PP volume using PROMC-Hampson Russell software. Later, this wavelet was convolved with the reflectivity log calculated from the density and P-wave logs to create a PP synthetic seismogram. Figure 2.11 shows the seismic-to-well tie and the correlation between synthetic seismogram and the PP stacked data is quite good for shallow intervals (Exshaw shale, 0.818 seconds) and good at the deep target (Muskwa shale, 1.405 seconds).

A detailed view of the logs within the Exshaw shale reservoir is shown in Figure 2.12. From left to right displayed curves are: gamma-ray (green), P-wave velocity (red), S-wave velocity (dark red), density (blue), acoustic impedance (pink), computed reflectivity (black), the synthetic seismogram (blue), seismic traces extracted from the PP

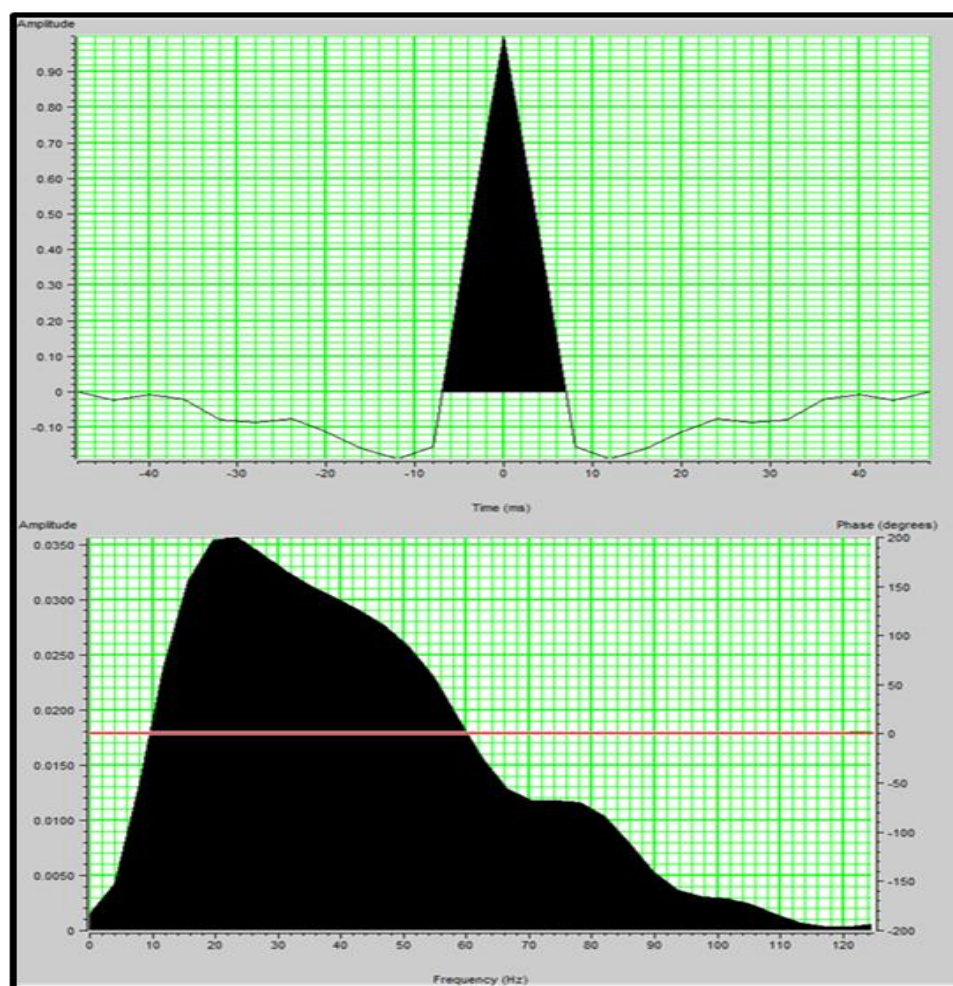


**Figure 2.10: Statistically extracted wavelet from PP volume for seismic-well tie, the top shows the wavelet in time domain and bottom in frequency domain.**

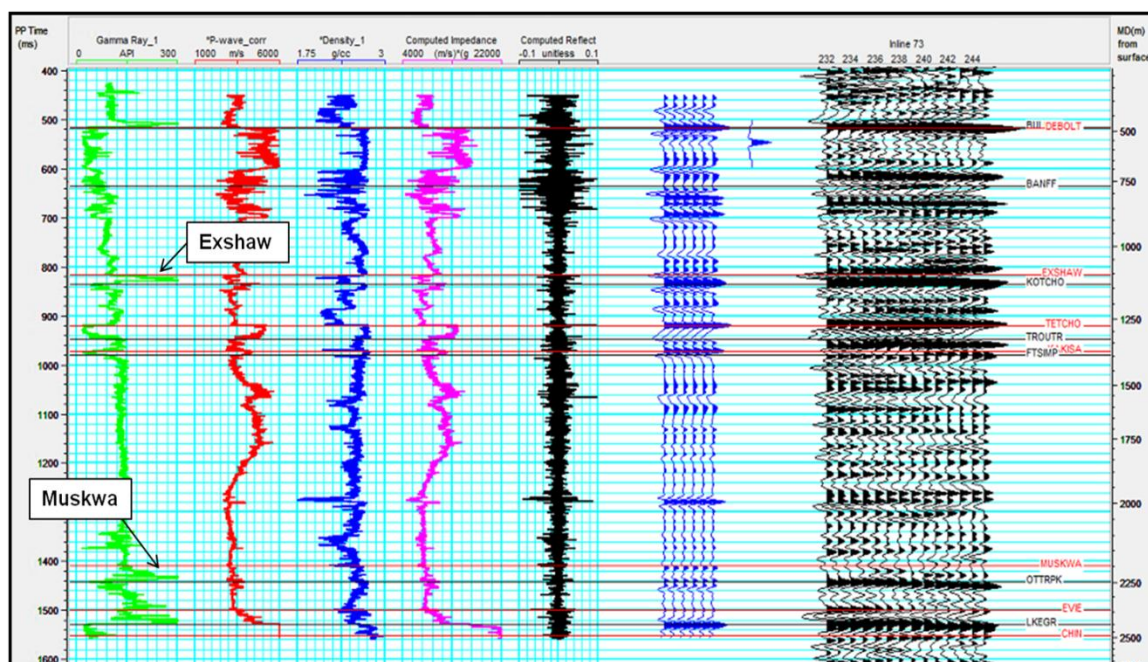


**Figure 2.11: Seismic-well tie for PP data showing from left to right: Gamma-ray (green), P-wave velocity log (red), density log (blue), calculated impedance log (pink), reflectivity (black), the synthetic seismogram with six traces (blue), the extracted wavelet and 14 traces that have been extracted from the 3D dataset for the PP volume near the wellbore (black).**

volume near the wellbore area, and computed  $V_p/V_s$  (red). Note that the top of Exshaw shale reservoir was picked on a trough and shows an increase in the gamma-ray values, a decrease on the P-wave velocity, a density decrease, a decrease in the computed impedance, and an increase in  $V_p/V_s$ . The Exshaw shale in this well is about 27 m thick with an interval time of 17 ms on the seismic section. The Exshaw shale is characterized by low density values, ranging from 2020 to 2700 kg/m<sup>3</sup> with an average density of 2400 kg/m<sup>3</sup> (Figure 2.12). The P-wave velocity shows a very significant decrease from 4000 m/s of lower Banff Formation to 3039 m/s of the Exshaw shale. The calculated S-wave velocity from equation (2.2) decreases from 1900 m/s of Lower Banff Formation to 1518 m/s of the Exshaw shale.  $V_p/V_s$  give the best differentiation regarding the lithology:

values from 1.95 to 2.05 for both the Exshaw shale and the overlain lower Banff shale and values from 1.84 to 1.90 for the limestone of both the overlying Banff Formation and the underlying Kotcho Formation. The average  $V_p/V_s$  ratio within the Exshaw shale is about 2.0.

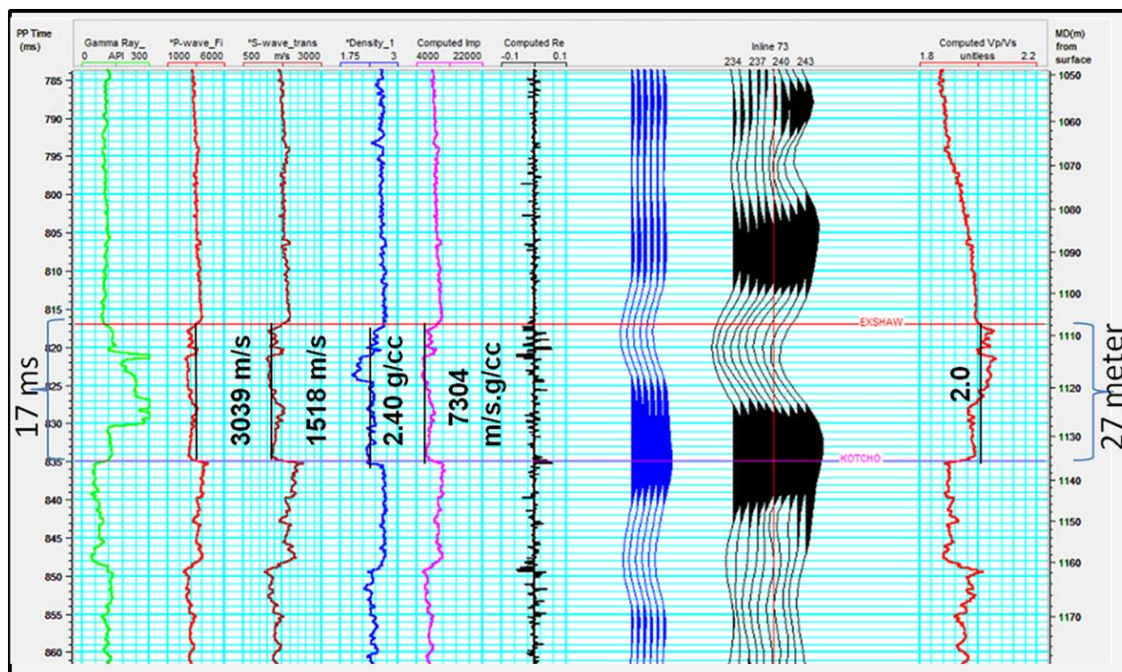


**Figure 2.12: A zoom view of logs and seismic-well tie for PP data at the Exshaw shale reservoir.**

A lithology differentiation has been attempted for well A. Shale zones are considered to have values higher than 85 API on the gamma-ray log, and  $V_p/V_s$  values more than 1.90 (Figure 2.13a and b). In Figure 2.13a, the Exshaw shale is shown in red, Lower Banff shales in orange and limestone of Kotcho Formation in blue. As has been shown in Figure 2.13 the change of  $V_p/V_s$  is attributed to the variation in shale content. As the shale content increases,  $V_p/V_s$  increases. As a result, this attribute will help us discriminate both the Exshaw shale and Lower Banff shale from the limestone of the

underlying Kotcho Formation, once we have extracted this attribute from the 3C-3D survey. However, it will be difficult to discriminate between the high gamma-ray shale from the moderate gamma-ray shale using this methodology (Figure 2.13).

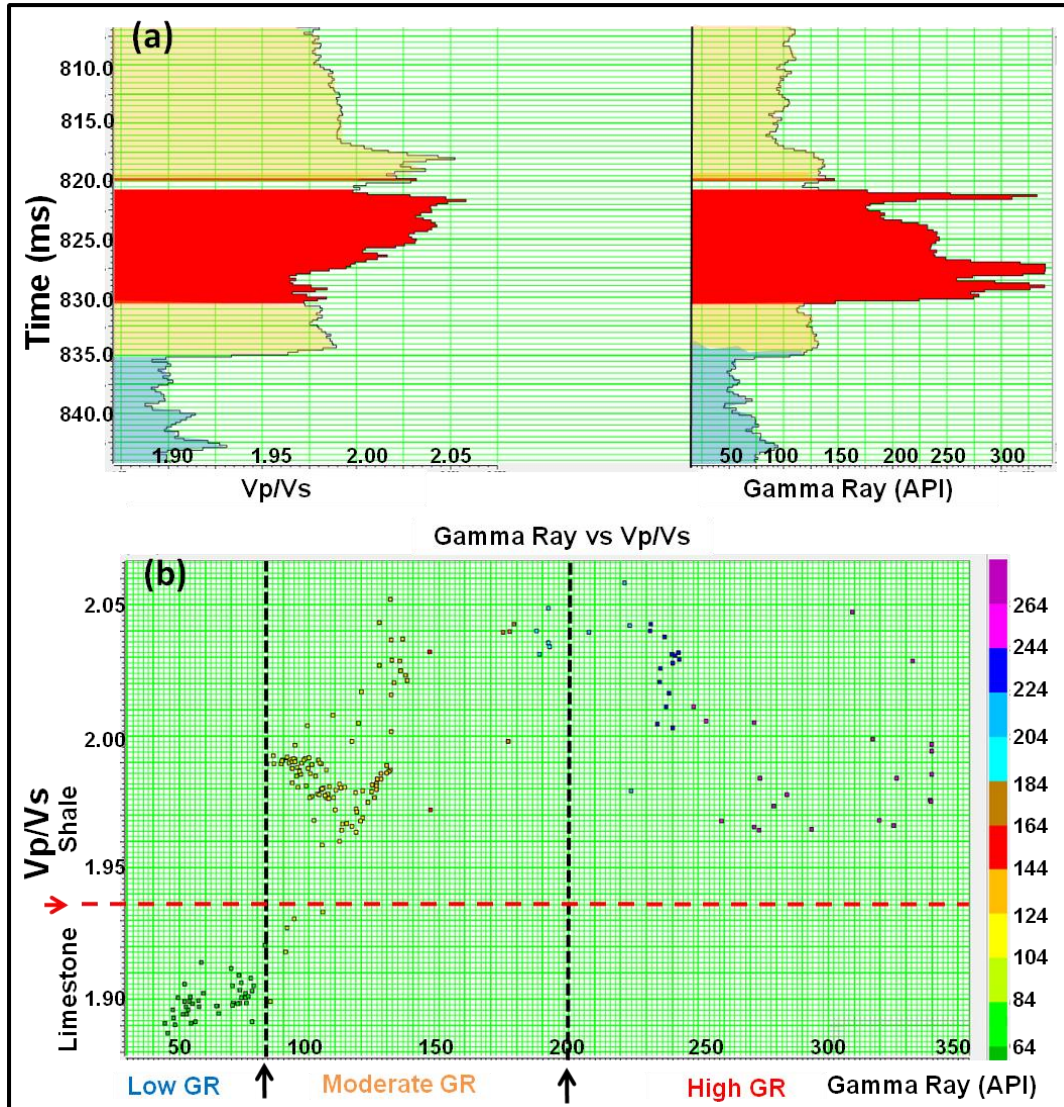
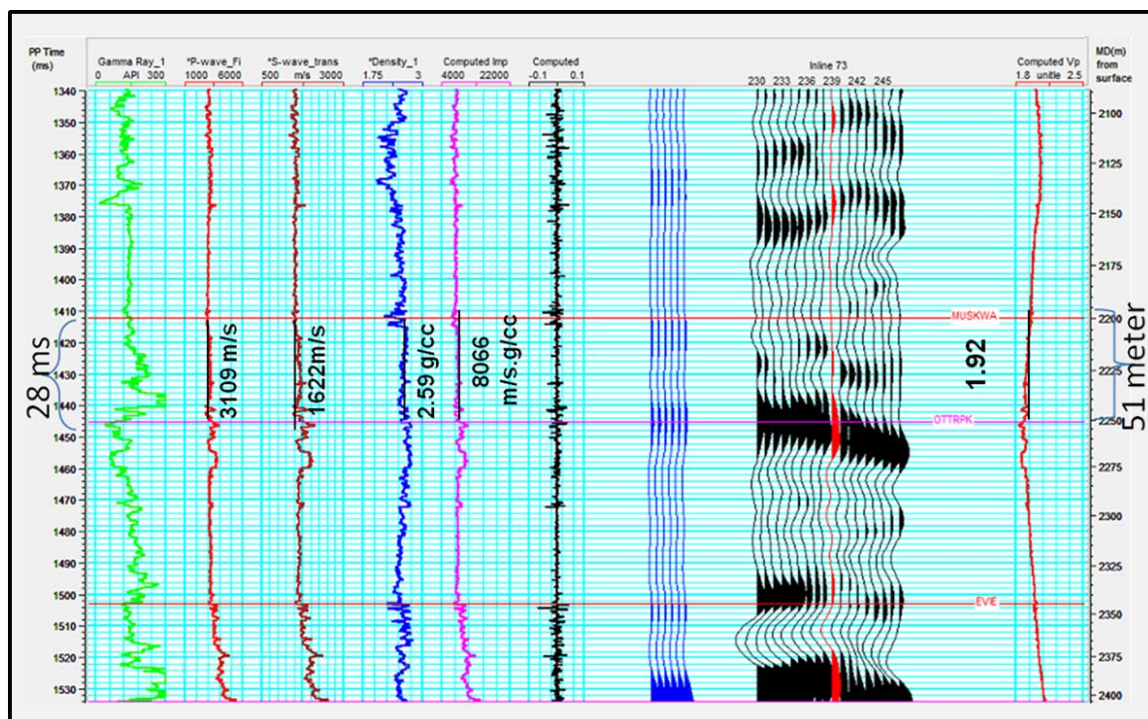


Figure 2.13: (a) Log plots showing Gamma Ray and Vp/Vs for well A; the red color highlights the high gamma-ray values of the Exshaw shale that exceeded the 150 API, the orange color indicates the gamma-ray value less than 150 API value and higher than 75 API of both Exshaw shale and Lower Banff shale, and the shaded blue color point towards the limestone of the Kotcho Formation which has the values less than 75 API, (b) Crossplot: Vp/Vs versus GR. The color bar (right) shows the GR values in API.

In comparison, the Muskwa shale is about 51 m thick, with a time thickness of 28 ms in the seismic volume. Figure 2.14 shows detailed view of the logs within the Muskwa shale reservoir. Logs from left to right are the following curves, gamma-ray (green), P-wave velocity (red), S-wave velocity calculated from equation 2.2 (dark red), density (blue), acoustic impedance (pink), computed reflectivity (black), the synthetic seismogram (blue), seismic traces extracted from the PP volume near the wellbore area, and the computed  $V_p/V_s$  ratio from equation 2.2 (red). Note that the top of the Muskwa shale reservoir is characterized seismically by a weak trough due to the low impedance contrast between the overlying Fort Simpson shale and the underlying Muskwa shale (Figure 2.12, Figure 2.14). Figure 2.14 shows an increase in the gamma-ray, and a slight



**Figure 2.14: A detail view of logs and seismic-well tie for PP data at the Muskwa shale reservoir.**

increase in P-wave velocity, shear velocity, density, and impedance logs. There is a slight decrease in  $V_p/V_s$  that computed from equation 2.2 (Figure 2.14). The Muskwa shale in

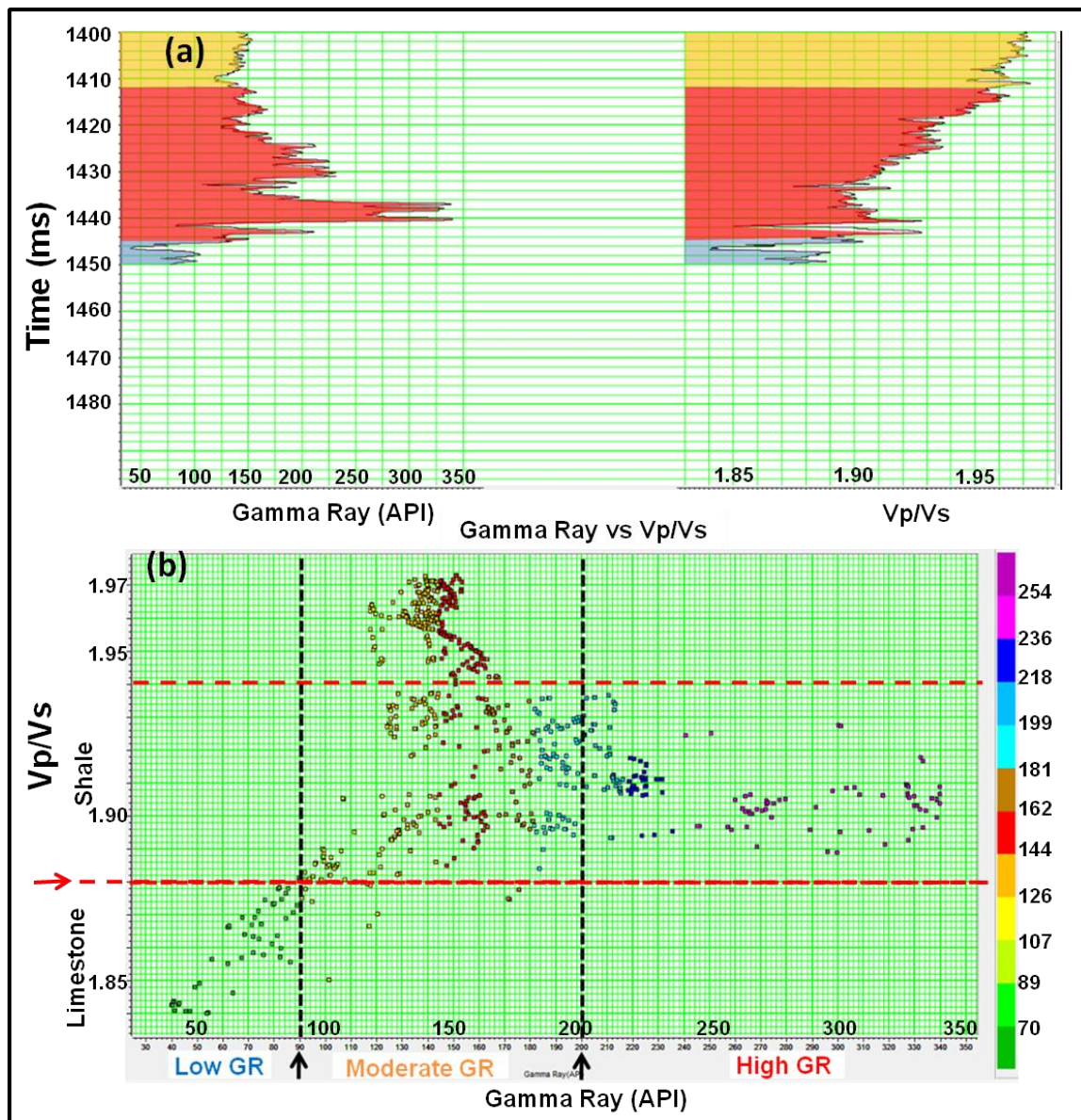


Figure 2.15: (a) Log plots showing Gamma Ray and the calculated  $V_p/V_s$  for well A from equation 2.2; the red color highlights the high gamma-ray values of the Muskwa shale that exceeded the 125 API, the orange color indicates the gamma-ray value less than 125 API value and higher than 75 API of both Muskwa shale and Fort Simpson shale. The shaded blue color indicates the limestone of the Kotcho Formation which has the values less than 75 API (b) Crossplot:  $V_p/V_s$  versus GR. The color bar (right) shows the GR values in API.

this well has an average density of  $2590 \text{ kg/m}^3$ , an average P-wave velocity of  $3109 \text{ m/s}$ , an average S-wave velocity of  $1622 \text{ m/s}$  that calculated from equation 2.2. Similar to the Exshaw shale,  $V_p/V_s$  that computed using equation 2.2, gives the best differentiation regarding the lithology.  $V_p/V_s$  higher than 1.88 are recognized for the shale of both the Muskwa Formation and the overlying Fort Simpson shale, and values less than 1.88 are attributed to the limestones of the underlying Otter Park Formation (Figure 2.15). The plot shows clearly that the high gamma-ray values of Muskwa shale characterized by low values of  $V_p/V_s$ , between 1.88 to 1.94 respectively. Interval  $V_p/V_s$  can be extracted from the 3C-3D data, and the discussion and extraction of this attribute is presented in Chapter Three.

## **2.6 Combined PP and PS interpretation**

The first step of joint interpretation of the two volumes (PP and PS) is to do seismic-well tie in the PS domain using the shear wave velocity that we generated from Equation 2.2. Figure 2.16 shows from left to right: the gamma -ray log (green), the S-wave velocity log (red), the density log (blue), and the computed shear impedance log (red). The synthetic seismogram (in blue) was created assuming an incident angle of up to 20 degrees. The wavelet was extracted from the PS (radial) migrated stack statistically and it is shown in Figure 2.17. The well log is stretched in PS time and the correlation between synthetic seismogram and the PS seismic stack is good for Exshaw shale (1.245 seconds) and fair to good at the top of Muskwa shale (2.255 seconds). Note that the computed S-wave velocity is affected by the stretching and squeezing of the log during the  $V_p/V_s$  registration. Similar to the PP volume, the top of the Muskwa shale is characterized seismically by a weak trough that is difficult to correlate throughout the 3D

survey and instead I picked its base which is in this case is the top of Otter Park Formation. It is characterized by a strong peak that is easy and reliable to pick and to track throughout the 3D survey on both volumes. On the other hand, the top of the Exshaw shale is characterized seismically in the PS section by a strong trough that can also be interpreted easily throughout the 3D survey on both volumes.

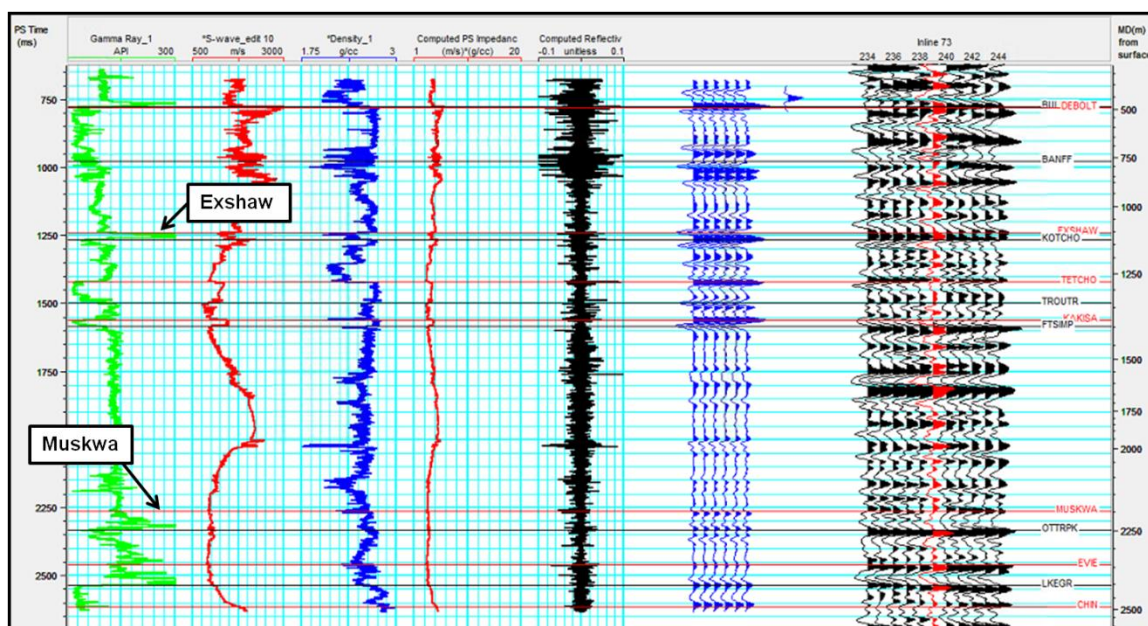


**Figure 2.16: Seismic-well tie for PS data showing from left to right: Gamma-ray log (green), S-wave velocity log calculated by Equation 2.2 (red), density log (blue), calculated shear impedance log (red), reflectivity (black), the synthetic seismogram with six traces (blue), the extracted wavelet and 12 traces that have been extracted from the 3D dataset near the wellbore (black).**

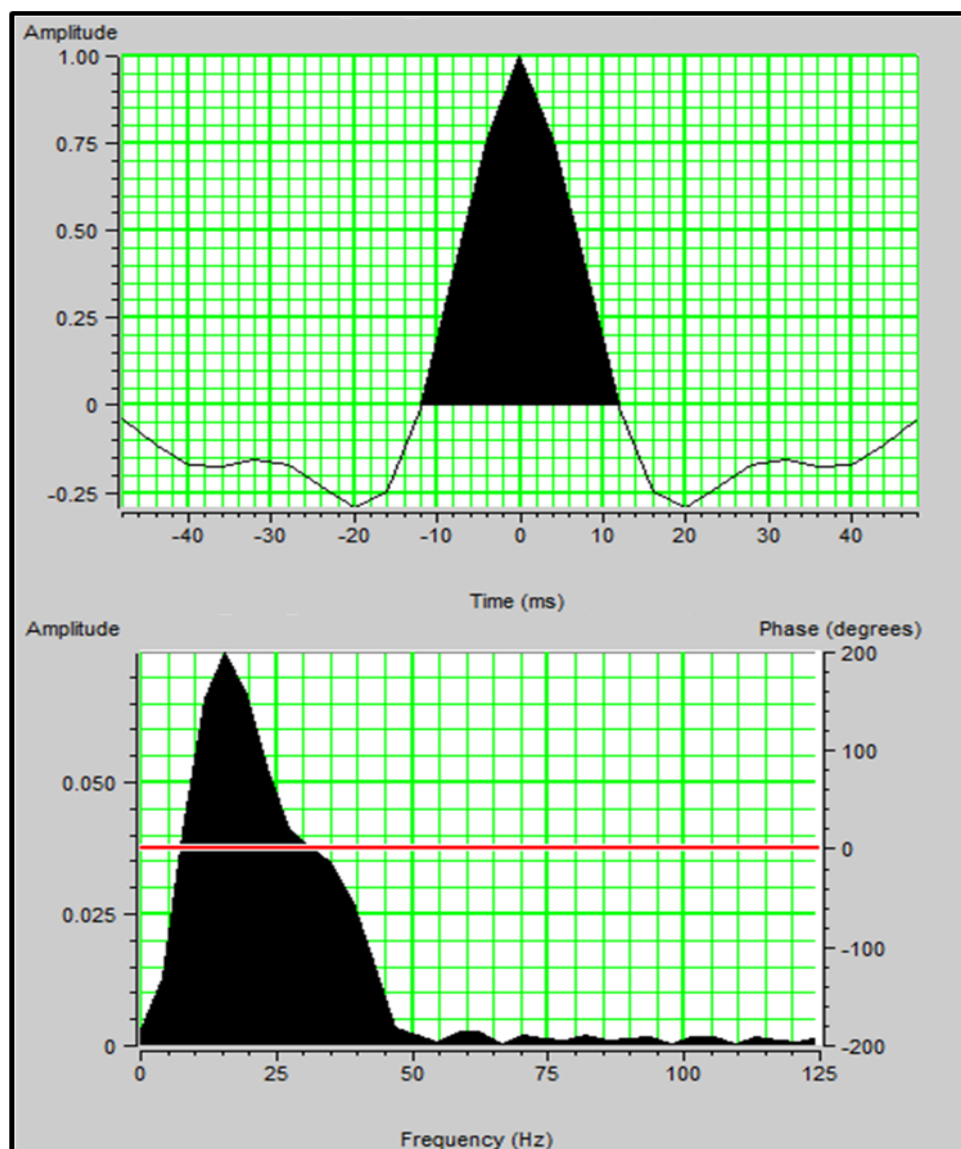


**Figure 2.17: Statistically extracted wavelet from PS volume for Seismic-well tie, the top shows the wavelet in time domain and bottom in frequency domain.**

The registration of the PP and PS volumes was done in two steps. Step one was to derive a velocity model from well A for domain conversion and step two was to match the picked horizons in both volumes. Figure 2.18 shows the seven key seismic horizons picked on PP and PS volumes. From top to bottom, there are the tops of the Debolt

Formation, the Banff Formation, the Exshaw Formation, the Tetcho Formation, the Fort Simpson Formation, the Otter Park Formation (the Base of Muskwa Formation), and the

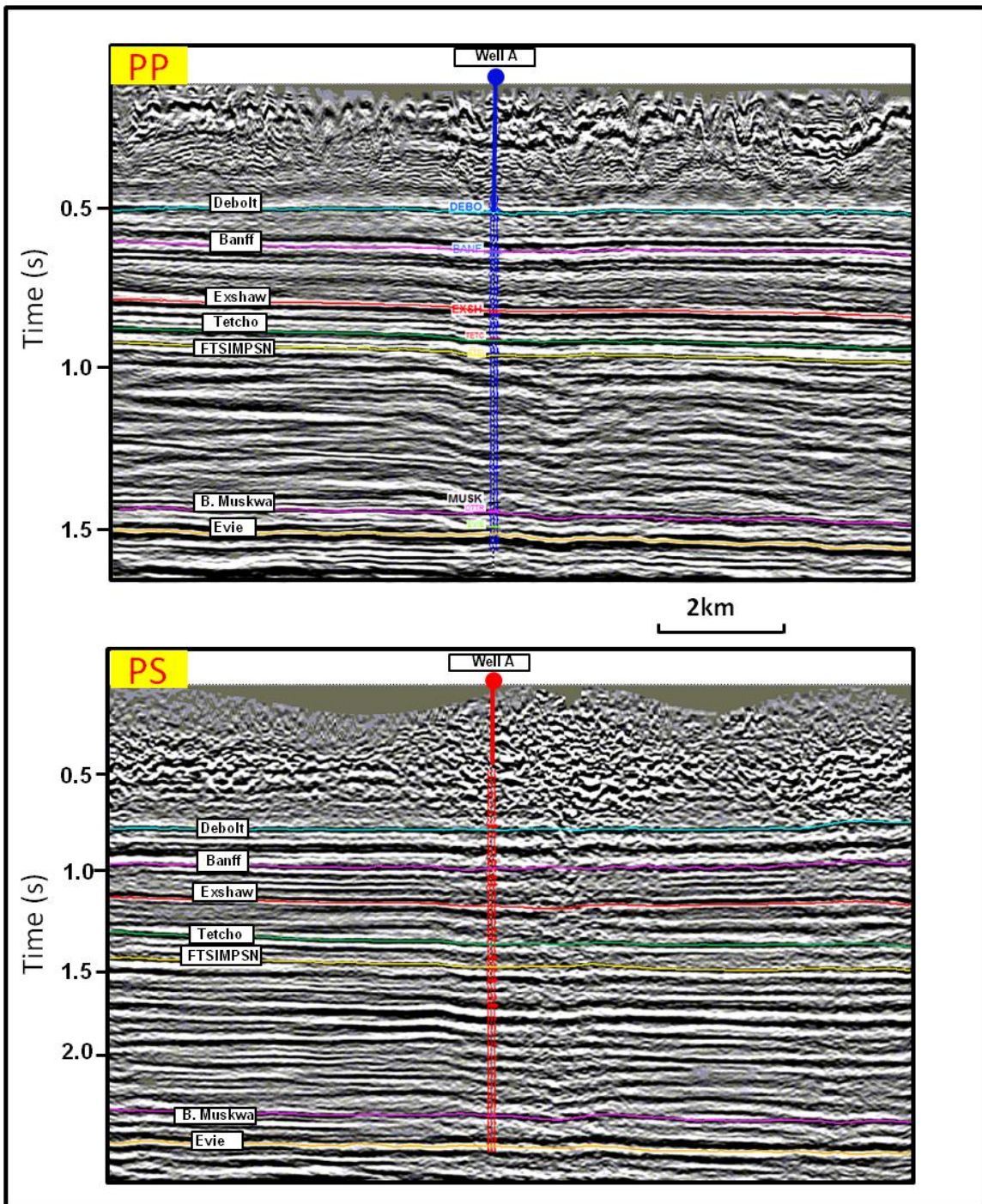
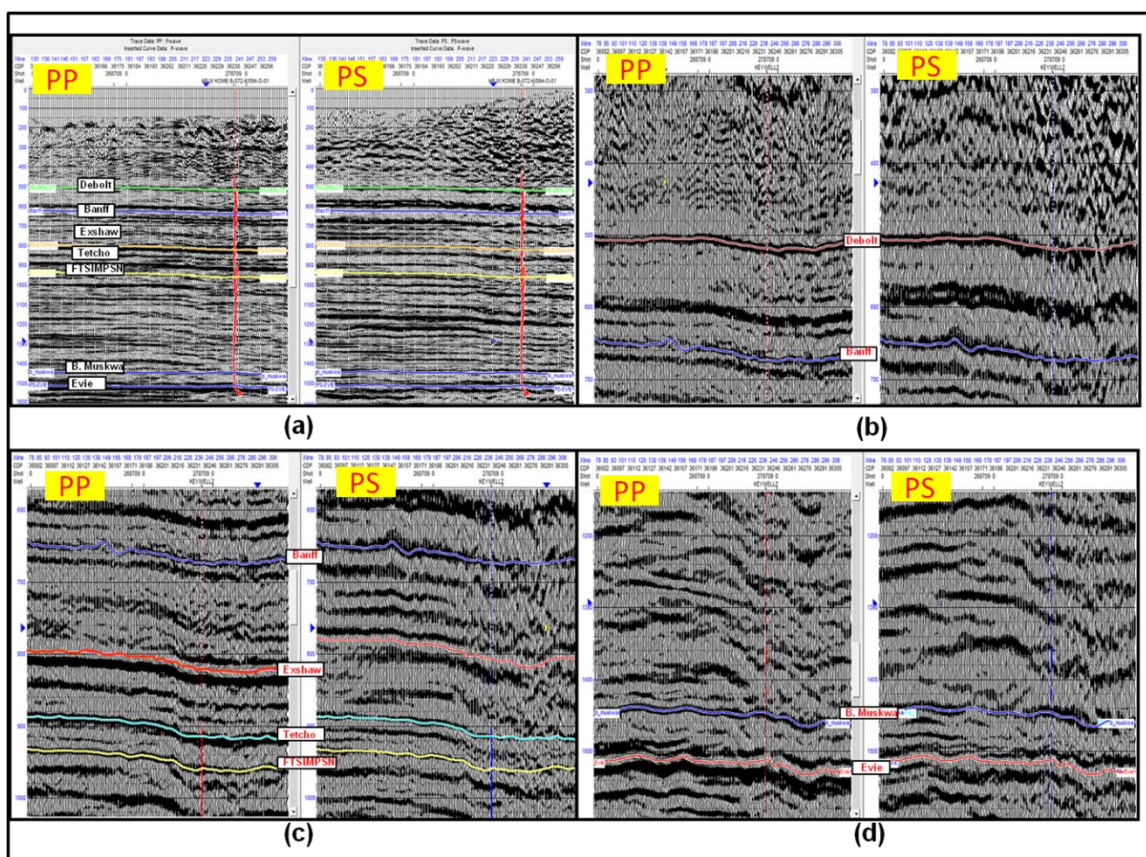


Figure 2.18: Example of in-line section from PP volume (above) and PS volume (below) showing the seismic-well tie for well A and the seven key interpreted seismic horizons.

Evie Formation. All of these seismic horizons were picked on every 40<sup>th</sup> inline and cross line. After that, an automatic pick and 3D interpolation was performed for these picks for each seismic horizon using the 3D hunt feature that provided by Kingdom Suite. Figure 2.19, shows the final registration using the PP and PS picked horizons. Note that both sections are shown in PP time, those on the left side show the PP section, and those on the right show the PS sections. The tops of the Exshaw shale PP, PS events, after horizon matching, are shown in red, and the base of the Muskwa shale horizon in blue.



**Figure 2.19** Inline 73: PP section (left) and PS section (right) stretched in PP time at well A. a) Unzoomed section after PP and PS registration (domain conversion, strata velocity model, and plus horizons matching applied). b) Zoomed view on the shallower horizons (Debolt Fm., and Banff Fm.). c) Zoomed view on the Exshaw Fm., Tetcho Fm., and Fort Simpson shale Fm. d) Zoomed view on the deep horizons (Muskwa Fm., and Evie Fm.).

After registration, two-way time PP and PS structure maps were created for the top of the Exshaw Formation and at the base of Muskwa Formation and are shown in Figures 2.20a and 2.20b respectively. These maps show the two-way time structure maps for top Exshaw shale along with the interpreted faults intersecting them. These two maps show that the Exshaw shale has a monoclinial dip toward the west, intercepted by four parallel normal faults. All these faults dip to the southwest and their strike direction is northwest-southeast. In addition, features that are believed to be artifacts generated by a significant channel system within the near surface, are indicated by dashed black lines are shown in both maps. These shallow channels are shown in refraction bedrock map (Figure 2.21). The Exshaw PS time structure map is more severely affected by these channel artifacts than the Exshaw PP time structure map (Figure 2.20). They are also visible in the example A-A` cross section in Figure 2.22. Figure 2.23 shows the four normal faults in a section along B-B`, and the faults are well imaged on both the PP section and the PS section. Note that these faults do not affect the deep horizons such the Muskwa and the Evie events.

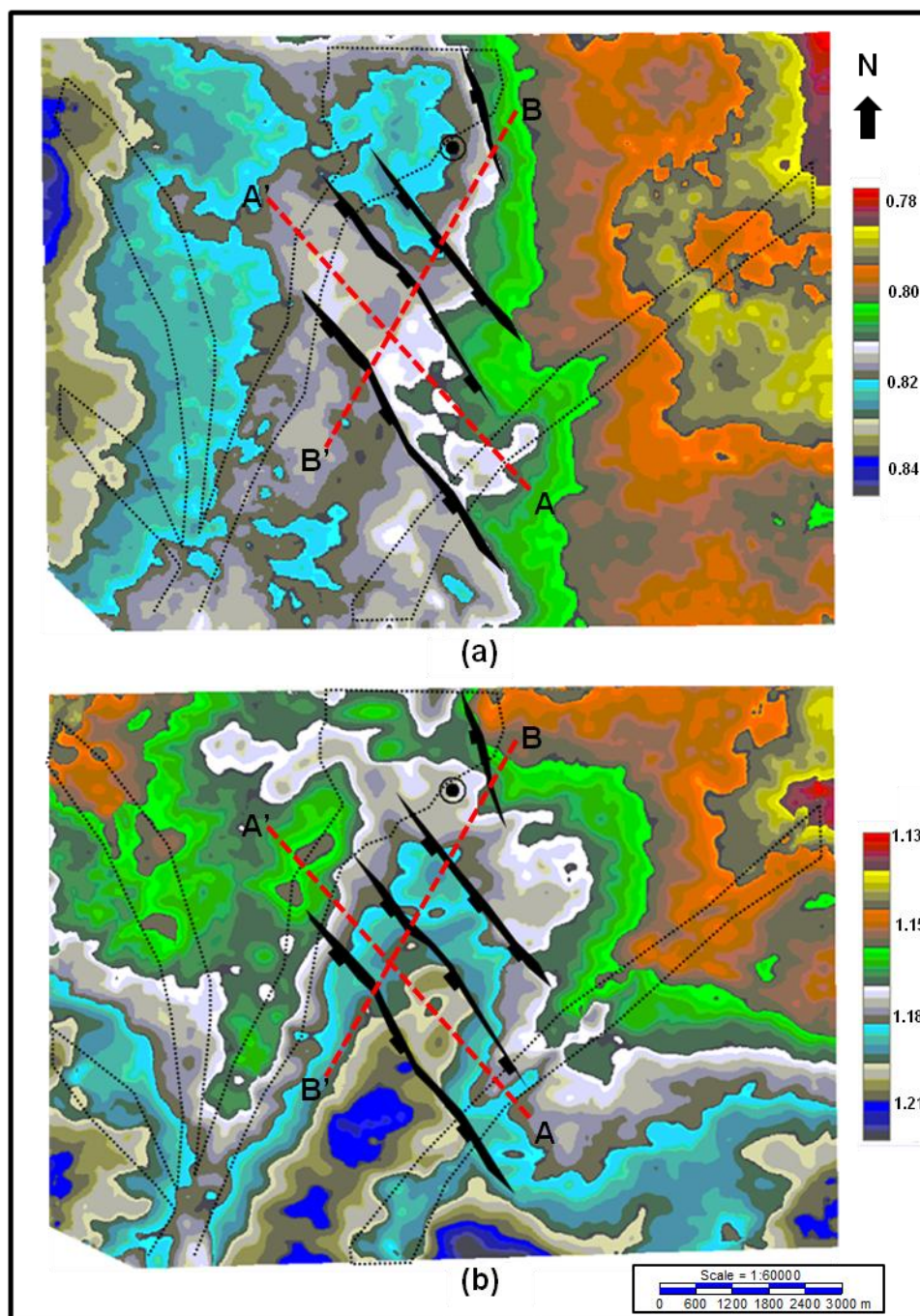


**Figure 2.20: Exshaw shale PP time structure map (a) and PS time structure map (b) showing the interpreted faults (black solid lines) that cut this surface in the area. Cross sections A-A' shown in Fig. 2.22 (through the channel artifacts) and B-B' shown in Fig. 2.23 (through the faults) are indicated by dashed red lines. The channel artifacts are highlighted by dotted black lines)**

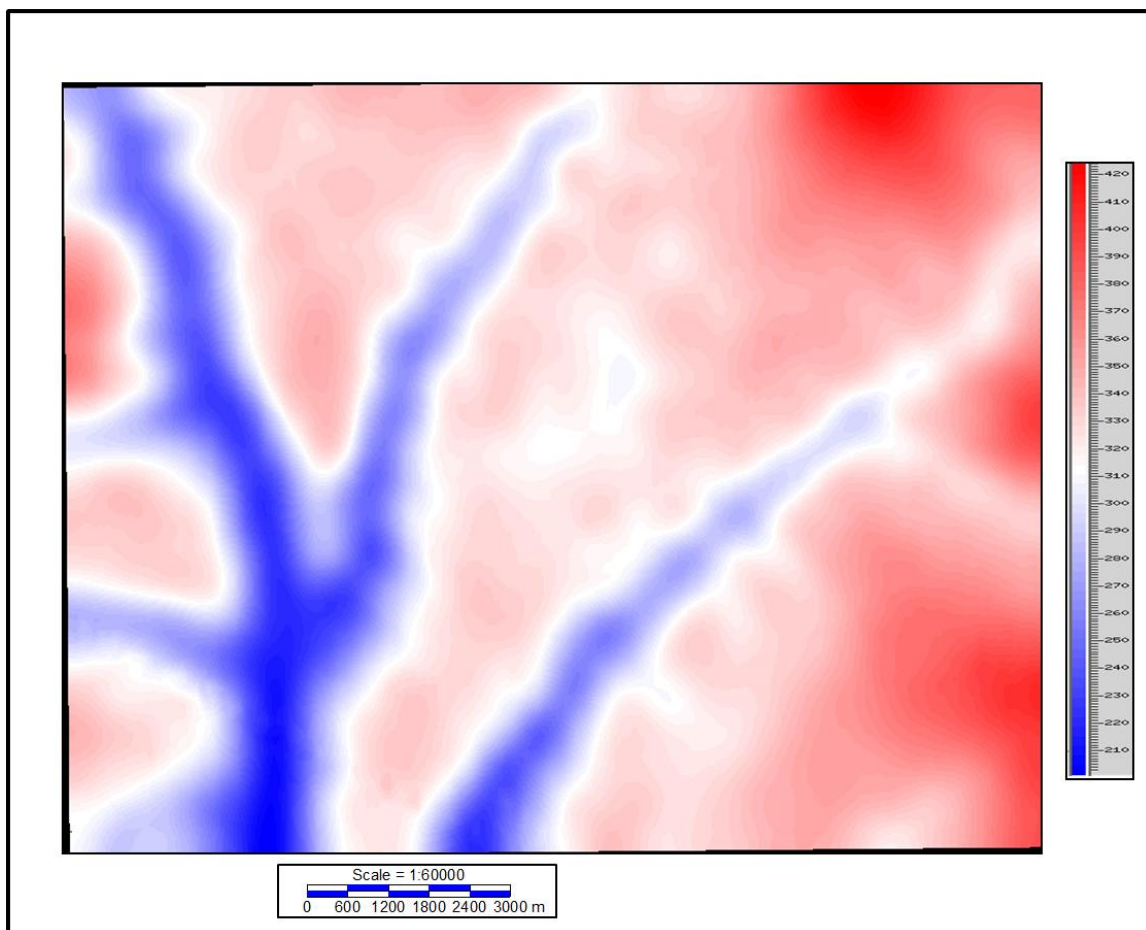


**Figure 2.21: The base of weathering map which highlights the near surface channels in blue (Olympic Seismic Ltd., 2009).**

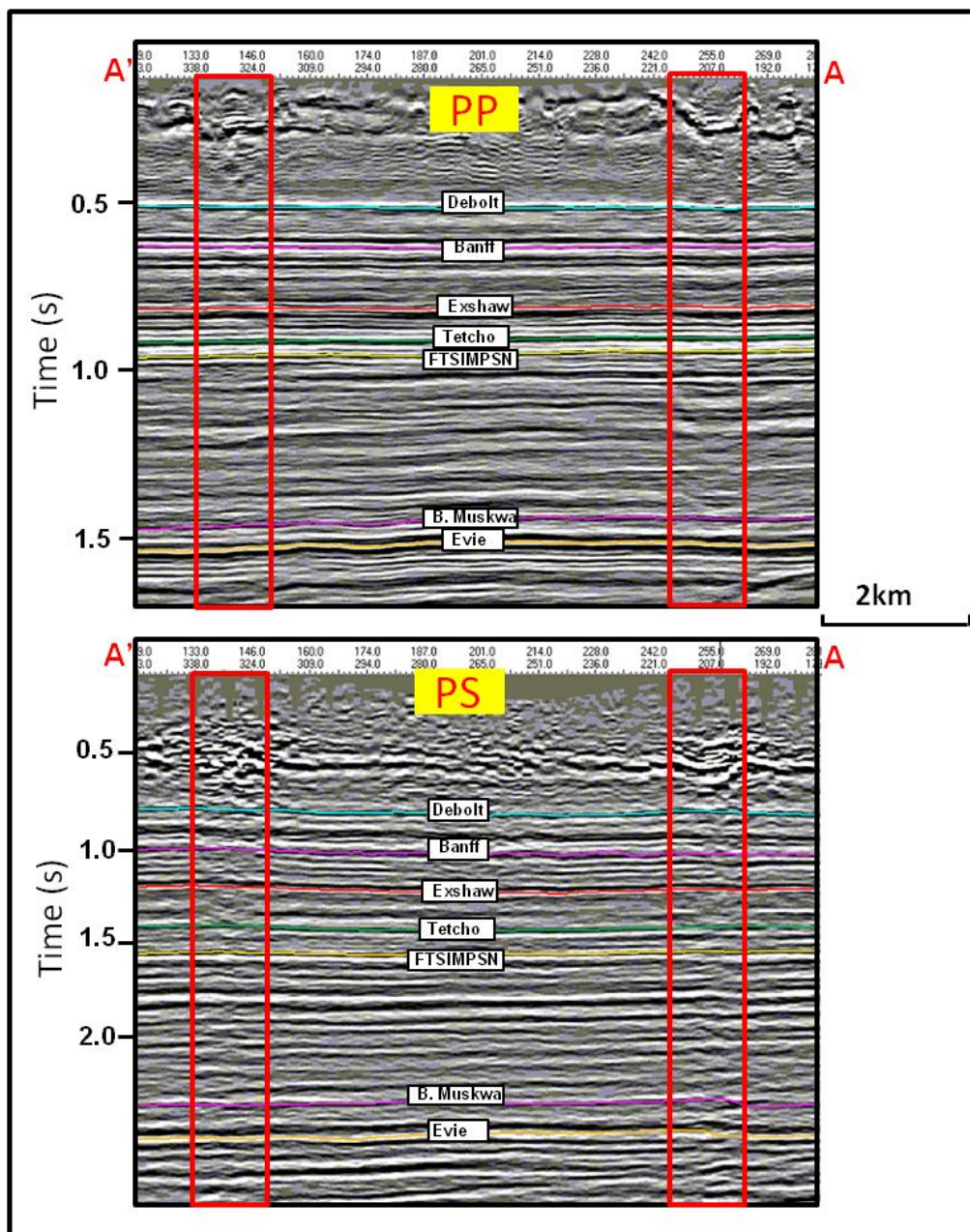


**Figure 2.22: A-A' traverse through PP section (above) and PS section (below) showing the imprint of the near surface channels (red rectangular) on the imaging below it. Refer to Figure 2.20 for the location of this cross section.**

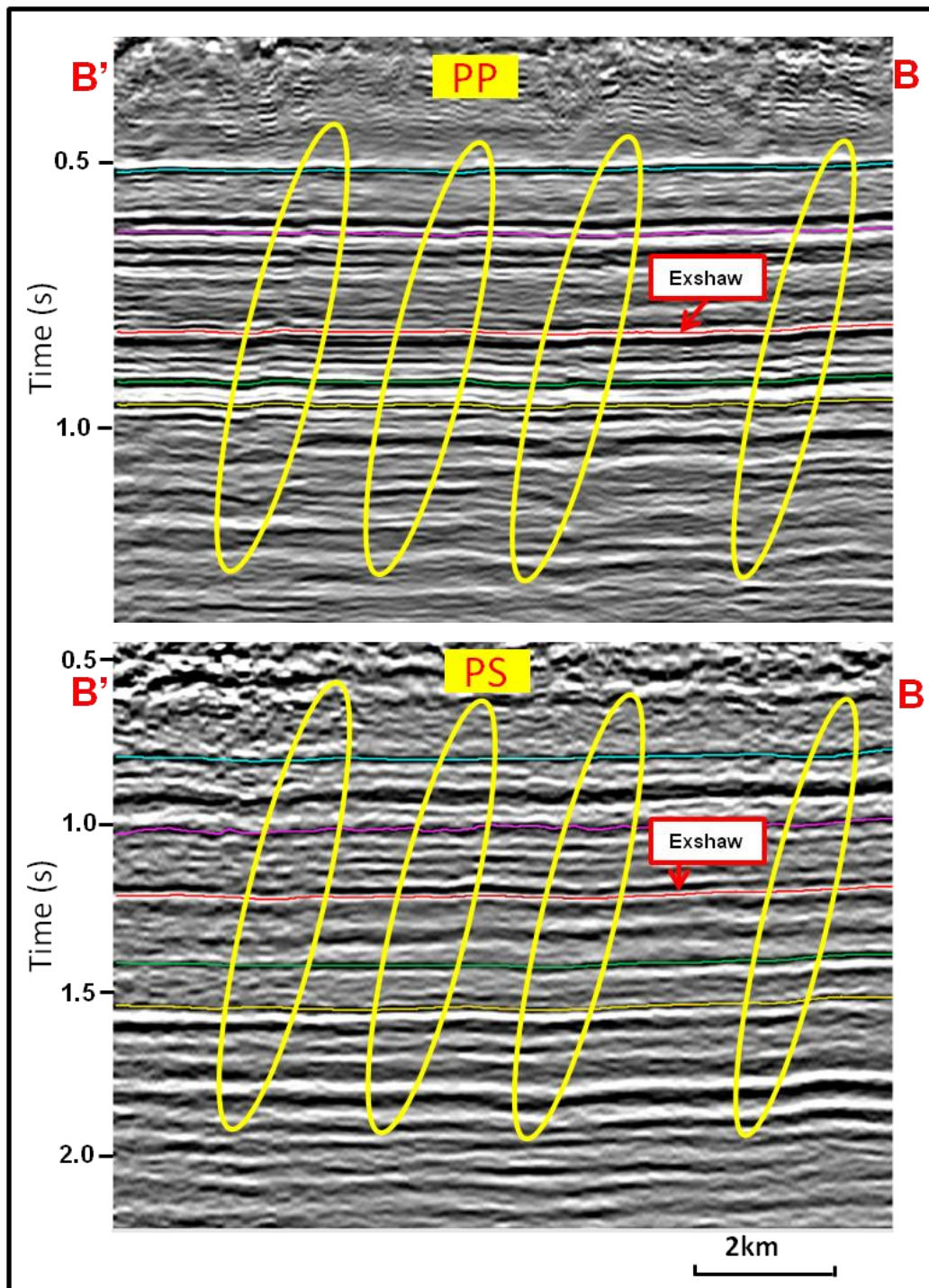


**Figure 2.23:** B-B' traverse through PP section (above) and PS section (below), showing the four normal faults (yellow ellipses) that cut the shallow horizons including the Exshaw shale. Refer to Figure 2.20 for the location of this cross section.

The interpretation is quite different for the deeper Muskwa Formation. One normal fault, one reverse fault and one strike slip fault have been interpreted at this level (Figure 2.24). Figures 2.25, and 2.26 show the traverses C-C` and D-D`, respectively that show these faults in vertical sections. The locations of these traverses are shown in Figure 2.24. All these faults are basement related faults (Figures 2.25 and 2.26). The reverse fault dips northwest and trends northeast-southwest, forming a small four-way anticline closure. The anticline axis is parallel to the strike direction of the fault (Figure 2.24). Figure 2.26 shows the fault and its displacement. The normal fault dips toward the east and its strike direction trends north-south (Figures 2.24 and 2.25), similar to the Bovie Fault, whereas the strike slip fault has left lateral movement and trends northwest-southeast and does not show any vertical displacement. Its signature in the seismic section looks similar to the channel signature (wide V shape) highlighted by yellow ellipse in Figure 2.25. The normal fault and strike slip fault have a small trough and they are difficult to interpret and track throughout the volumes (Figure 2.25). Their interpretations were enhanced by later seismic attributes analysis including curvature analyses, which are discussed in Chapter Three.

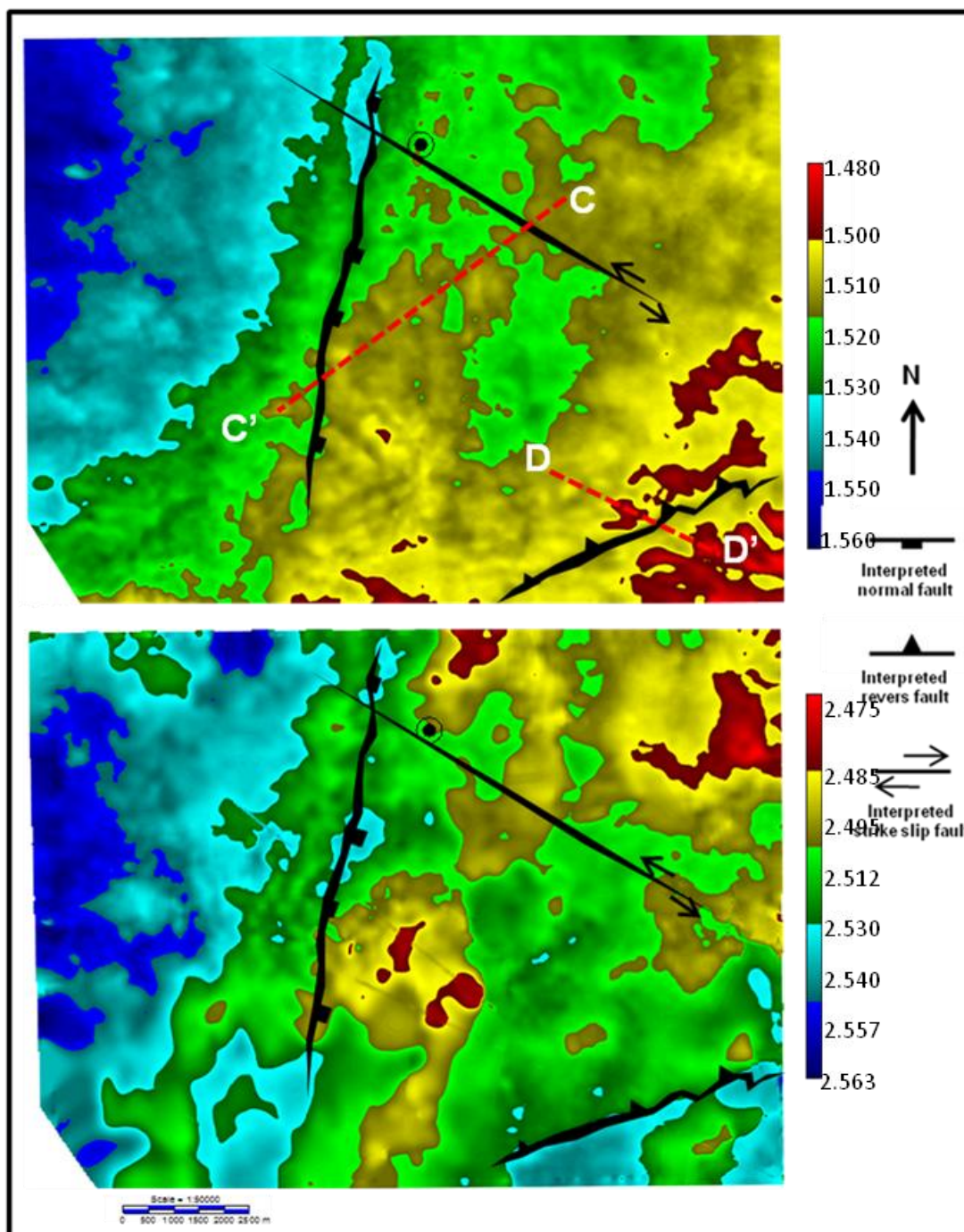


Figure 2.24: Base Muskwa shale PP time structure map (upper) and PS time structure map (lower) showing the interpreted faults (black solid lines) that cut this surface in the area and the location of the two cross sections C-C' and D-D'.

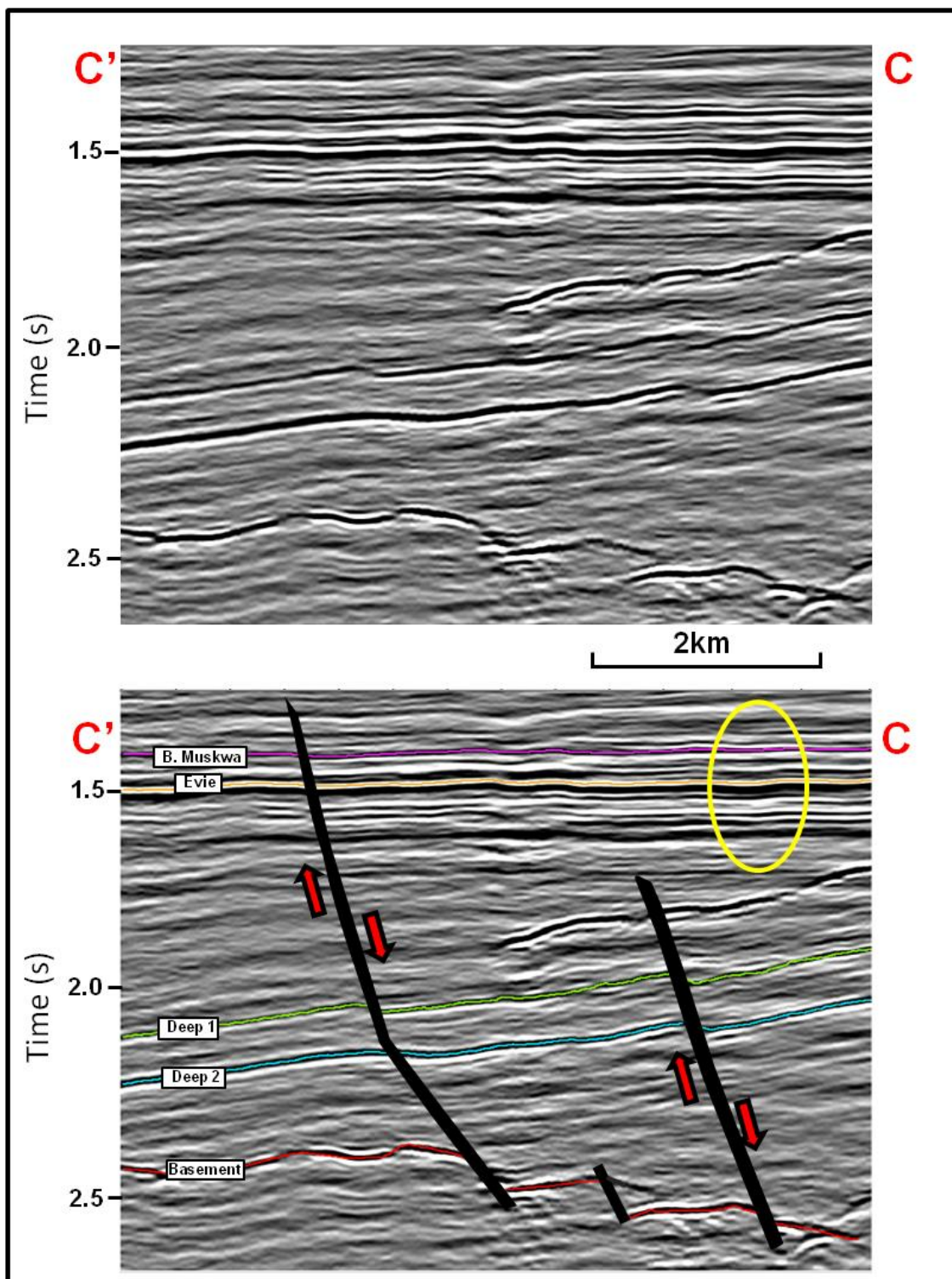


Figure 2.25: C-C' traverse through PP section, shows the strike slip fault (yellow ellipse) and the normal faults (black solid lines) that cut the deep horizons including Muskwa shale. Refer to Figure 2.24 for the location of the cross section.

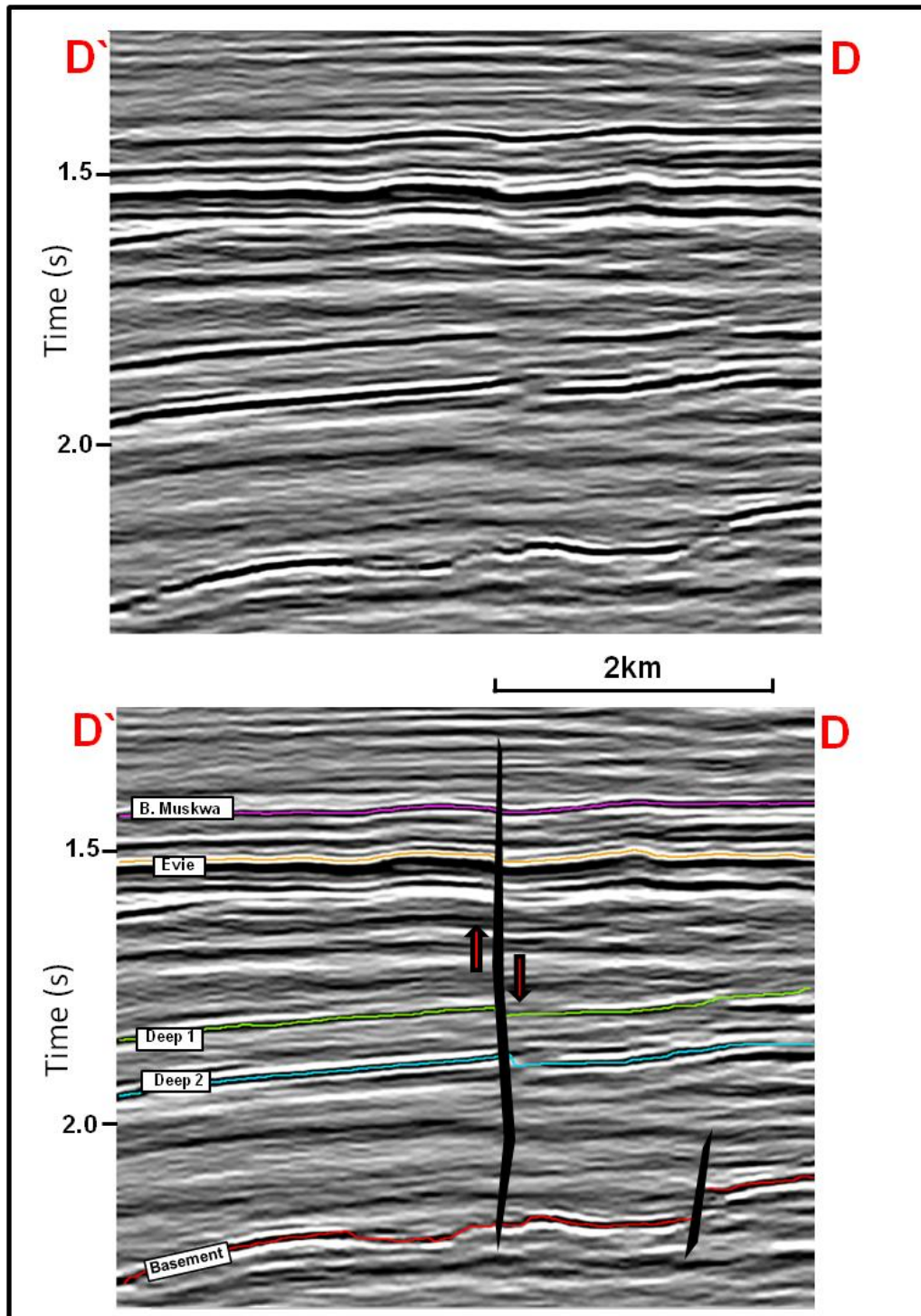


Figure 2.26: D-D' traverse through PP section (above) and PS section (below), shows the reverse fault indicated by black solid lines that cut the deep horizons including Muskwa shale. Refer to Figure 2.24 for the location of the cross section.

## 2.7 Summary

The gross structural interpretation of the 3D multicomponent seismic dataset from the Horn River Basin highlights different major fault trends. At the top of the Exshaw Formation (Upper Devonian and Lower Mississippian), four normal faults have been recognized and mapped. They dip southwest and their strike direction is trending northwest-southeast. The magnitude of the throw of these faults decreases with depth and they do not cut the deep horizons such the Muskwa and the Evie Formations. This implies that these faults must be connected to a major detachment between the Exshaw and Muskwa Formations.

At the Muskwa Formation (Middle Devonian), three major fault trends have been identified and have different features and trends compared to the faults mapped at the shallower formations. These deeper faults include one reverse fault trending southwest-northeast, one normal fault trending north-south, and one strike slip fault trending northwest-southeast. The reverse fault has formed a small four way anticline closure and its axis is parallel to the strike direction of the fault. The normal faults and the strike slip fault have small vertical displacements and they are difficult to interpret on the seismic sections.

All the faults are generally better imaged on the PP sections than the PS sections and required enhancement by the use of seismic attributes analysis such as curvature analyses, as discussed in the following chapter.

## **CHAPTER 3: 3D CURVATURE ANALYSIS AND VP/VS INTERVAL MAPPING**

### **3.1 Introduction**

Seismic attributes are described by Sheriff (2006), as the measurements that are obtained from seismic traces in the form of time, velocity, amplitude, frequency and attenuation. In general, seismic time attributes are used to enhance structural interpretations and the seismic amplitude, velocity and frequency attributes are considered to improve the stratigraphical interpretations as well as to delineate best reservoir-quality hydrocarbon-bearing rocks (Marfurt, 2008).

In this chapter, the use of 3D curvature analysis to enhance fault interpretations for both shale reservoirs in the study area (Exshaw, and Muskwa) and its integration with other attributes such as instantaneous frequency, amplitude extractions and Vp/Vs interval extraction are discussed.

### **3.2 Theory**

Recently, curvature has been used to recognize subsurface geological features such as faults/fractures and channels (e.g Chopra et al., 2006). Curvature describes how bent a surface is at a particular point and it is closely related to the second derivative of a curve defining the surface (Roberts, 2001). In a 2-D curve, it is the reciprocal of the radius of a circle that is tangent to the curve at any point on it and curvature will be larger for a curve that is tightly folded and will be zero for straight line or dipping plane (Figure 3.1a) (Roberts, 2001). The sign convention for curvature attributes that is proposed by Roberts (2001) is shown in Figure 3.1a. The arrangement of vectors (black arrows), which are normal to the surface indicates the sign of curvature or where the curve bends are facing. For example, planar and dipping surfaces have zero curvature, anticlines have

positive curvature and synclines have negative curvature. In 3-D, the curvature analysis can be computed by applying the same curvature from a 2D analysis for the intersections of two orthogonal planes with the 3D surface (Figure 3.1b) (Chopra and Marfurt, 2007).

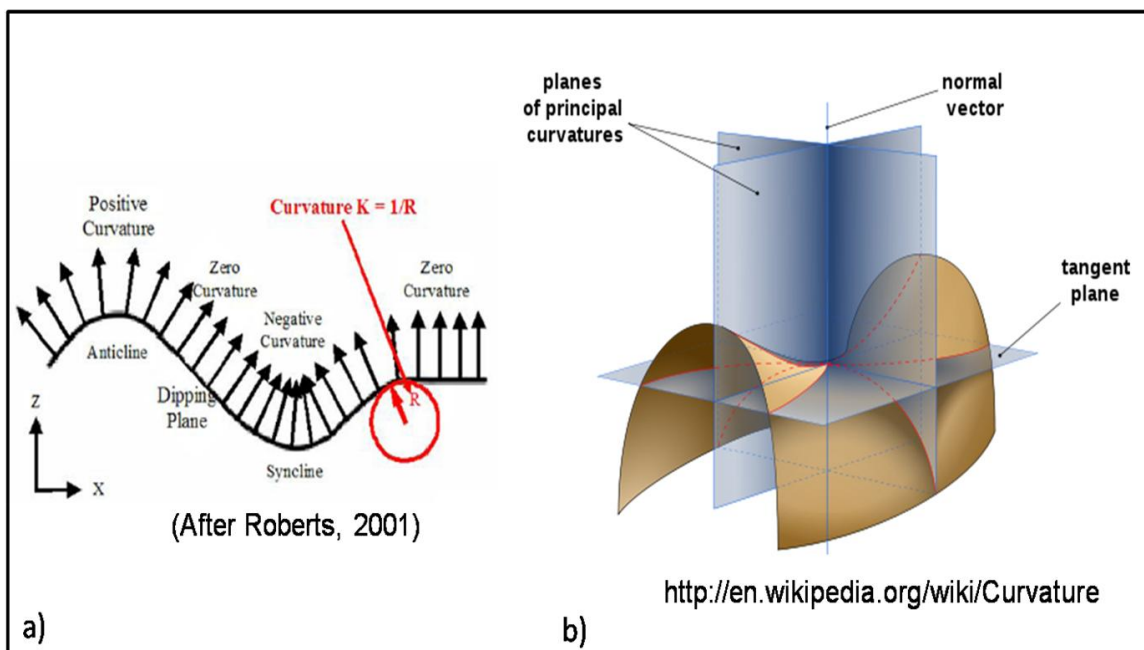


**Figure 3.1:** (a) illustrates a 2D curvature of a line and the sign convention for curvature attributes. The arrows represent vectors, that are normal to the surface. When vectors are parallel on flat or planar dipping surfaces, the curvature is zero. When vectors diverge over anticlines, the curvature is defined as positive and every time they converge over synclines, the curvature is defined as negative. (b) Showing the two orthogonal set that intersect with the 3D surface.

The curvature computation can be obtained through:

- 1-horizon based analysis
- 2-volumetric based analysis

Horizon-based curvature computations require high quality seismic data and a strong impedance contrast at the horizon of interest, whereas volume-based curvature does not need a picked horizon to undertake the analysis (Chopra and Marfurt, 2007). Al-Dossary and Marfurt (2006), introduced the volumetric computation of curvature, which abandons

the need for picked horizon to do the curvature analysis. This volumetric computation can be summarized into two important steps; step one is to estimate the volumetric reflector dip and azimuth that represents the single dip for each sample in the dataset by equation (3-1) (Al-Dossary and Marfurt, 2006):

$$F_{\alpha}(\partial u/\partial x) = (-ik_x)^{\alpha} F(u), \quad (3-1)$$

where the operator  $F$  denotes the Fourier transform, where  $u$  is an inline or crossline component of reflector dip, and where  $\alpha$  is a fractional real number that typically range between 0 and 1. Step two is to compute the curvature from the adjacent measures of dip and azimuth (Al-Dossary and Marfurt, 2006). Finally, a full 3D volume of curvature values is formed that we can slice and visualize through a picked horizon or a specific reflection time. Since the volume-based curvature is computed from a time window of seismic data, the results are statistically less sensitive to backscattered noise and have a higher signal-to-noise ratio than horizon-based curvature (Chopra and Marfurt, 2007). In actual practice, there are many curvature measures that can be computed by fitting mathematical quadratic surfaces to the surface areas. These are minimum, maximum, most-positive, most-negative, curvedness, azimuth of minimum curvature, shape index, dip and strike curvature (Roberts, 2001). The most-positive and the most-negative curvature measures are found to be the most useful for representing the geological structure interpretations (Chopra and Marfurt, 2007).

### 3.3 Curvature analysis and results

Curvature analyses were calculated on the 3C-3D data and the results are shown in Figures 3.2, through 3.5. Figure 3.2a shows the horizon-based most negative curvature for the top of the Exshaw horizon for the PP volume, and shows (a) four normal faults,

indicated by the blue arrows; (b) artifacts generated by a significant channel system within the near surface, indicated by the white arrows and (c) interpreted acquisition footprint throughout the survey area, highlighted, for example, in the red ellipses. Figure 3.2b shows the 0.894 second time slice of the volume-based most negative curvature computed on the PP volume, and shows the same four normal faults as in Figure 3.2a indicated by blue arrows, as well as the artifacts generated by a shallow channel system, indicated by white arrows. Figure 3.3a shows the 1.208 second (Exshaw Formation) volume-based most negative curvature computed on the PS volume, showing the four normal faults indicated by blue arrows. It also shows two obvious features that are believed to be artifacts generated by the significant channel system within the near surface, indicated by white arrows. These subsurface channels are shown in refraction bedrock map (Figure 3.3b), which was provided by Olympic Seismic.

Figures 3.4a and 3.4b show the 0.820 second (Exshaw Formation) volume-based most negative curvature and the 0.820 second volume-based most positive curvature on PP volume, respectively. Both maps highlighted the lateral continuity of the faults clearly which indicated by red arrows; however the fault locations are spatially displaced on both maps indicated by red circle and the right location of the fault should be the space in between, as shown by the yellow line for one of the faults.

Figure 3.5a shows the computed horizon-based most negative curvature on the PP volume for the base of the Muskwa horizon and shows the three major faults at this level, indicated by the black arrows. The computed volume-based most negative curvature at the level of the base Muskwa shale, represented by the 1.52 second time slice, is shown

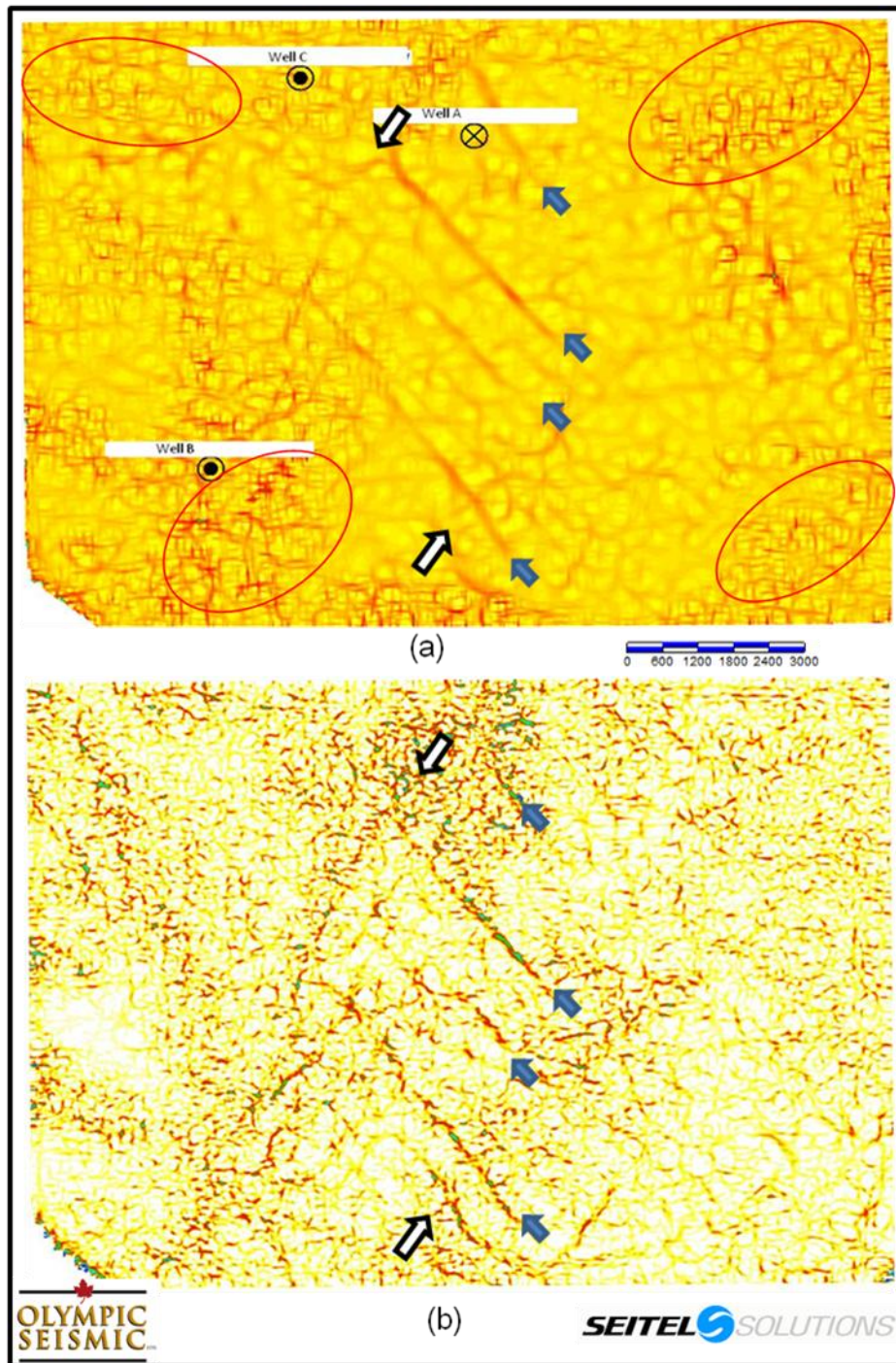


Figure 3.2: (a) Horizon-based most negative curvature for the top of Exshaw horizon (b) 0.894 second time slice of the volume-based most negative curvature computed on PP volume. Red ellipses indicate acquisition footprint. The blue arrows show the four normal faults and the white arrows show the two possible strike-slip faults.

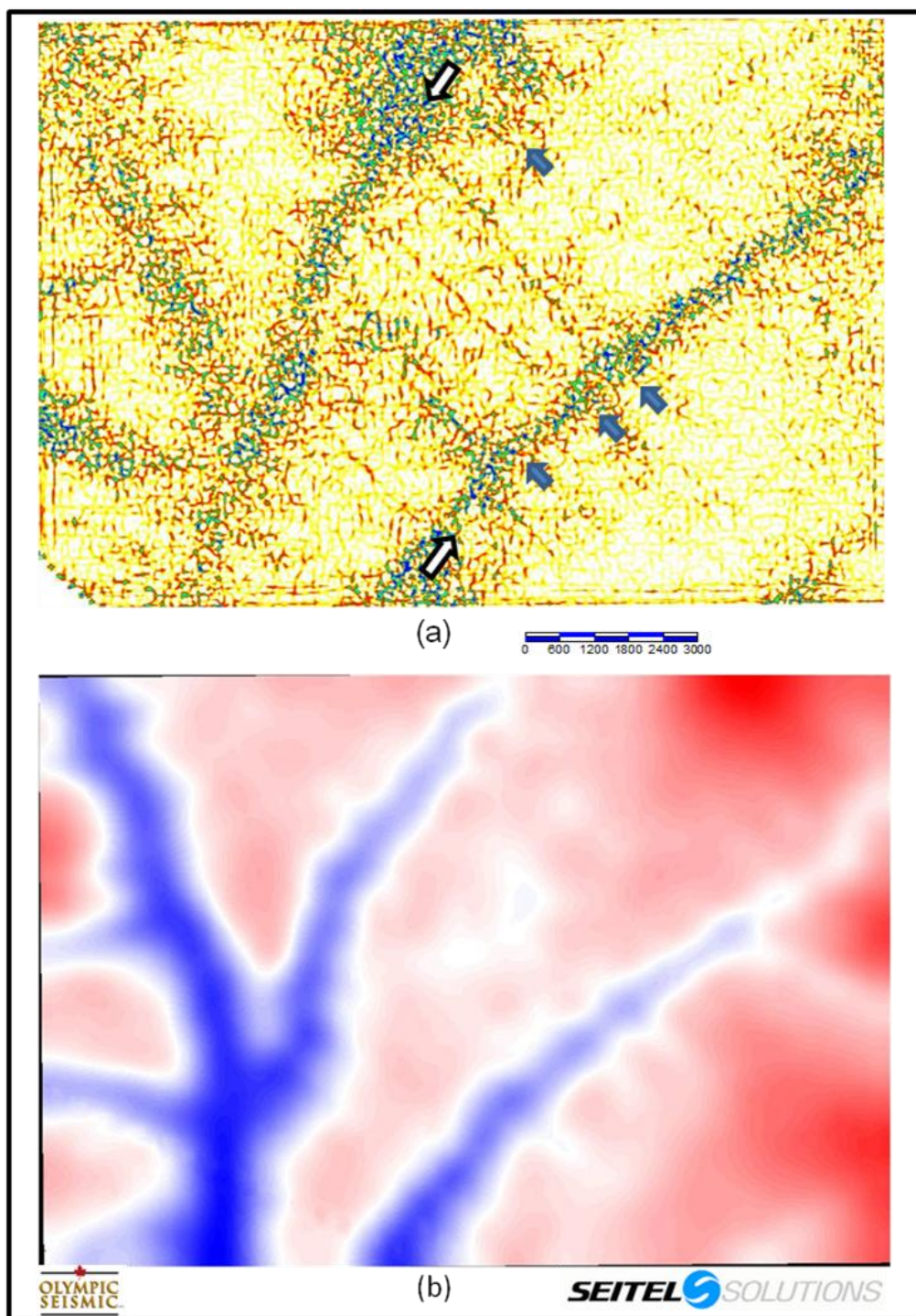


Figure 3.3: (a) 1,208 second volume-based most negative curvature computed on PS volume (b) base of weathering layer map.

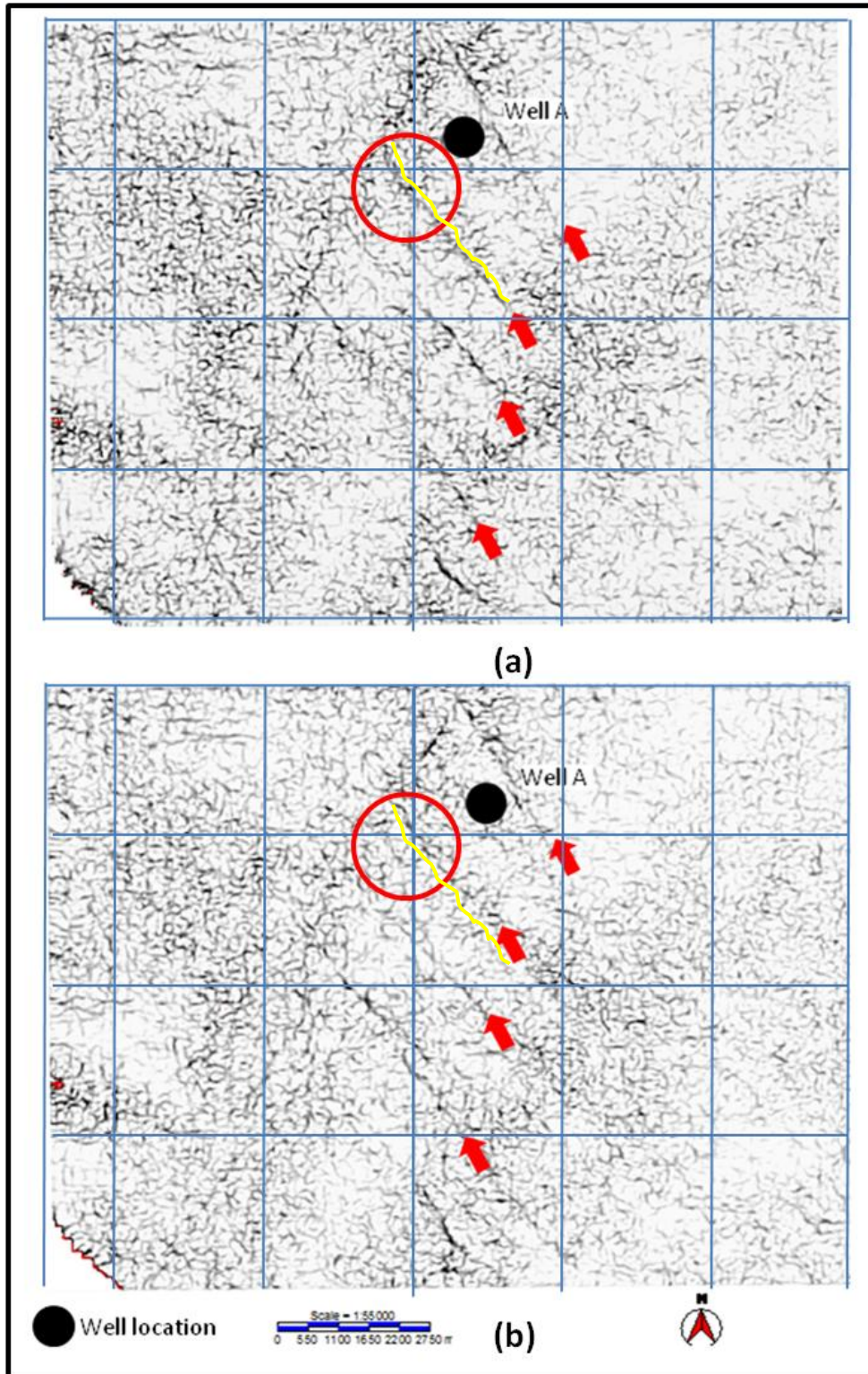


Figure 3.4: (a) 0.820 second volume-based most negative curvature computed on PP Volume (b) 0.820 second volume-based most positive curvature computed on PP Volume.

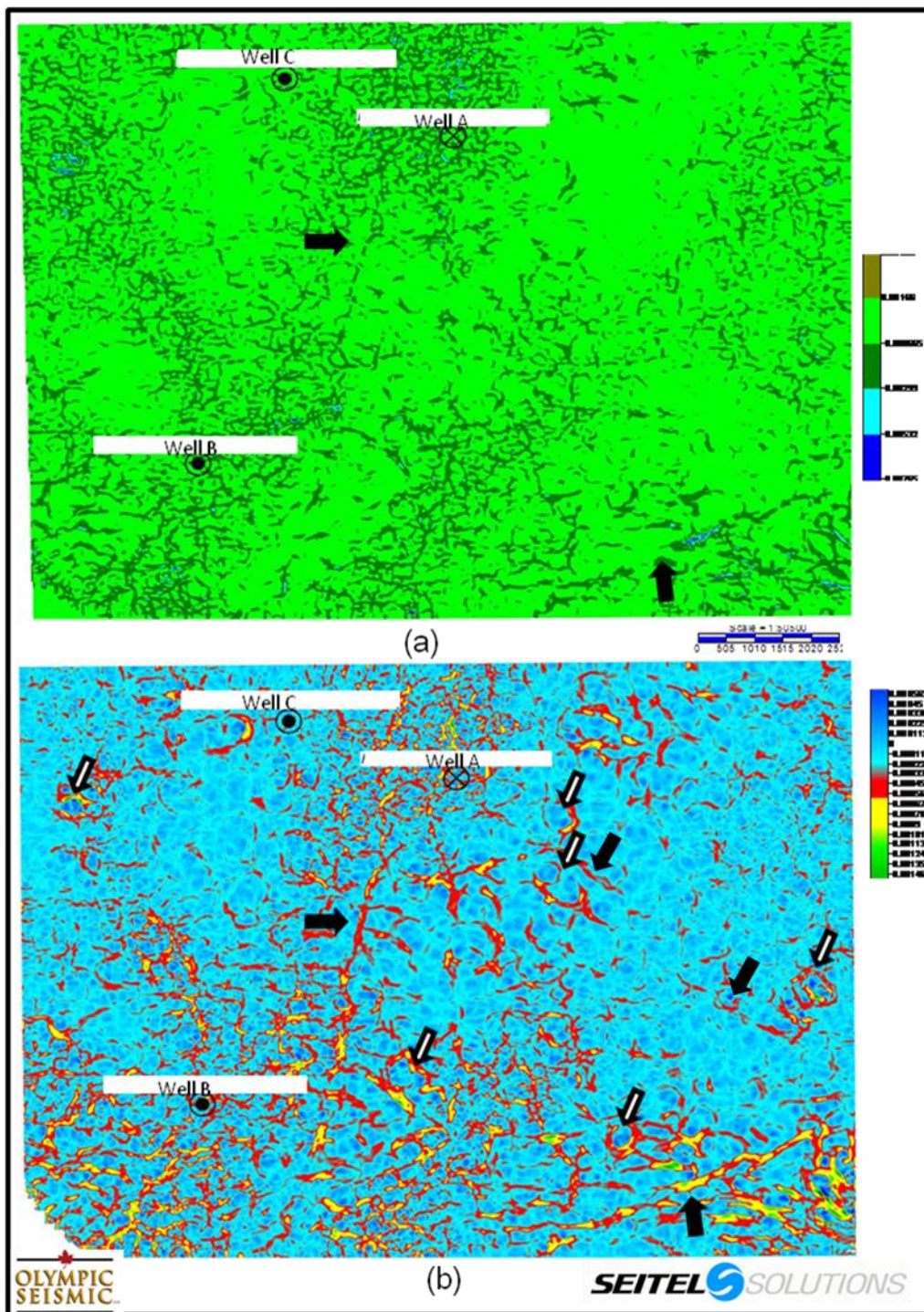


Figure 3.5: (a) Horizon-based most negative curvature on the PP volume for the base of Muskwa horizon (b) 1.52 second time slice of the volume-based most negative curvature computed on PP volume. The black arrows indicate the two major faults and the white arrows show circular features which are interpreted to be possible mounds or karsting features.

in Figure 3.5b. It shows clearly the three major faults cutting this section, indicated by black arrows, and circular features which are interpreted to be mounds or karst features, indicated by white arrows. These features were not mapped by the horizon-based attribute (Figure 3.5a).

### **3.4 3D visualization**

As stated by Lynch (2008), seismic resolution has been divided into two types, namely absolute and apparent resolution. Absolute resolution is the actual temporal and spatial resolution of the data, whereas the apparent resolution is achieved by enhanced visualization by looking at the data at different angles, views and colors. Figure 3.5, shows a horizon slice (PP data) at the base of Muskwa shale extracted from most negative curvature volume from different orientations and angles. The color bar indicates dark blue for the most negative curvature and red for positive curvature values. Figure 3.5a is a top view and the strike-slip fault is highlighted by red arrows. This fault is more pronounced when we view this picture from the southeast direction, in the same direction as the fault strike (Figure 3.6b). An even better angle and view for the strike-slip fault is shown in Figure 3.6c. In this orientation, the fault appears to extend to the southeast along a different segment, indicated by red arrows. Figure 3.6d is a 3D zoomed view of the white rectangle area shown in Figure 3.6a. It clearly shows a mound shape developed in this area, indicated by the white arrow. This is not the only mound developed in this level however, Figure 3.5b shows other possible mound locations. Another example of enhanced apparent resolution by looking at the data from different perspective is shown in Figure 3.7, from the PS data volume. In this Figure the four normal faults are well mapped in all orientations (Figure 3.7a, Figure 3.7b, and Figure 3.7c). However Figure

3.7c shows a conjugate faults trend to the normal faults when we use the lighting to visualize the results. The normal fault trend is shown by green arrows whereas the conjugate trend is identified by red arrows (Figure 3.7c).

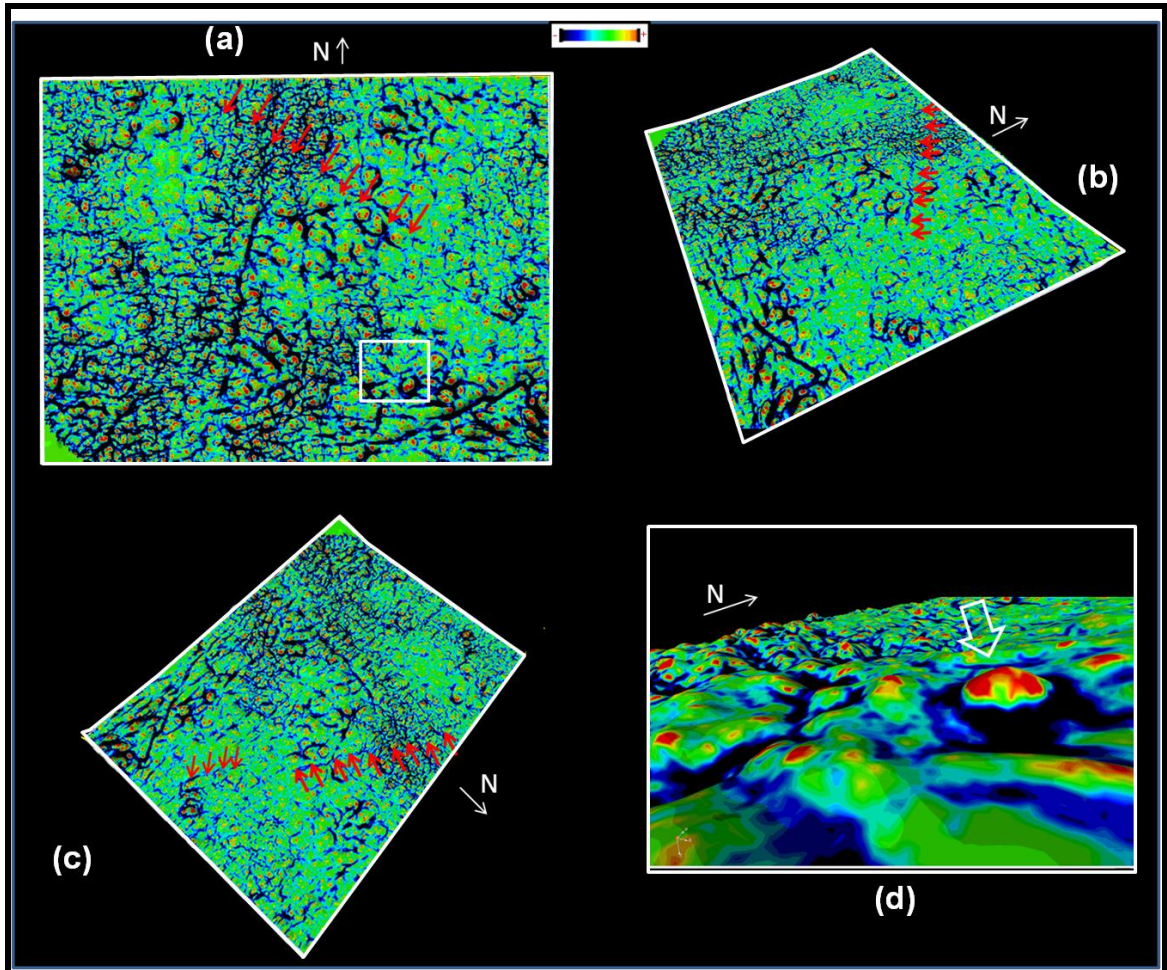


**Figure 3.6: Horizon-slice through most negative curvature volume at the base of the Muskwa shale horizon. The color bar indicates dark blue for most negative curvature value and red for positive curvature value. (a) Top view (b) the same horizon slice but looking at it from the southeast corner (c) top view from the northeast corner (d) zoomed 3D view showing the mound feature. The strike slip fault is indicated by red arrows.**

### 3.5 Fracture interpretation

Fracture detection using seismic amplitude data is very challenging due to seismic data being band-limited which reduces seismic resolution. However, despite the fact that fractures are a sub-seismic geological features, curvature, particularly the computed volume-based most negative curvature, is a useful attribute for making predictions regarding fracture density (Hunt et al., 2010). Fracture detection using curvature analysis is based on three hypotheses: the rock is brittle and breaks due to fracturing, an increase in curvature implies an increase in strain, and an increase in strain implies an increase in fracture density (Nelson, 2001).

The interpreted fractures using curvature analysis, is characterized by a relatively medium to high negative curvature value (dark to light blue color). In this case study, zones of natural fractures are detected mainly close to the major faults (Figure 3.8). The dominant trends of these fractures (red circles) are generally parallel to the major faults in the area (Figures 3.8a, and 3.8b). The unique advantage of the curvature attribute when it is compared to other seismic methods for detecting natural fractures such as AVAZ (Amplitude varying with azimuth) is that its results give a direct interpretation of geology (Hunt et al., 2010). Figures 3.6a, 3.8b, 3.8c illustrate that the curvature attribute shows some well developed mound features (black arrows), and possibly small faults and joints (white arrows) and fractures (red circles).

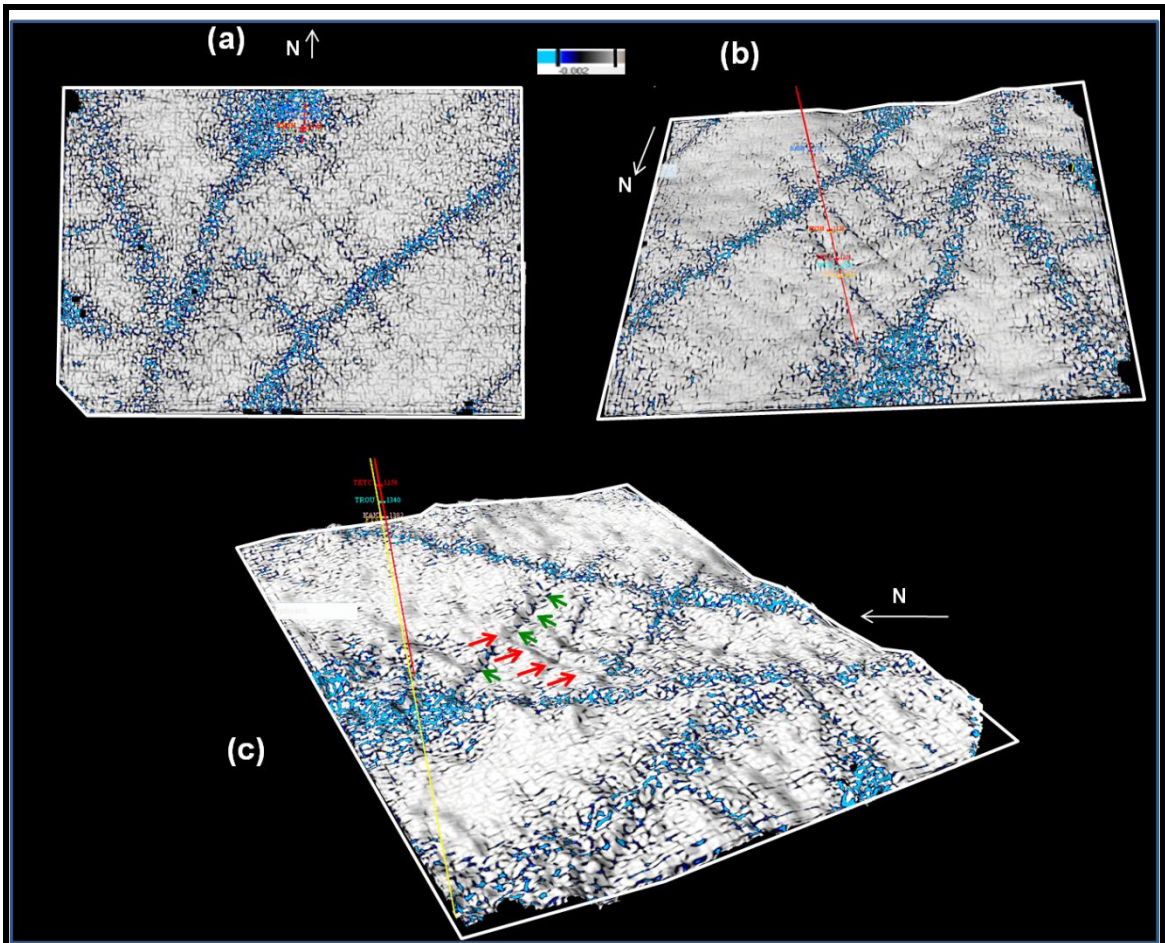


**Figure 3.7: Horizon-slice extracted from most negative curvature PS volume at the top of the Exshaw shale horizon. The color bar indicates blue and black colors for most negative curvature value and white color for positive curvature value. (a) top view looking north (b) the same horizon slice but looking south with angle to show the 3D view (c) top view from the northwest corner and with using light to indicate the four normal faults (green arrows) intercepting possible other faults (red arrows) orthogonally. The artifacts generated by a significant channel system within the near surface are indicated by negative curvature values shown by the blue color.**

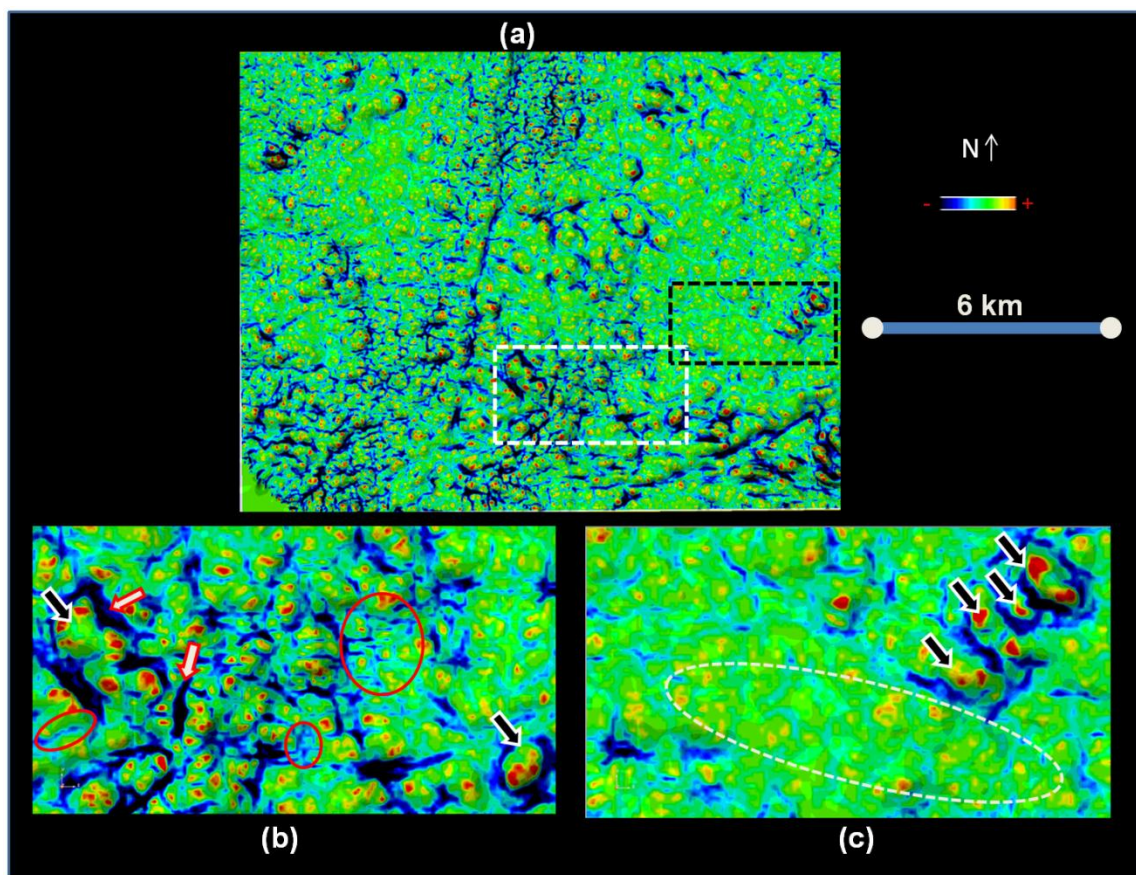


**Figure 3.8: Horizon-slice through most negative curvature PP volume at the base of the Muskwa shale horizon; the color bar indicates dark blue for most negative curvature value and red for positive curvature value. (a) Top view for the whole surface (b) Zoomed view of high fractured density area. The location of this area is shown in white dashed rectangular in the above figure. (c) Zoomed view of low fractured density area indicated by curvature. The location of this area is shown in black dashed rectangular in the above figure.**

### 3.6 Interval $V_p/V_s$ analysis, amplitude, and instantaneous frequency

The change of  $V_p/V_s$  within a reservoir can be attributed to many variations of its properties. It could be due to the variation of lithology (shale content) (Stewart et al., 2003), porosity (Close et al., 2010), water saturation (Xu, 2006), or presence of a natural fracture network (Zhang, 2010). The dominant driving effect for all of these is the shale content. Therefore, interval  $V_p/V_s$  maps of both the top of the Exshaw and the base of the

Muskwa Formations were used in an attempt to map fractures in the formations and to predict higher porosity reservoir. The  $V_p/V_s$  maps for these two targets were extracted using the isochron maps from both PP and PS data for the same depth interval according to the formula (Margrave et al., 1998)

$$\frac{V_p}{V_s} = \frac{2\Delta t_{ps} - \Delta t_{pp}}{\Delta t_{pp}} \quad (3-2)$$

Where  $\Delta t_{ps}$ , and  $\Delta t_{pp}$  are the PS and PP travel times for the target interval.

Seismic amplitude is defined as a physical measurement of the targeted subsurface reflection or horizon and it is a function of  $\rho$  (density),  $V_p$  (compressional velocity) and  $V_s$  (shear velocity) (Vetrici and Stewart, 1996). Whereas, the instantaneous frequency is the first derivative of the instantaneous phase, and is given by:

$$\omega(t) = d\theta(t) / dt$$

and it shows how the instantaneous phase of the seismic trace changes quickly with time (Vetrici and Stewart, 1996). Both amplitude and instantaneous frequency maps have been used to predict fractures. For example, Figure 3.8 shows an example of using these attributes to predict fractures within a tight sand reservoir in the Powder River Basin, United States (Mavko, 2010). Low amplitude and low instantaneous frequency values (blue color in Figure 3.9) were used to indicate fractured areas within the reservoir due the loose of spectral of energy of the P-wave near the Fresnel zone (Mavko, 2010).

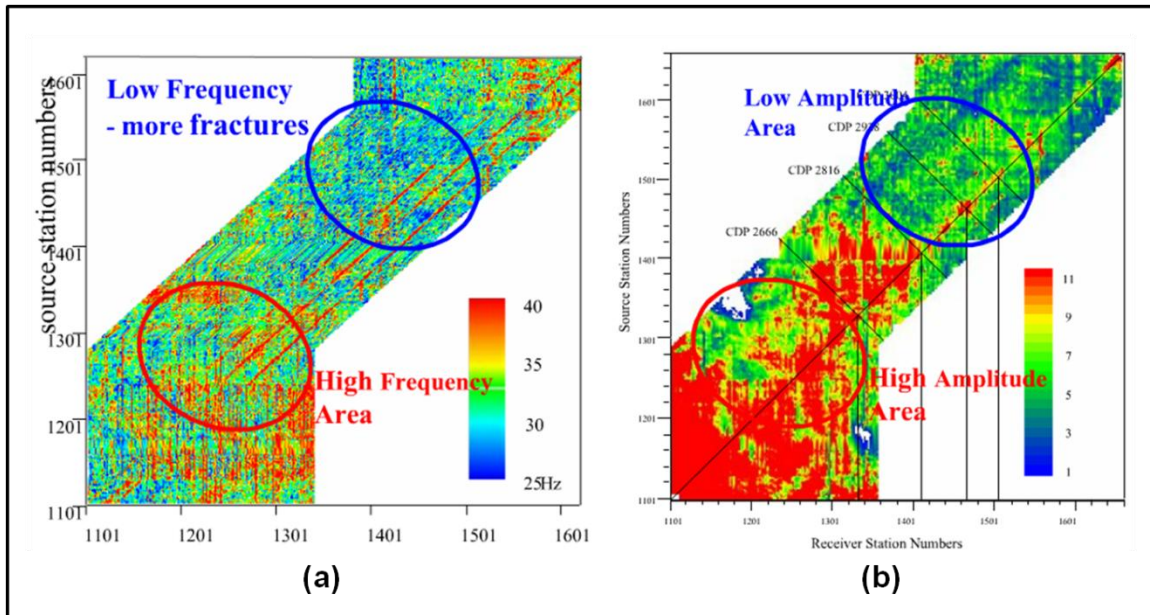


**Figure 3.9: Example from Powder River Basin showing the fracture signature using amplitude and instantaneous frequency seismic attributes. (a) Instantaneous frequency map shows that the fractures are present in low frequency area, indicated by blue color. (b) Amplitude map values shows fractured area are characterized by low amplitude values highlighted by blue and green colors (from Mavko, 2010).**

### 3.7 Results for Exshaw Formation

For the Exshaw Formation, two intervals were chosen for interval  $V_p/V_s$  analysis using equation (3-1): the first is from the Banff Formation to the Tetcho Formation, and the second interval is from the Banff Formation to the Fort Simpson Formation (Figure 3.10). These intervals were chosen because reflections from these formations could be registered on both PP and PS volumes with confidence. By comparing the  $V_p/V_s$

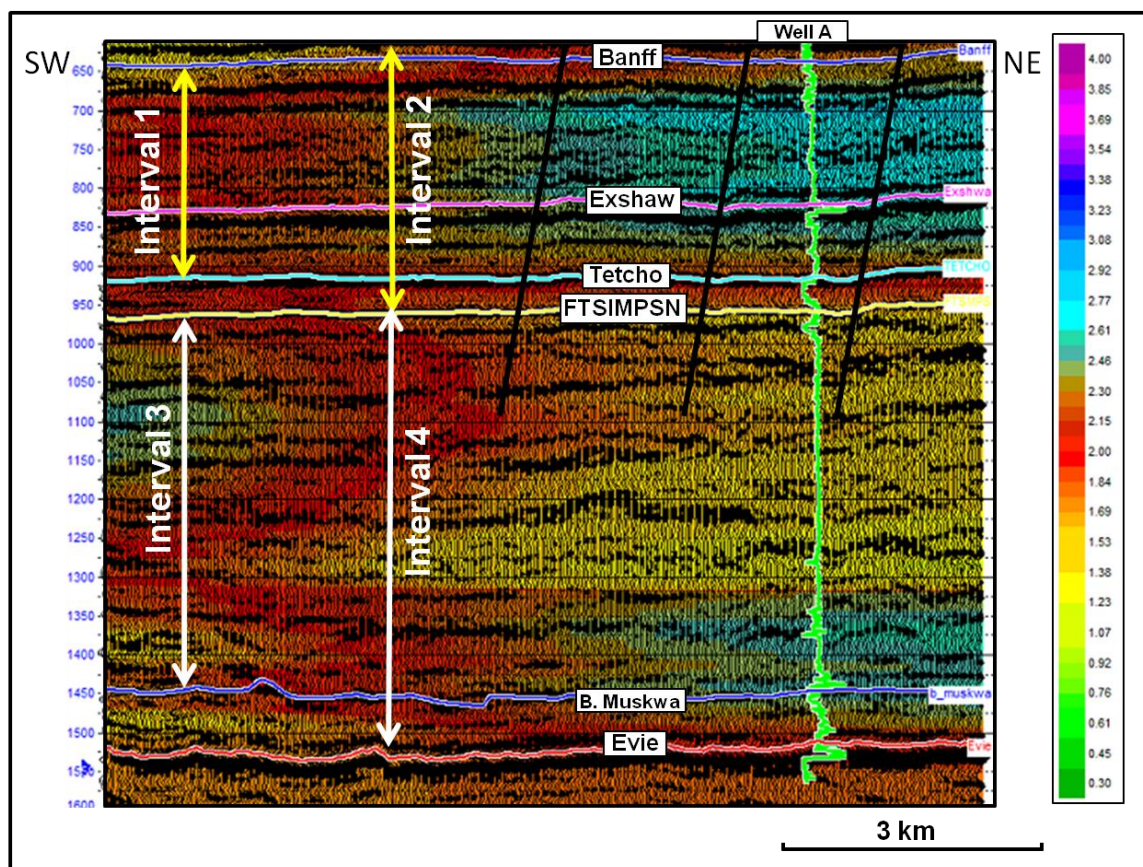


**Figure 3.10: SW-NE seismic line showing the intervals used for interval  $V_p/V_s$  calculation. Interval 1 is from the Banff Formation to the Tetcho Formation; interval 2 is from the Banff Formation to the Fort Simpson Formation; interval 3 is from the Fort Simpson Formation to the Base of Muskwa Formation ; interval 4 is from the Fort Simpson Formation to the Evie Formation.  $V_p/V_s$  extrapolated from well values superimposed on the seismic sections. Refer to Figure 3.10 for the location of the line. Black solid lines indicate interpreted faults.**

maps of these two intervals, the relative  $V_p/V_s$  trend relevant to the Exshaw Formation was estimated. Figures 3.11a and 3.11b show the interval  $V_p/V_s$  map from the top of Banff Formation to the top of Tetcho Formation and interval  $V_p/V_s$  map from the top of Banff Formation to the top of Fort Simpson Formation. The dashed white ellipses show

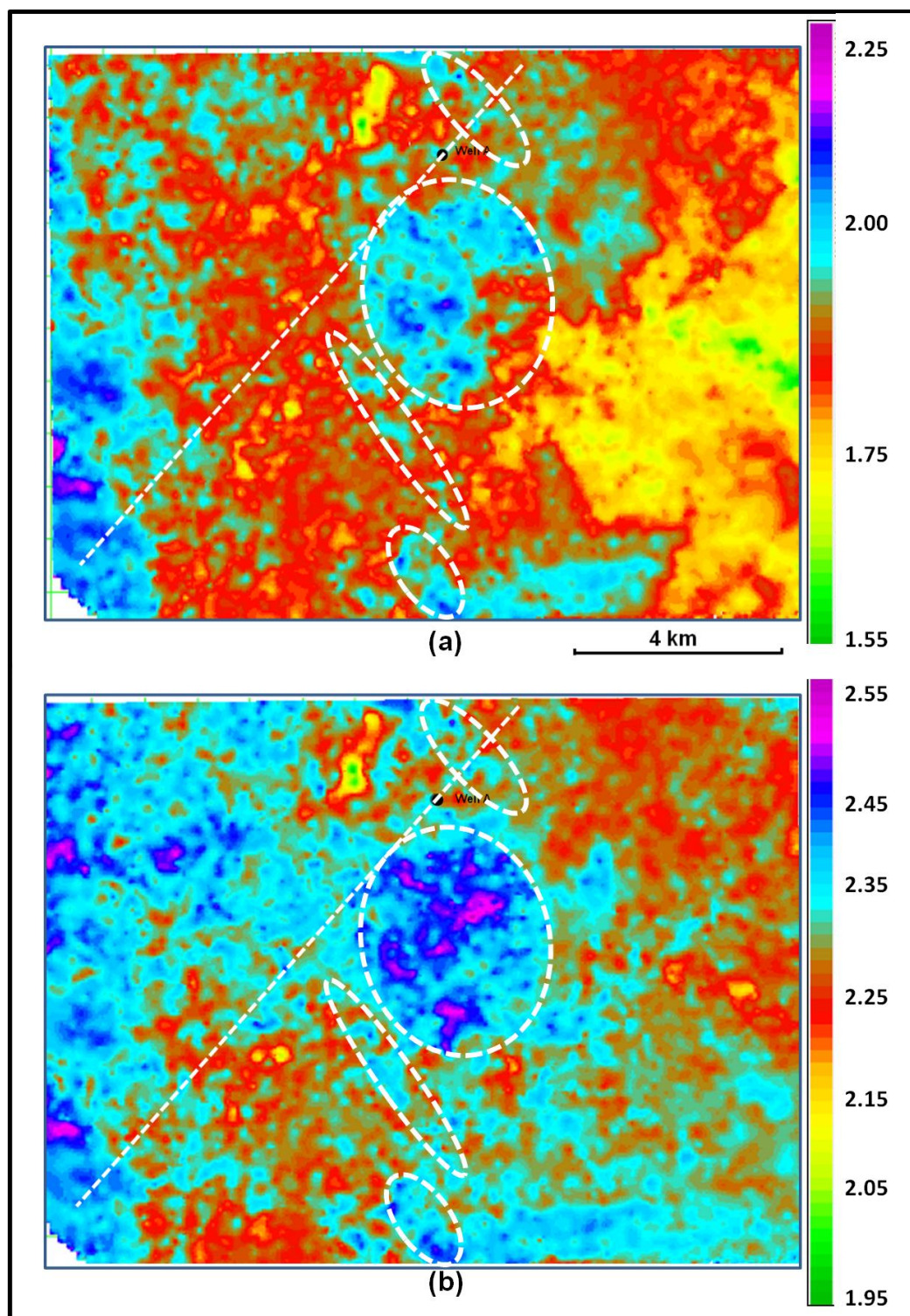


**Figure 3.11: (a) Interval  $V_p/V_s$  map from the Banff Formation to the Tetcho Formation. (b) Interval  $V_p/V_s$  map from the Banff Formation to the Fort Simpson Formation. Dashed white line indicates the location of the seismic line shown in Figure 3.9. Dashed white ellipses show high  $V_p/V_s$  trends.**

the areas with higher  $V_p/V_s$  values (purple and blue colors) in both maps. These areas are clustered near the four normal faults zones and can be possibly interpreted to indicate fault related fractures. These interpretations can be supported by looking at the amplitude and instantaneous frequency maps extracted at the top of Exshaw shale Formation (Figures 3.12a and 3.12b). The black ellipses in the instantaneous frequency map (Figure 3.12a), highlight low instantaneous frequency areas (red to green color) that correlate with low amplitude values (blue colors) in the amplitude map (Figure 3.12b), also indicated by the black ellipses. The integration of extracted curvature maps with the extracted  $V_p/V_s$  maps yield a better structural interpretation conclusion (Figure 3.13). Ultimately, the curvature attributes show the major fault trends (Figure 3.13a) and higher  $V_p/V_s$  interval values (Figures 3.11a, 3.11b and 3.13b) highlight potentially highly fractured areas within the Exshaw shale reservoir, reasonably induced by the major faults (Figure 3.13a).

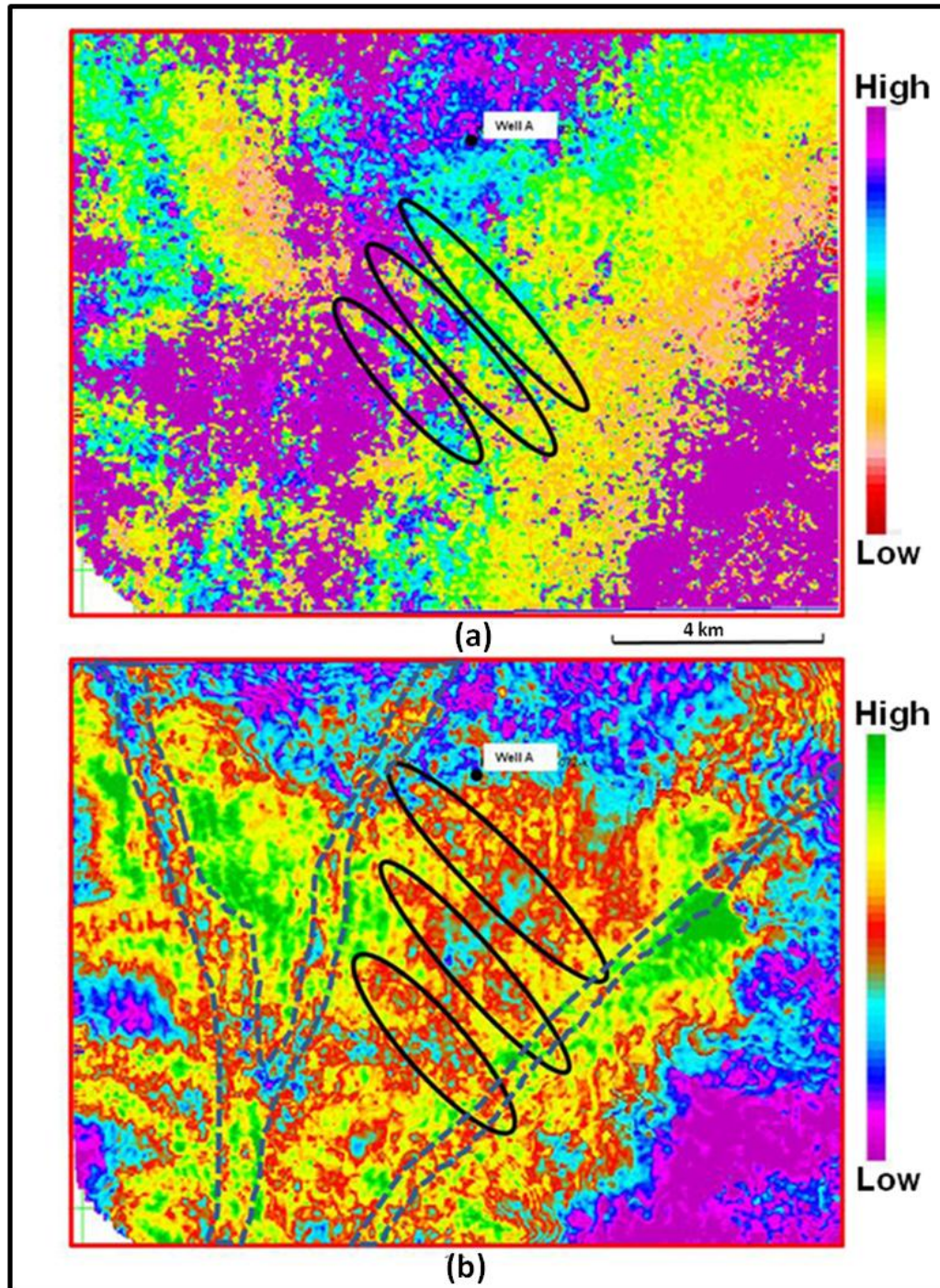
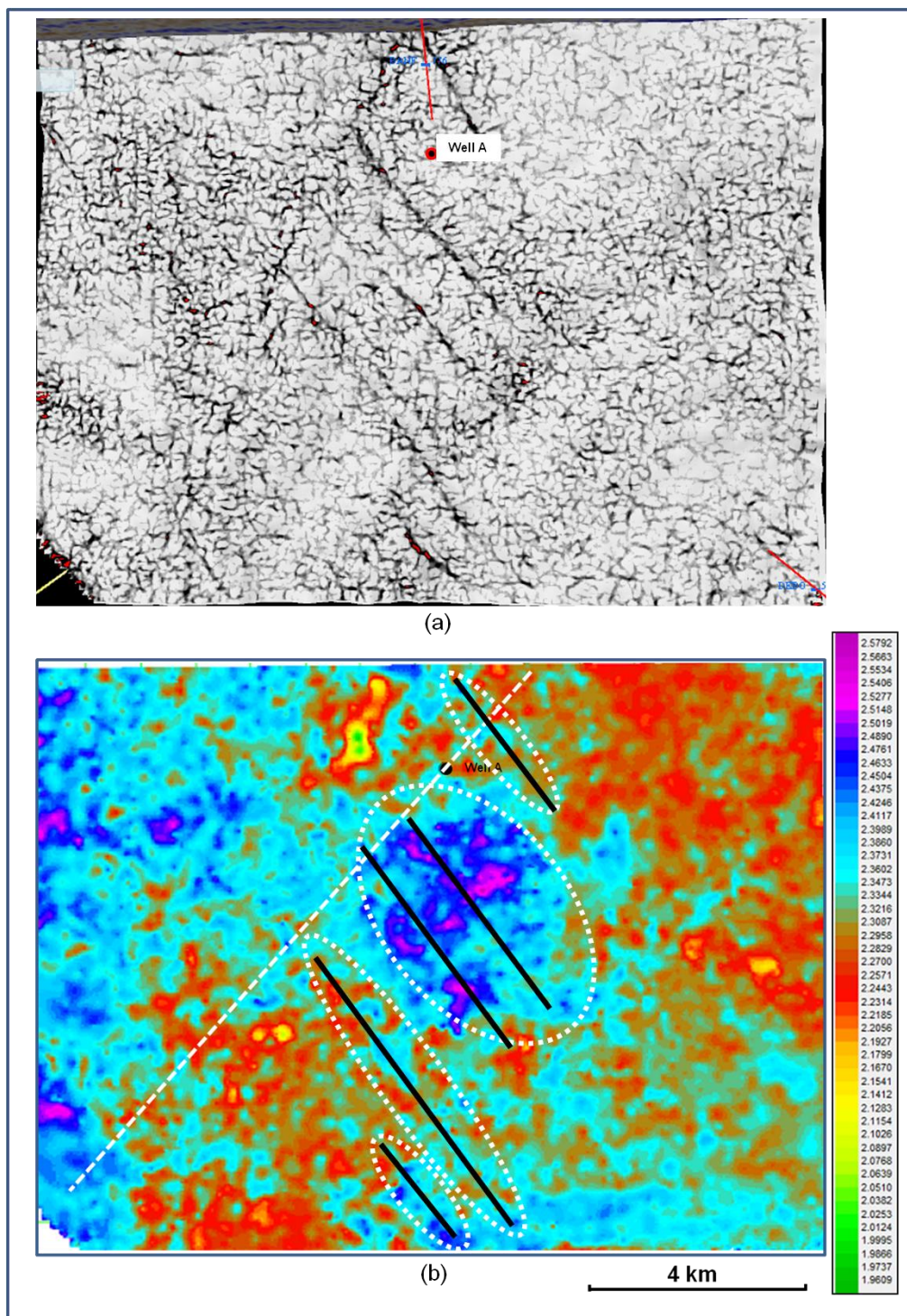


Figure 3.12: (a) Instantaneous frequency map extracted with a 30 ms window centered at the top of Exshaw seismic horizon. (b) Amplitude map extracted at 30 ms window centered at top of the Exshaw seismic horizon. Black ellipses highlight low values of both maps that correlate with high  $V_p/V_s$  areas shown in Figure 3.10. Dashed blue polygons indicate artifacts generated by the channel system within the near surface.



**Figure 3.13: (a) Horizon-slice through most negative curvature volume at the top of the Exshaw shale horizon. Black indicates negative curvature values. (b) Interval  $V_p/V_s$  map from the Banff Formation to the Fort Simpson Formation. Blue color indicate higher  $V_p/V_s$  values and black solid lines indicate interpreted faults that have been mapped using curvature at this level.**

### 3.8 Result for the base of Muskwa shale reservoir

Similarly, Vp/Vs analysis was undertaken for the interval from the Fort Simpson Formation to the base of the Muskwa Formation (Figure 3.14a) that is identified by interval 3 in Figure 3.10, and interval from the Fort Simpson Formation to the Evie Formation (Figure 3.14b) that is identified by interval 4 (Figure 3.10). These intervals were used to calculate the Vp/Vs changes at the base of Muskwa shale using equation (3-1). The Vp/Vs values seem to be too large (Vp/Vs for shale is 2.1), but this could be attributed to the larger picking errors of the base of the Muskwa Formation and the top of Evie Formation on the PS data due to the low dominant frequency. Higher Vp/Vs trends that correlate with faults vicinity (black solid lines) have been mapped at this level (Figures 3.14a and 3.14b). In addition, the extracted 30 ms window RMS amplitude at the same horizon (Figure 3.15b) showed that these high Vp/Vs areas correlate with low amplitude (light blue color). Also, the faults zones which correlate with high Vp/Vs values are characterized by low frequency content in the instantaneous frequency map (Figure 3.15b). Figure 3.16a shows the extracted most negative curvature at the base of Muskwa shale horizon. Blue color indicated most negative curvature values (faults and fracture areas) and it is well correlated with high Vp/Vs values, also indicated by the blue color (Figure 3.16b). Note that the mound features that are highlighted by dashed white circles in the curvature map (Figure 3.16a) have high Vp/Vs values indicated by dashed black circles (Figure 3.16b). In summary, the curvature attributes are interpreted to show the major fault and fractured areas that are characterized by negative values (Figure 3.16a). These negative curvature values correlate with high Vp/Vs interval values (Figure

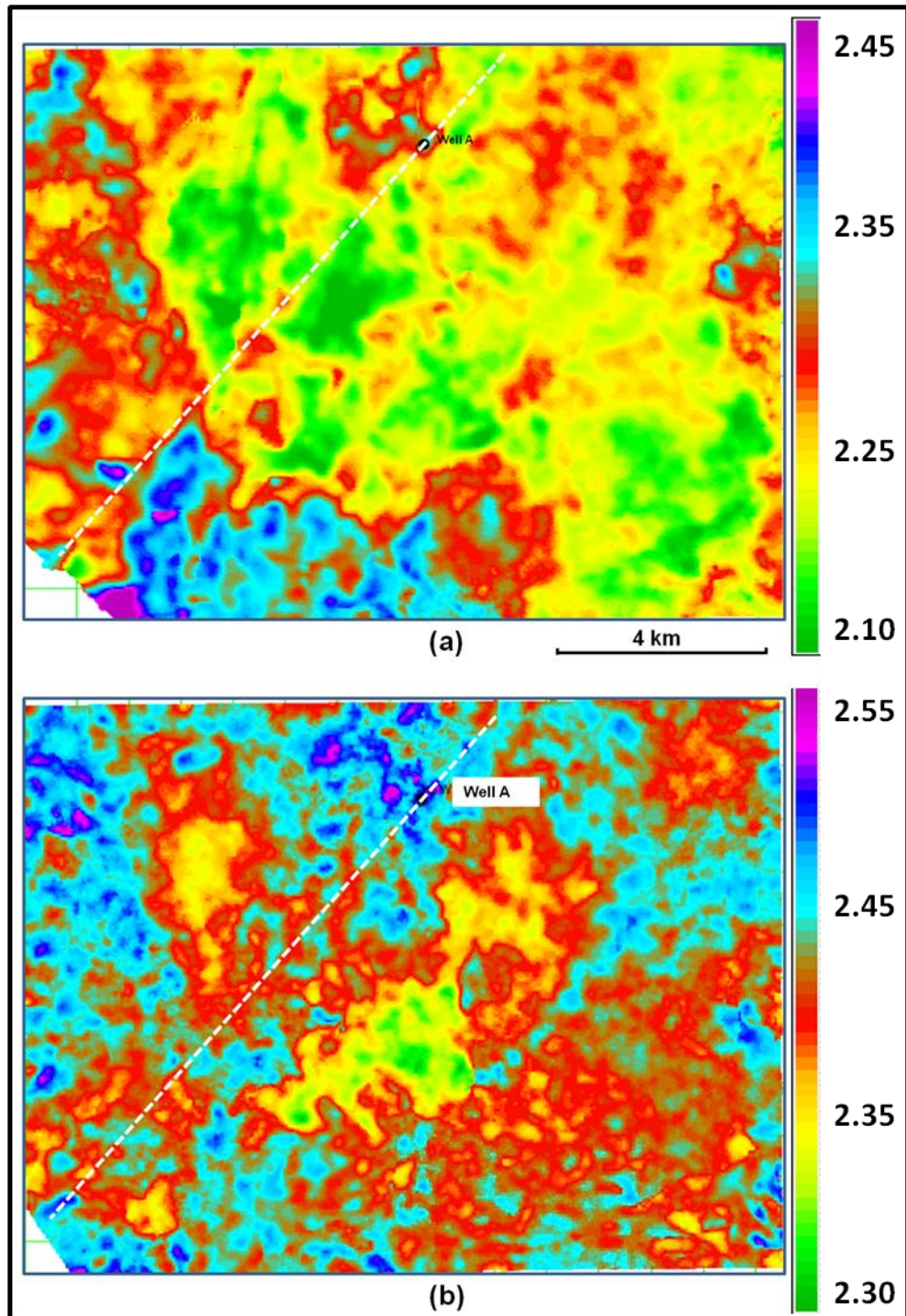


**Figure 3.14: (a) Interval  $V_p/V_s$  map from the Fort Simpson Formation to the base of Muskwa Formation. (b) Interval  $V_p/V_s$  map from the Fort Simpson Formation to the Evie Formation. Dashed white line indicates the location of the seismic line shown in Figure 3.9.**

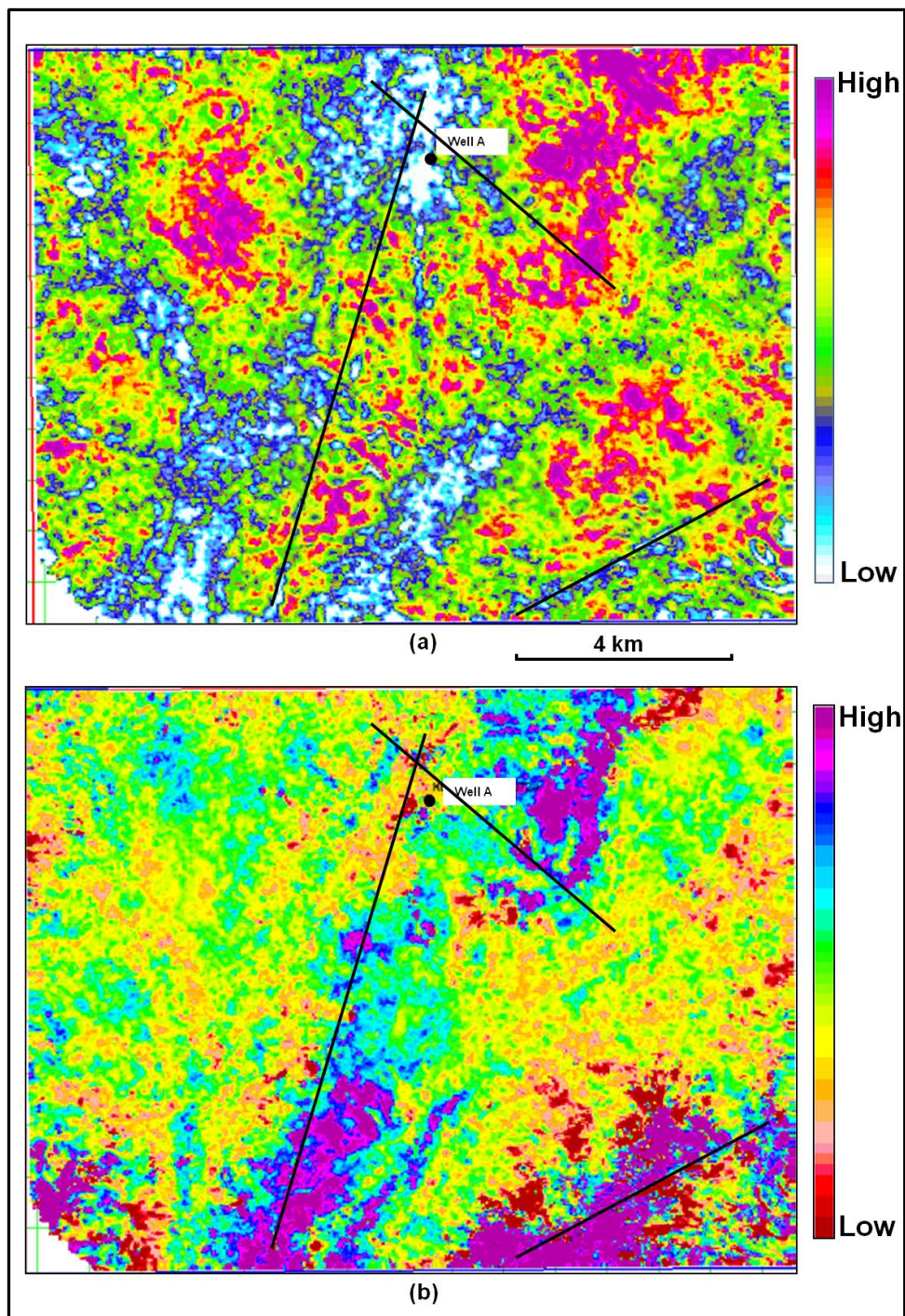


**Figure 3.15: (a) RMS Amplitude extracted with a 30 ms window centered at the base of Muskwa shale horizon. Blue color indicates low amplitude area. (b) Instantaneous frequency map extracted with a 30 ms window centered at the base of Muskwa shale seismic horizon. Red & yellow colors indicate, areas of low instantaneous frequency.**

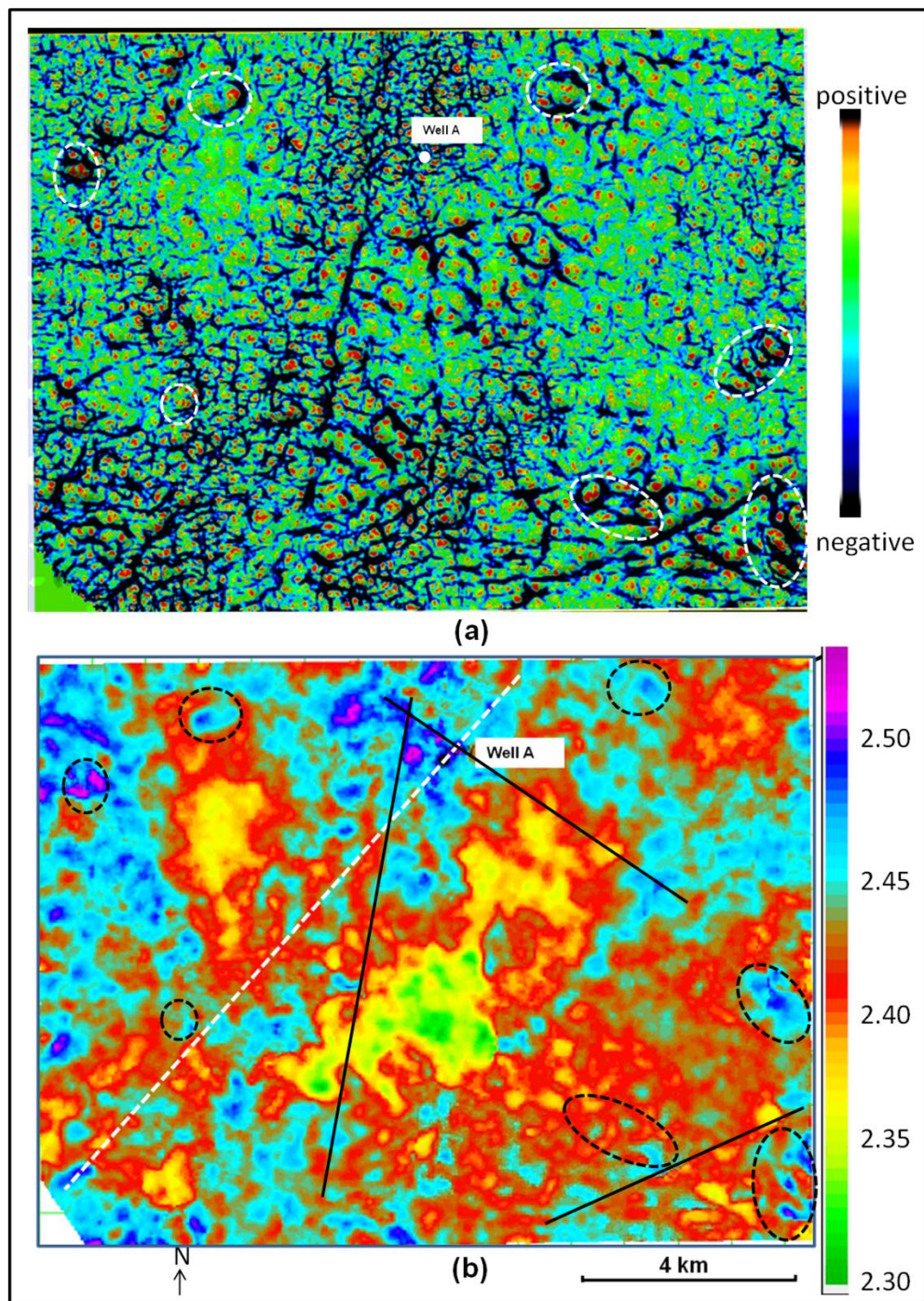


**Figure 3.16: (a) Horizon-slice through most negative curvature volume at the base of the Muskwa shale horizon. Blue color indicates negative curvature values. (b) Interval  $V_p/V_s$  map from the Fort Simpson Formation to the Evie Formation. Blue color indicates high  $V_p/V_s$  values. Black solid lines indicate interpreted faults that have been mapped using curvature at this level and dashed black & white circles identify circular features which are interpreted to be possible mounds.**

3.14a, Figure 3.14b and Figure 3.16b), low amplitude (Figure 3.15a), and low instantaneous frequency (Figure 3.15b).

### **3.9 Summary**

Curvature attribute analyses enhanced the structural interpretations from these data, such as faults and fractures and enable mapping their lateral continuity throughout the seismic volumes. Both horizon and volume-based most-negative curvature were found to be the most useful to map fault and fracture trends at both the Exshaw and Muskwa shale gas targets. At the Exshaw level, the curvature shows one main fault trend: northwest-southeast trending normal faults that dip toward the southwest. At the Muskwa Formation, three major fault trends have been identified and have different features and trends compared to the faults mapped at the shallower formations. These deeper faults include one reverse fault trending southwest-northeast, one normal fault trending north-south, and one strike slip fault trending northwest-southeast.

Vp/Vs interval extraction at both shale reservoir targets showed that higher Vp/Vs values are mapped near the major faults. These higher Vp/Vs values are characterized by low amplitudes and low instantaneous frequency. The integration of attributes yields an improved overall structural interpretation. The most negative curvature map highlights the major fault and fracture trends and the Vp/Vs map, the instantaneous frequency map as well as the amplitude maps highlights potential highly fractured areas within the shale reservoirs.

## **CHAPTER 4: AVO analysis and attributes**

### **4.1 Introduction**

AVO stands for Amplitude Variation with Offset and it refers to the change in reflection amplitude with a change in incident angle of the seismic energy at a reflector. Also, it is considered in exploration seismology as one of the most effective methods for detecting hydrocarbons (Lines and Newrick, 2004).

Pre-stack 3D seismic gathers from the HRB dataset were used for AVO analysis for both shale gas targets (Exshaw and Muskwa reservoirs) using Hampson - Russell AVO software. The goal was to assess AVO as a method to recognize potential anomalies that might be favourable for shale gas development.

### **4.2 Theory**

The AVO concept is derived from the Zoeppritz equation's which describe how the reflection coefficient at any boundary varies as a function of the incident angle, the P-wave velocity, the S-wave velocity, and the density (Figure 4.1) (Lines and Newrick, 2004). As shown in Figure 4.1, incident P-wave energy on an interface will generate into four resultant wavelet modes: reflected P-wave, reflected S-wave, transmitted P-wave, and a transmitted S-wave (Sheriff, 1991). Due to the fact that the Zoeppritz's equations solution is so complex, several approaches to AVO equations have been developed to represent the approximations to Zoeppritz's equations (Aki and Richards, 1980; Shuey, 1985; and many others). Shuey (1985) developed a simplification of the Zoeppritz equations into two simple terms:

$$R(\theta) \approx A + B \cdot \sin^2(\theta) \quad (4.1)$$

Where  $\theta$  = incident angle

A = Intercept =  $R_0$

$$B = \text{Gradient} = \left( \frac{9}{4} \Delta\sigma - R_0 \right)$$

$\Delta\sigma = \sigma_2 - \sigma_1$  = Poisson's ratio difference between two layers

Shuey's linear approximation (equation 4.1) is the most common equation used in AVO analysis (Lines and Newrick, 2004). It relates the Poisson's ratio ( $\sigma$ ), which in this case represents the rock properties, with the variation of reflection coefficients and it shows that Poisson's ratio plays a major role in determining the AVO anomaly (Lines and

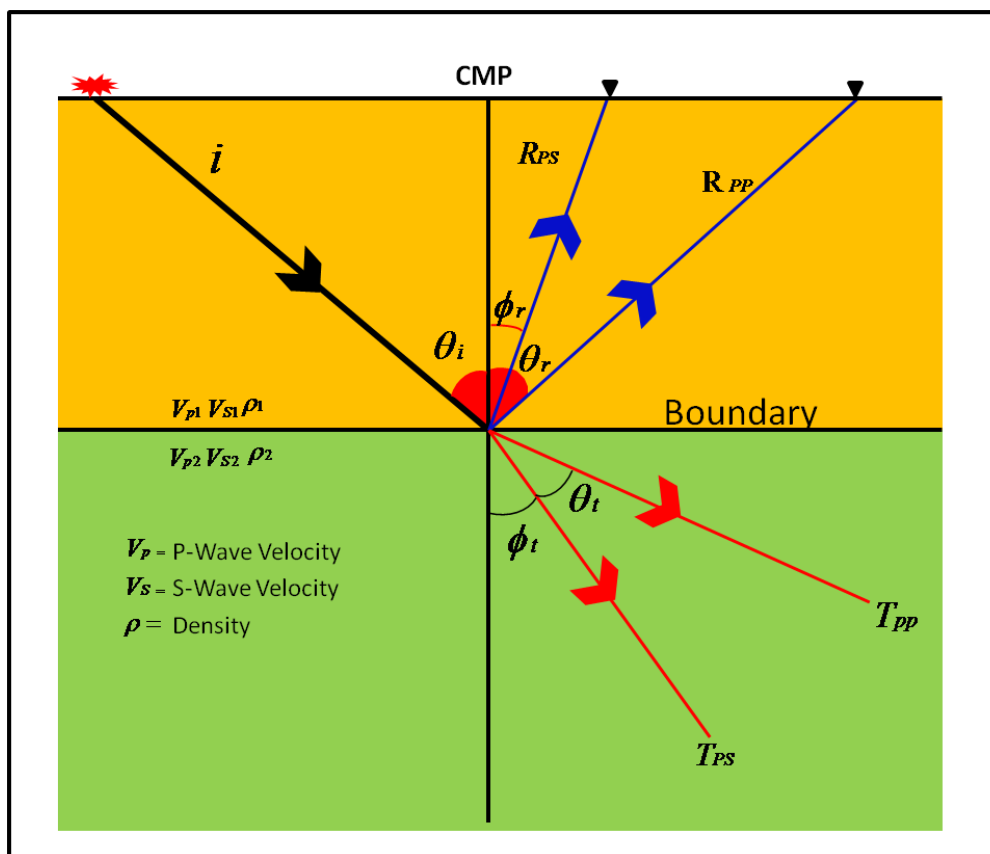


**Figure 4.1: An incident P-wave on a boundary separating two layers converts into four waves: reflected P-wave (Rpp), reflected S-wave (Rps), transmitted P-wave (Tpp) and transmitted S-wave (Tps).**

Newrick, 2004).

The most popular AVO attribute extractions are the intercept (A), the gradient (B) and the scaled Poisson's ratio (A+B). The intercept (A) is the normal incidence P-wave reflectivity ( $R_0$ ), while the gradient (B) is the slope taken by performing a linear regression analysis on the seismic amplitudes over an incident angle range typically of 0 to 30 degrees (Figure 4.2). The sum of the intercept and gradient (A+B) is proportional to the changes Poisson's ratio ( $\Delta\sigma$ ) as shown in equation 4.2 (Varga, 2009):

$$A + B = \frac{9}{4} \Delta\sigma \quad (4.2)$$

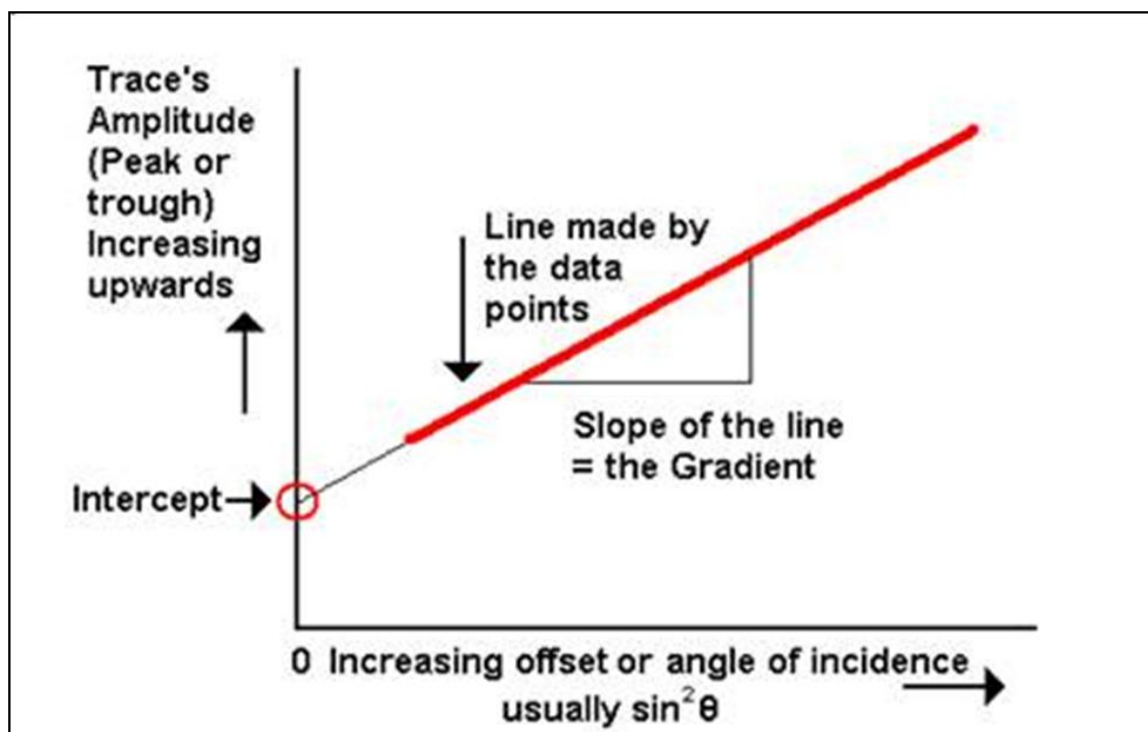


Figure 4.2: Plot showing how the intercept and gradient values have been obtained from the pre-stack gathers after the AVO analysis (from Hampson-Russell, 2007).

### 4.3 AVO and rock properties in shale gas

In sandstone reservoirs, AVO analysis has proved itself to be a direct hydrocarbon indicator (Allen and Peddy, 1993). In carbonate reservoirs, the AVO analysis has been used to detect porosity development within limestone facies effectively, but not for pore fluid assessment (Chacko, 1989). In shales, Draege et al., (2006) and Avseth et al., (2008) studied and modeled the effect of mineralogy and compaction of marine shales on the seismic properties and also on the AVO background trend, as well as the AVO signatures of sandstone reservoirs capped by these shales. They found that the mineralogy alteration from smectite to illite and quartz that took place at 70° C (2 KM burial depth) will increase the rock stiffness, decrease the porosity and decrease the fluid sensitivity of the AVO analysis for both the shale and the underlying sandstone. In order to apply AVO analysis and integrate it to petrophysical rock physics to better highlight reservoir quality in the Devonian shale gas in HRB, well data that includes cores, advanced suites of logs for determining accurate porosity, and mineralogy are required. Unfortunately, we do not have all well information in this study area. However, we can correlate the Vp/Vs interval maps that we computed earlier at the reservoir targets levels (Exshaw and Muskwa) with the scaled Poisson's ratio attribute maps computed from AVO analysis at the same level by:

$$\sigma = \frac{(Vp/Vs)^2 - 2}{2[(Vp/Vs)^2 - 1]} \quad (4.3)$$

Since the lower values of the interval Vp/Vs were attributed to better porosity development within Triassic Montney shale gas reservoir in HRB (Figure 4.3) (Close et al., 2010), lower values of the scaled Poisson's ratio obtained from AVO analysis could

suggest a similar remit for the HRB. The Lower values of both maps delineate possible areas favourable for exploration at the level of Exshaw and Muskwa shale targets.

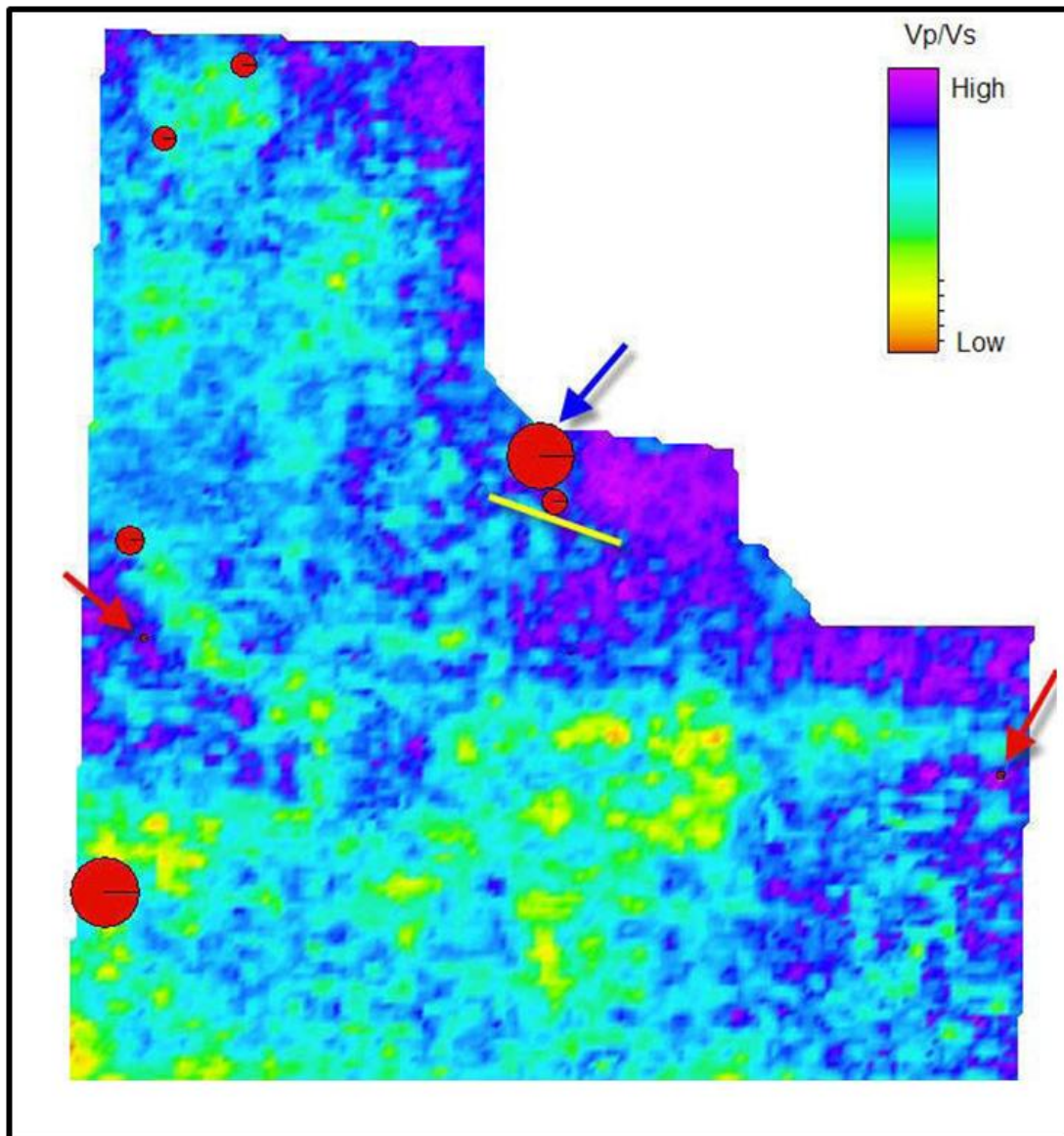


**Figure 4.3: Map of  $V_p/V_s$  ratio and porosity-height from 8 wells through the Lower Doig and Upper Montney. The red arrows highlight wells with very low porosity-height values and correspond in general to areas of higher  $V_p/V_s$ . The blue arrow highlights a well with a large porosity-height at the edge of the seismic data where the inversion is adversely affected by decreased fold. The yellow line is the approximate location of a horizontal well where micro-seismic data were recorded (from Close et al., 2010).**

#### 4.4 AVO analysis of the top of Exshaw shale event

The first step before applying the AVO analysis was to create a super gather. This process helps to increase the signal to noise ratio and reduce the data volume while it maintains the AVO amplitude value (Hampson, 2007). The rolling window that used for the super gather in this dataset is a 3 inline by 3 crossline bins and the output CDP is windowed into 20 traces. The amplitude of the top of Exshaw shale reservoir has Class IV AVO (Figure 4.4) (Rutherford and Williams, 1989 and Castagna et al., 1998) and Figure 4.5 shows a CDP super gather near well A is the study area on the left and on the right of the figure it shows the regression line (gradient) behaviour of the top Exshaw shale reservoir event as well as the crossplot of the gradient versus the intercept (interval between 700 to 950 ms). Incident angles are shown in colours: maximum angle is up to 30°. The amplitude of the top of Exshaw shale reservoir characterized by high negative amplitude, decreasing in absolute value with offset, as shown in Figure 4.5. Figures 4.6 and 4.7 shows the AVO intercept (A) the AVO gradients (B) maps, respectively, extracted from the top of Exshaw shale reservoir event. Both maps show high amplitude values (red and pink colors) that are bounded by the four major normal faults (black solid lines) and separates these blocks. Also, both maps show that they are also severely affected by artifacts generated by a significant channel system within the near surface, indicated by dotted black lines (Figure 4.6 and Figure 4.7).

The scaled Poisson's ratio (A+B) map extraction at the top of Exshaw shale is shown in Figure 4.8. This map is very similar to the AVO gradient map in Figure 4.7 and shows the same anomaly trends. In comparison, Figure 4.9, which shows the 30 ms RMS window extraction of scaled Poisson's ratio (A+B) AVO attribute at the top of Exshaw

shale reservoir. We found that it shows the same AVO anomaly trend (green and yellow) as Figure 4.8, but the effects of the channel artifacts are reduced. Also, Figure 4.9 shows that this anomaly is characterized by high negative amplitudes, shown in cross section (A-B) and which dim toward the southwest.

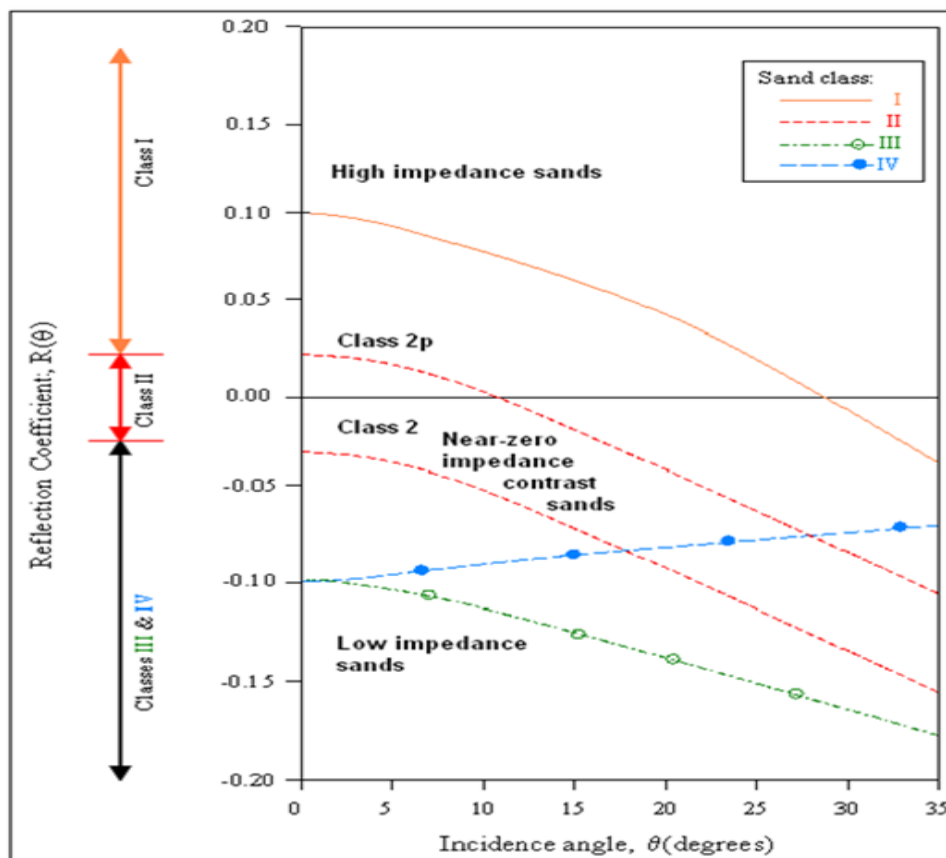


**Figure 4.4: The AVO classification (Rutherford and Williams, 1989, and Castagna et al, 1998).**

The correlation between the extracted scaled Poisson's ratio values at the top of the Exshaw shale event from the AVO analysis and the represented interval  $V_p/V_s$  of the top of the Exshaw shale that computed from the top of the Banff Formation to the top of Tetcho Formation are shown in Figures 4.10a, and 4.10b, respectively. Good correlation between these two maps has been observed. Low  $V_p/V_s$  interval values (Figure 4.10b)

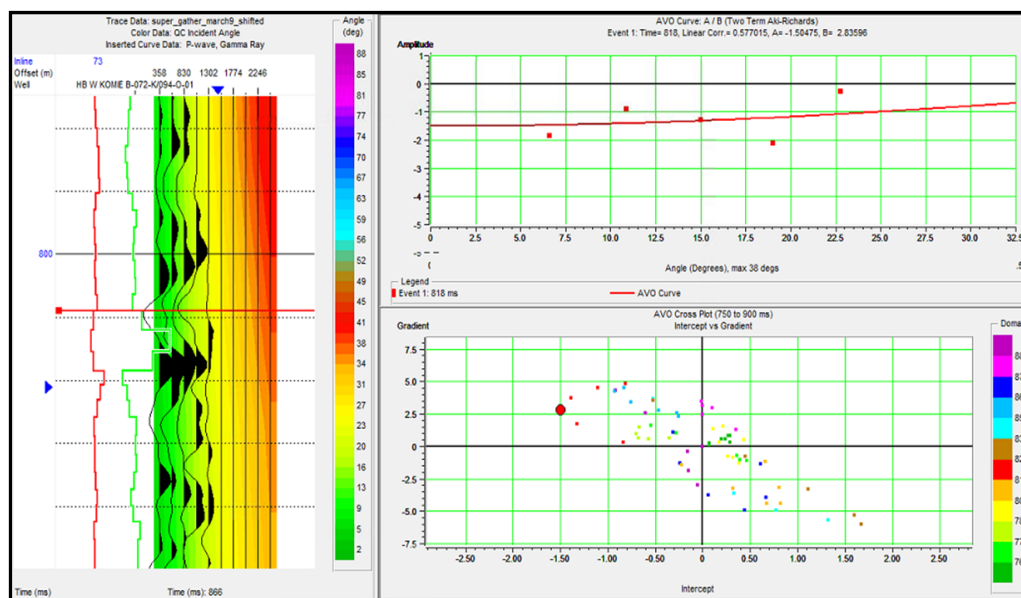


**Figure 4.5: CDP Super Gather near the key well in the area. The background color indicates the incident angle (on the left). The gradient behaviour at the top of the Exshaw shale reservoir (upper right) shows class IV AVO. The gradient versus intercept crossplot is shown on lower right (700-950 ms).**

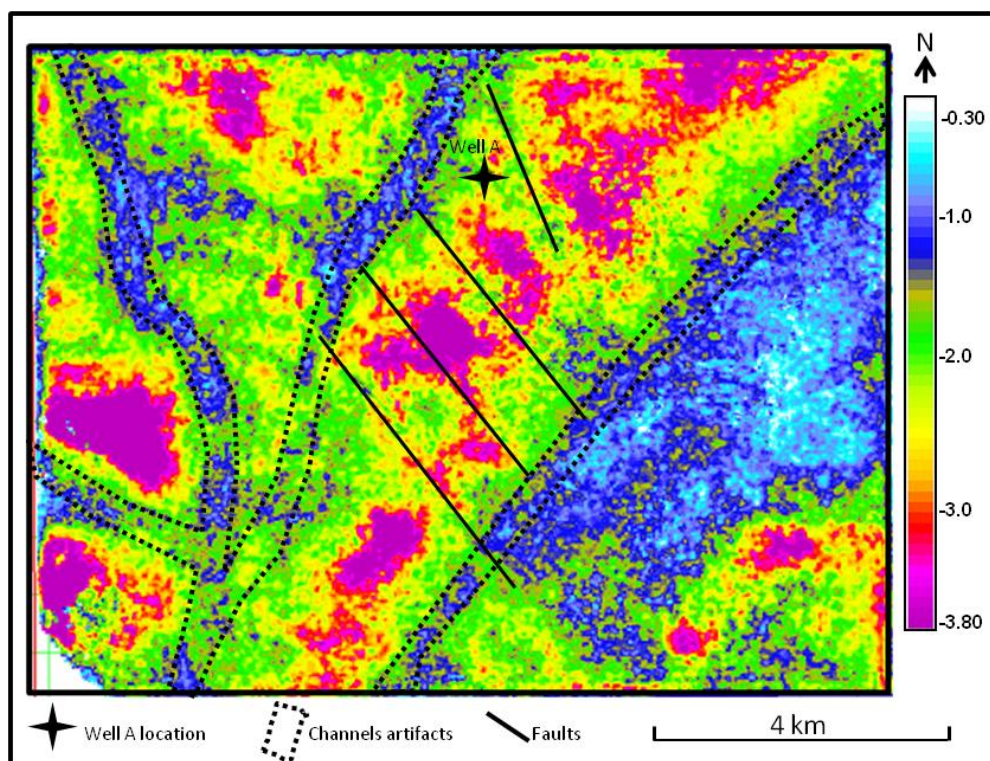


**Figure 4.6: AVO intercept (A) map extracted at the top of Exshaw shale reservoir.**

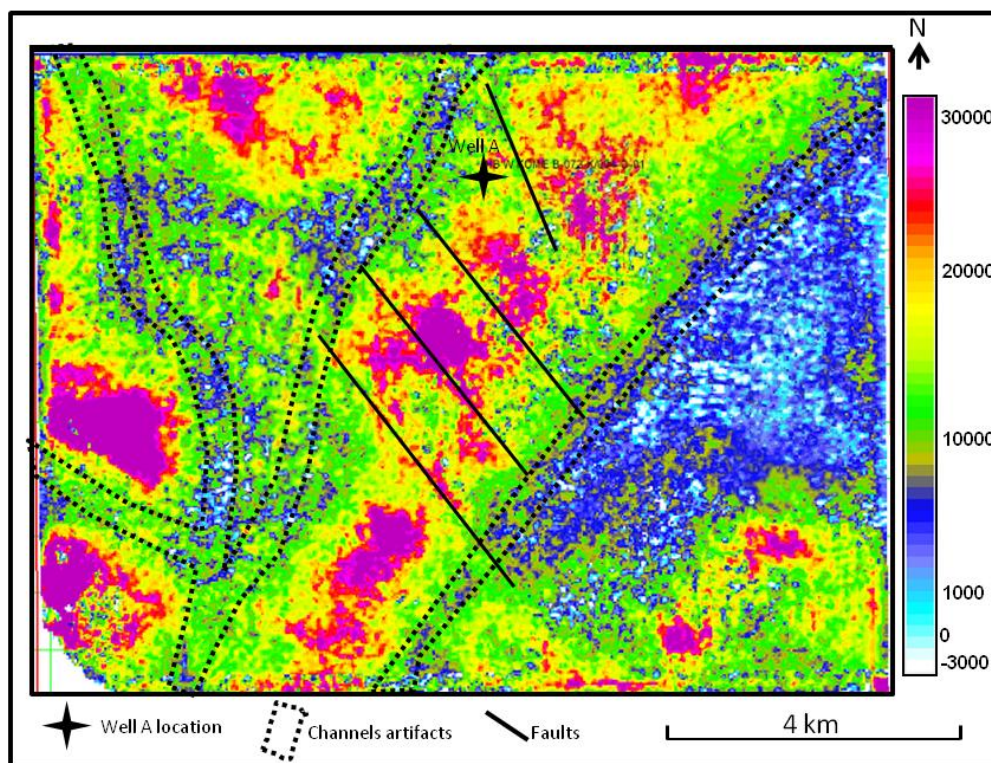


**Figure 4.7:** AVO gradient (B) map extracted at the top of Exshaw shale reservoir.

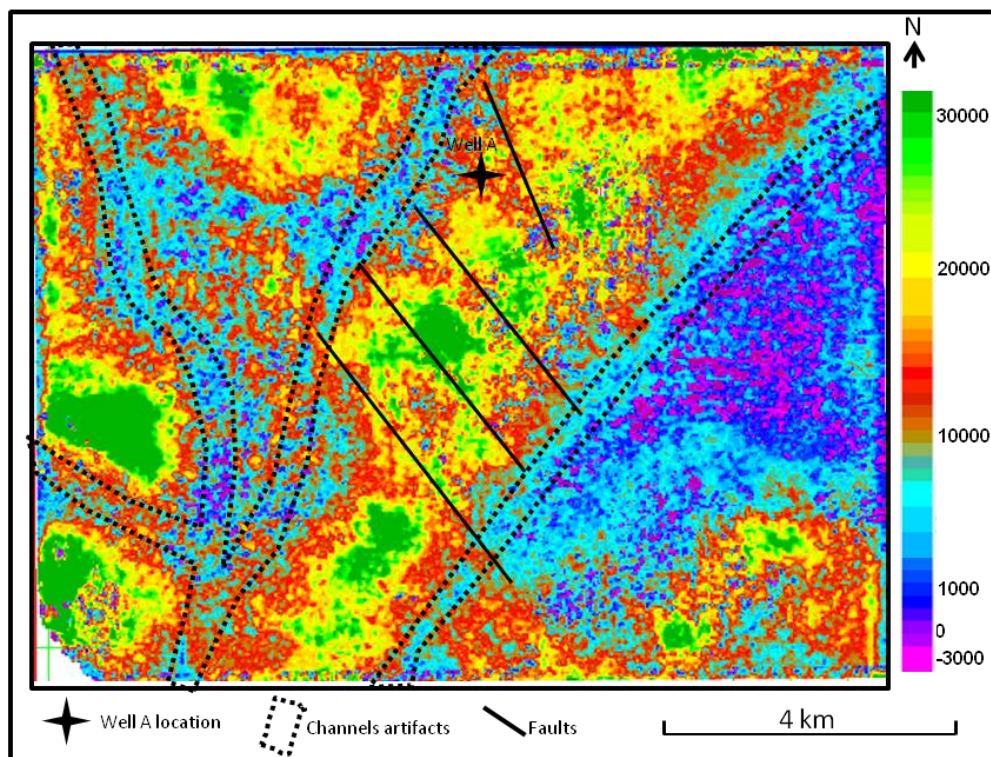


**Figure 4.8:** AVO scaled Poisson's ratio (A+B) map extracted at the top of Exshaw shale reservoir.

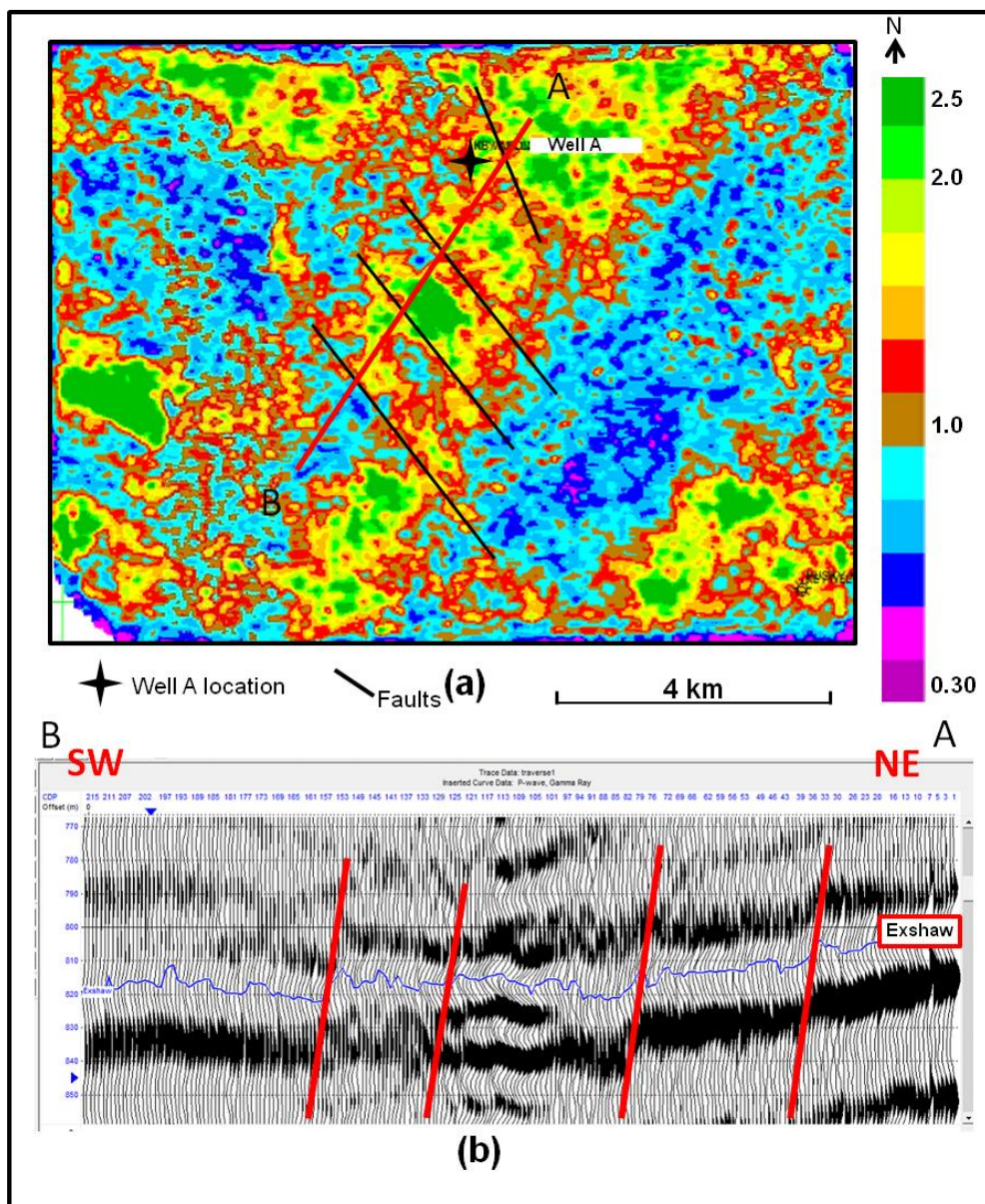


**Figure 4.9: (a) Scaled Poisson's ratio (A+B), 30 ms RMS window AVO attribute extraction map centered at the top of Exshaw shale reservoir (above). (b) A-B cross section of the super stack generated using Hampson - Russell's AVO software (below). Faults are indicated by red solid lines.**

correlate with low scaled Poisson's ratio values (Figure 4.10a). Since the low  $V_p/V_s$  interval values possibly indicate better porosity development within the shale gas interval

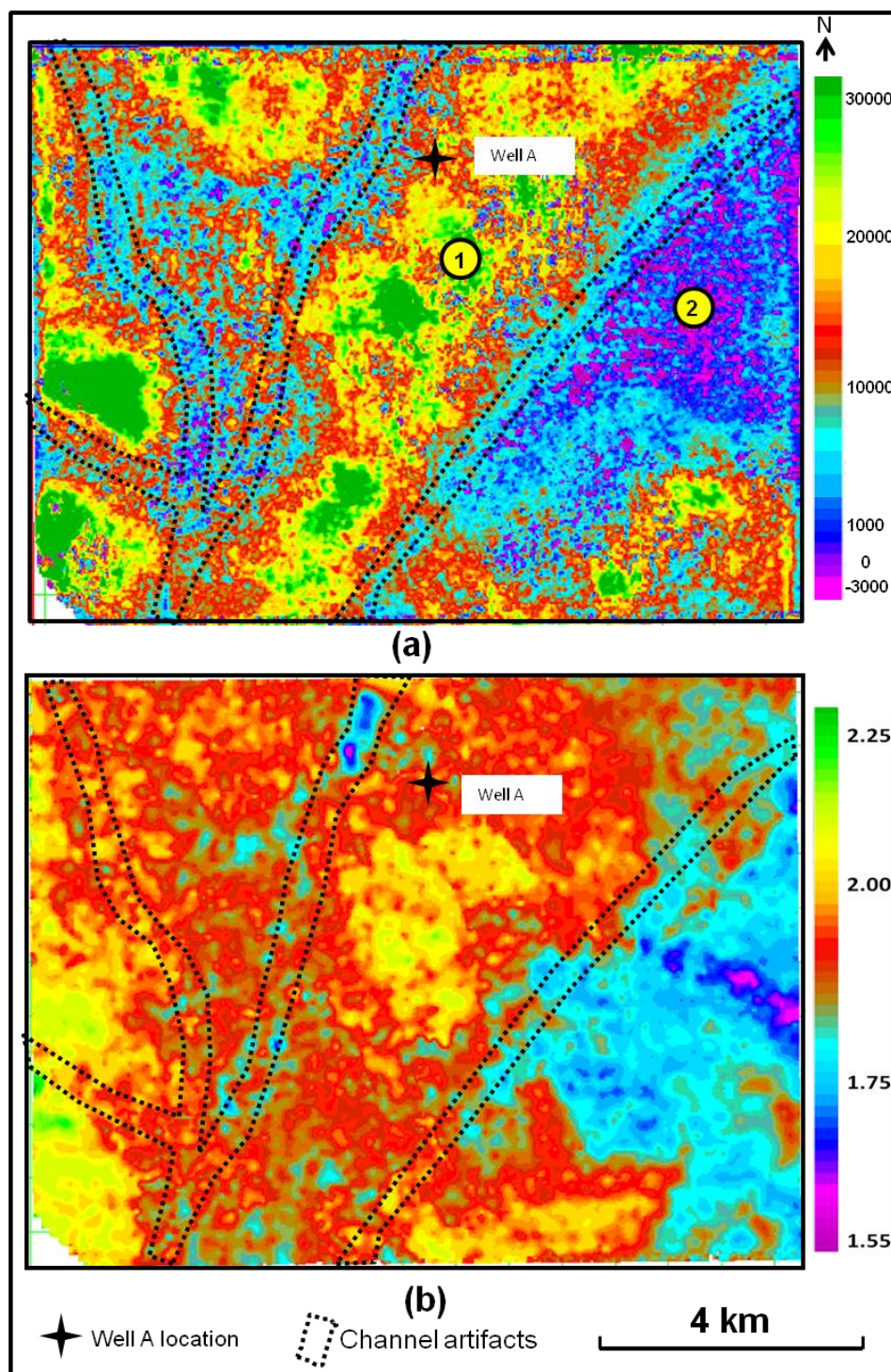


**Figure 4.10: (a) AVO scaled Poisson's ratio (A+B) map extracted at the top of Exshaw shale reservoir. (b) Interval  $V_p/V_s$  map from the Banff Formation to the Tetcho Formation which represents the  $V_p/V_s$  interval at the top Exshaw of shale. Cold colors indicate low values of both attributes. Note the yellow circles are showing the location of two CDP that are showing in Figure 4.11.**

(Close et al., 2010) or possibly facies change from shale to silt (Stewart et al., 2003), the low scaled Poisson's ratio values that obtained from the AVO analysis at the top of the Exshaw shale may indicate the same thing. Figure 4.11 shows two CDP gathers; one located at the high scaled Poisson's ratio values of the scaled Poisson's ratio map that extracted at the top of Exshaw shale event indicated by the yellow circle 1 (Figure 4.10a), and the second CDP gather which indicated by yellow circle 2 located at the low scaled Poisson's ratio values area of the same map (Figure 4.10a) which correlate to low  $V_p/V_s$  interval values extracted at the top of the Exshaw shale event at this CDP location (Figure 4.10b).

#### **4.5 AVO analysis of the base of Muskwa shale event**

For the base Muskwa shale reflector, the AVO behaviour is characterized by a slight amplitude decrease with increasing incident angle and has a Class I AVO response (Figure 4.12) (Rutherford and Williams, 1989 and Castagna et al, 1998). The intercept and the gradient maps extracted at this level are shown in Figure 4.13 and Figure 4.14, respectively. These maps represent RMS AVO attribute values extracted over a 30 ms window centered at the base of Muskwa shale reflector shown in Figure 4.12. Both maps show a similar trend of AVO anomalies. However, the major faults mapped at this level, highlighted in solid black lines do not show any apparent relationship to the AVO anomaly. The effect of the channel artifacts are still seen in this level, although it is much less when compared with these artifacts at the Exshaw shale level (Figure 4.6 and Figure 4.7). Figure 4.15 shows the RMS scaled Poisson's ratio (A+B) map calculated using a 30 ms window centred at the base of the Muskwa shale reflector. This map is somewhat

similar to the gradient map in Figure 4.14, with the higher AVO anomalies being highlighted in green and yellow. Figures 4.16a and 4.16b show the correlation between the extracted scaled Poisson's ratio values

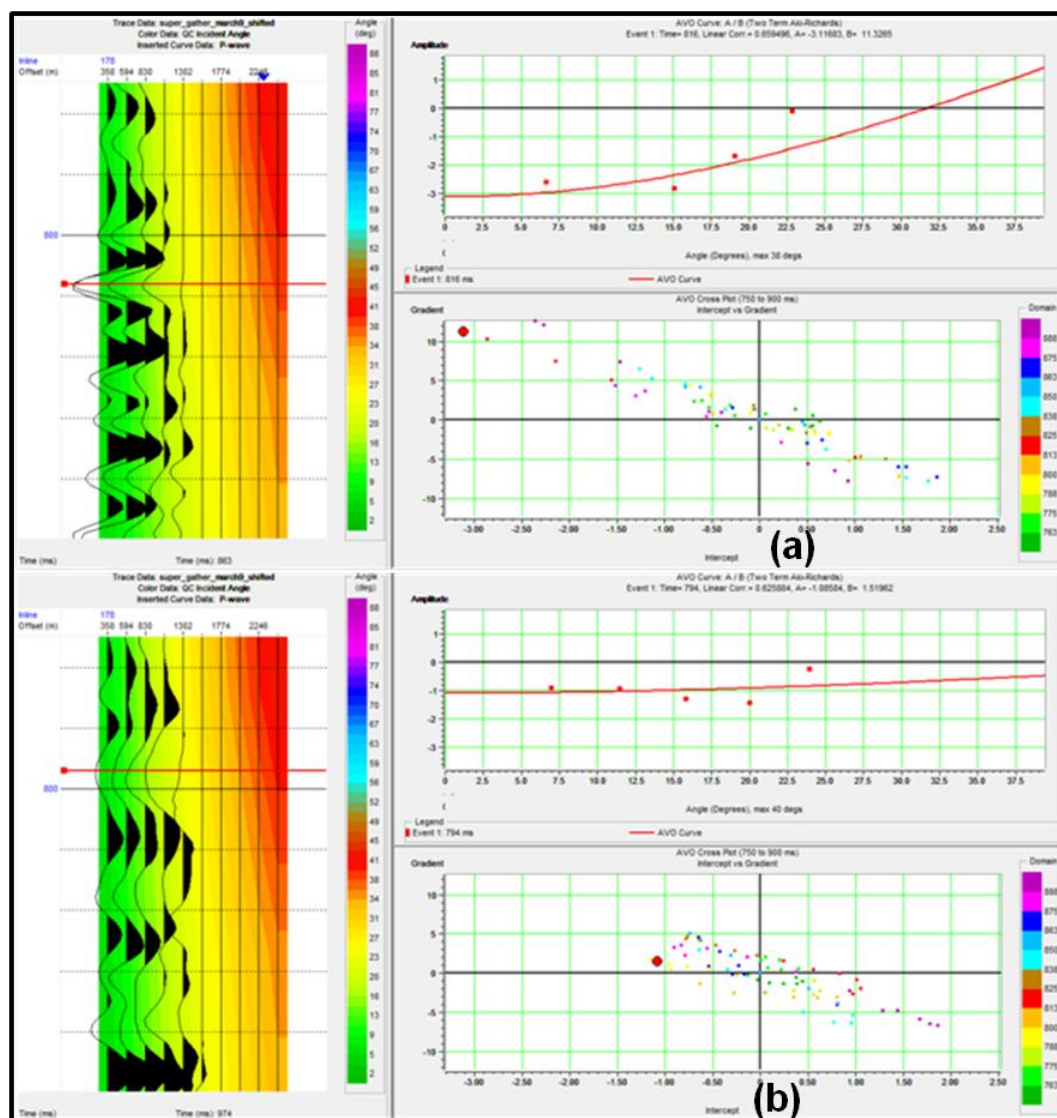


**Figure 4.11: (a) CDP super gather chosen from the high gradient values area. (b) CDP Super Gather chosen from the low gradient values area. The background color of the gather indicates the incident angle (on the left). The gradient behaviour at the top of the Exshaw shale reservoir (upper right of both CDPs) shows how the gradient decreases from high value (upper CDP) to low gradient value (Lower CDP). The gradient versus intercept crossplot is shown on lower right of both CDPs (750-900 ms). Refer to Figure 4.10 for the location of these two CDPs.**

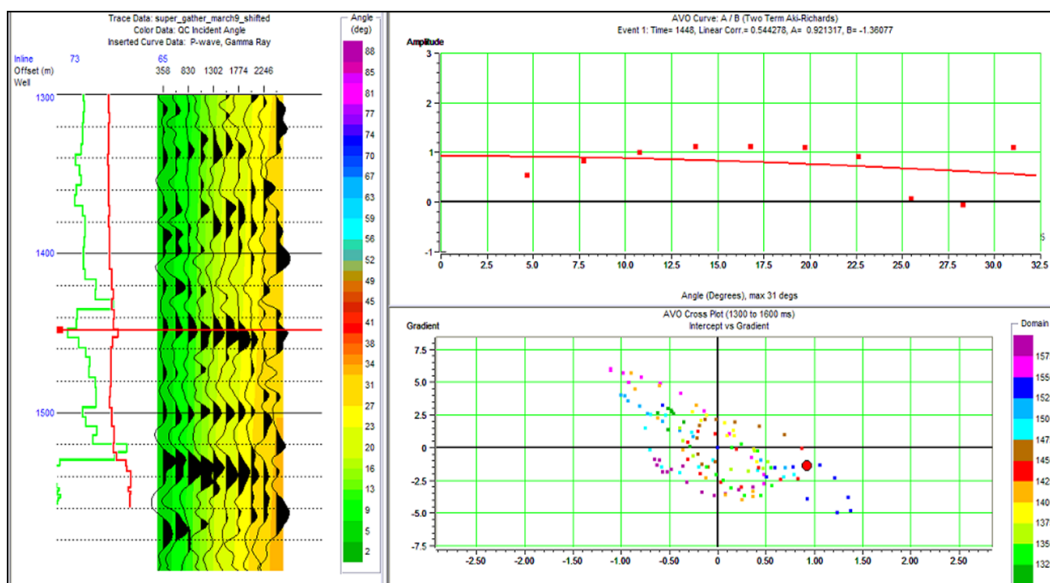


**Figure 4.12: CDP gather near the key well in the area and the background color indicates the incident angel (on the left). The gradient behaviour at the base of the base Muskwa shale reservoir (upper right) shows the amplitude is decreasing with angle. The gradient versus intercept crossplot is shown on lower right for interval at the level of Base Muskwa event between 1300 to 1600 ms.**

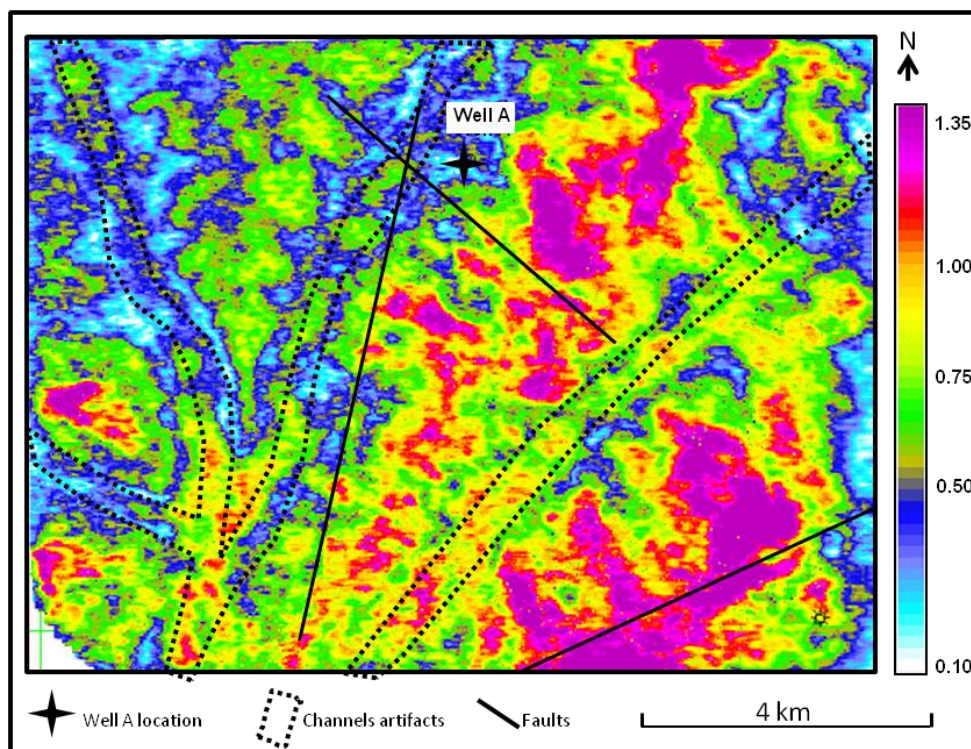


**Figure 4.13: RMS AVO intercept map extracted over a 30 ms window centred at the base of Muskwa shale event. The solid lines indicate the interpreted major faults at this level. The dotted black lines identify artifacts generated by channels within the near surface.**

at the base of the Muskwa shale event from the AVO analysis and the represented interval  $V_p/V_s$  of the base of the Muskwa shale that was computed from the top of the Fort Simpson Formation to the top of Evie Formation. The low values of both maps are shown in cold colors (purple and blue) and correlation between these two maps is reasonable but not as good as the correlation obtained at the Exshaw level. The reason of not having good correlation between attributes above, could be attributed to the larger picking errors of the base of the Muskwa Formation and the top of Evie Formation on the PS data due to the low frequency content. Figure 4.17 shows two CDP gathers that are chosen from different location. The first CDP located at the high scaled Poisson's ratio values of the scaled Poisson's ratio map that extracted at the top of Exshaw shale event indicated by the red circle 1 (Figure 4.16a). The second CDP gather which indicated by red circle 2 (Figure 4.16a) located at the low scaled Poisson's ratio values area that correlate with low  $V_p/V_s$  interval values extracted at the base of the Muskwa shale event at this CDP location (Figure 4.16b) and perhaps indicates improved reservoir porosity at this level.

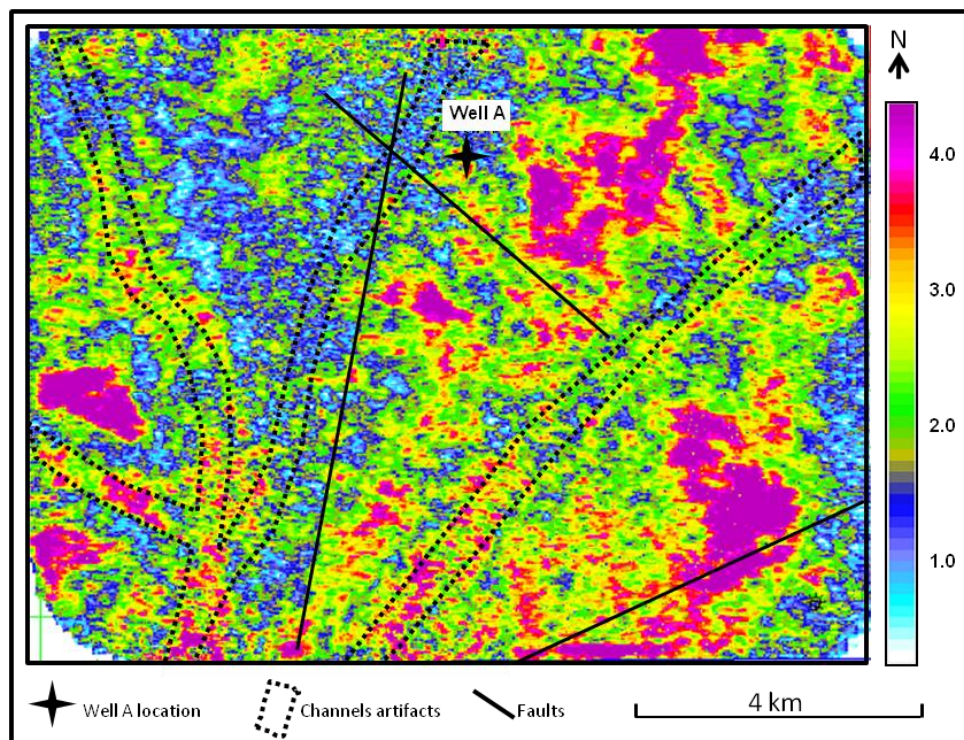


**Figure 4.14: RMS AVO gradient attribute map extracted over a 30 ms window centred at the base of Muskwa shale event.**

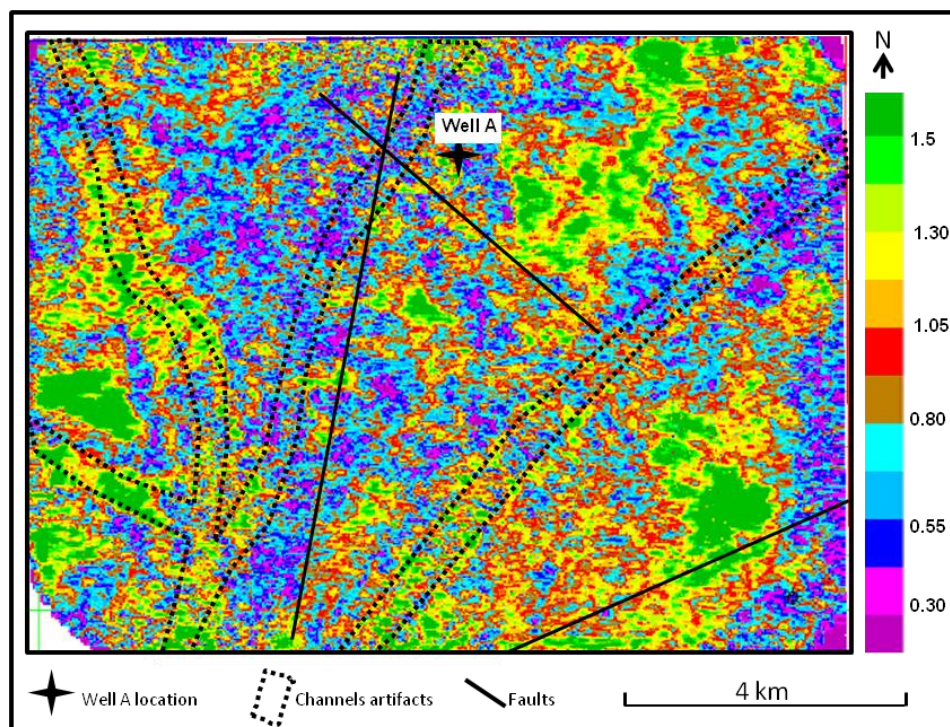


**Figure 4.15: RMS scaled Poisson's ratio map extracted over a 30 ms window centred at the base of Muskwa shale event.**

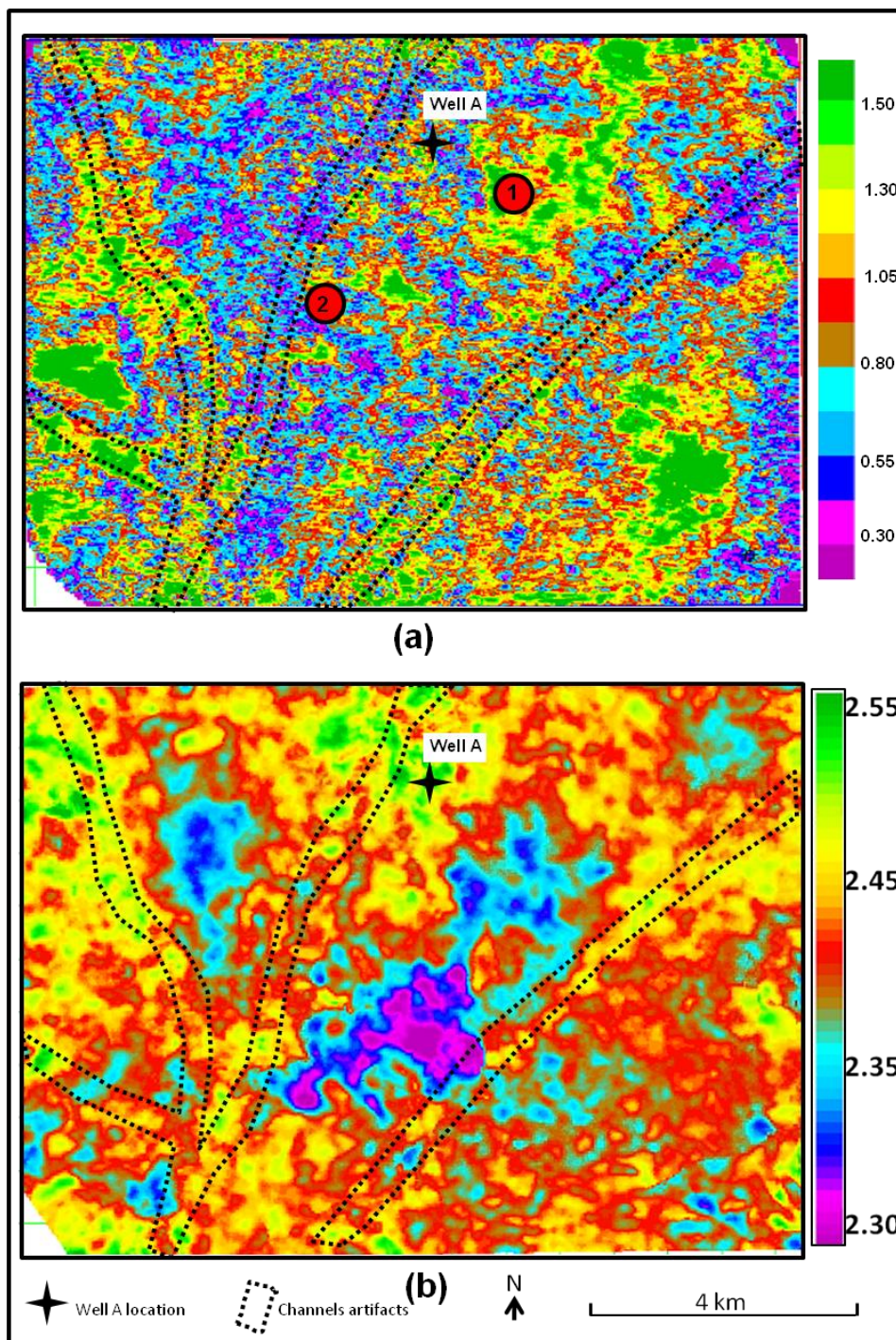
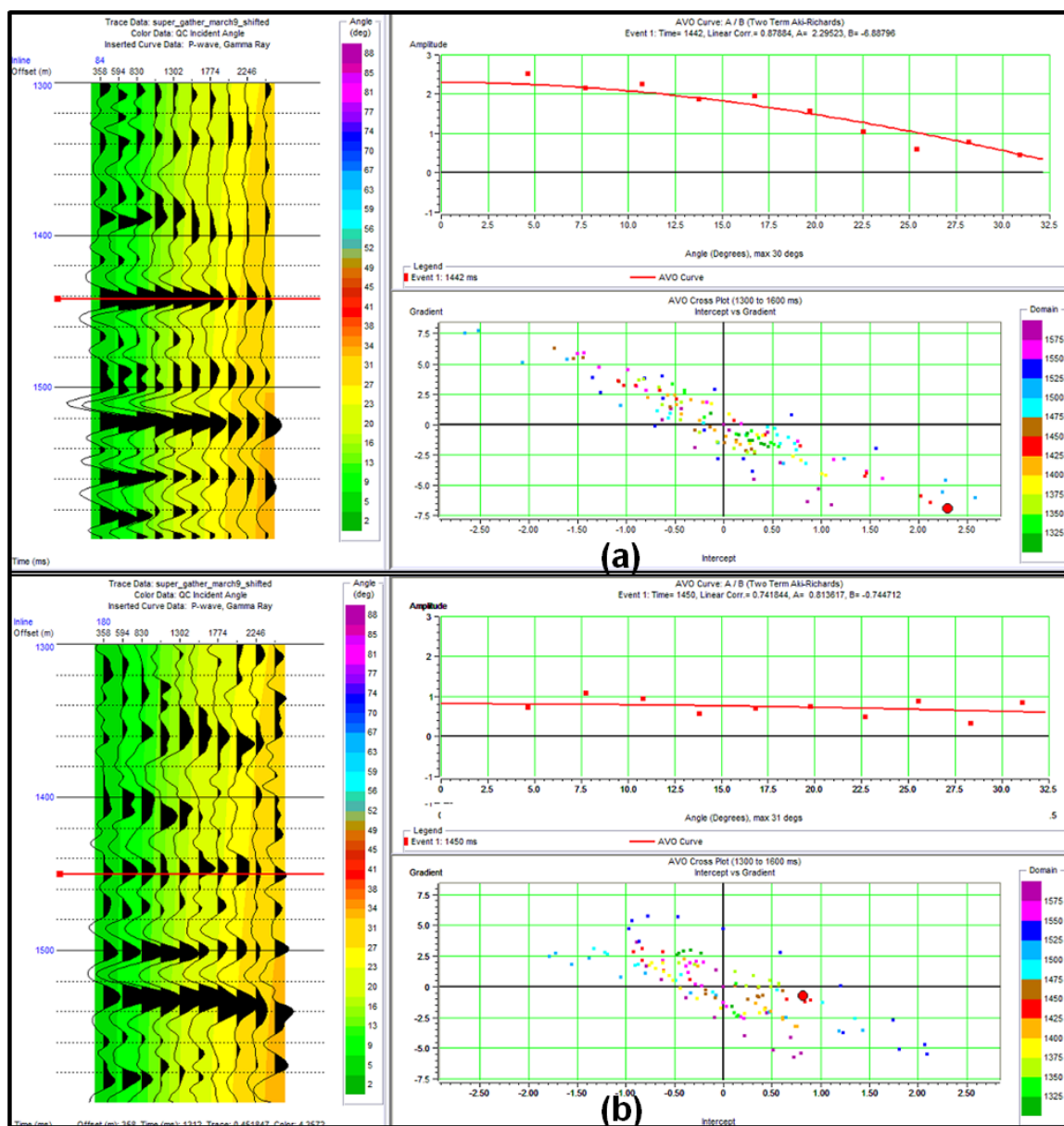


Figure 4.16: (a) AVO scaled Poisson's ratio (A+B) map extracted at the base of Muskwa shale reservoir. (b) Interval  $V_p/V_s$  map from the Fort Simpson Formation to the Evie Formation which represents the  $V_p/V_s$  interval at the base of the Muskwa shale. Cold colors (purple and blue) indicate low values of both attributes



**Figure 4.17: (a) CDP super gather chosen from the high scaled Poisson's ratio value area. (b) CDP super gather chosen from the low scaled Poisson's ratio value area. The background color of the gather indicates the incident angle (on the left). The gradient behaviour at the base of the Muskwa shale reservoir (upper right of both CDPs) shows how the gradient decreases from high value (upper CDP) to low gradient value (lower CDP). The gradient versus intercept crossplot is shown on lower right of both CDPs (1300-1600 ms). Refer to Figure 4.16 for the location of these two CDPs highlighted by red circles.**

#### 4.6 Summary

3D pre-stack gathers from the HRB PP volume were input for AVO analyses in order to identify seismic anomalies that outline possible areas that may indicate favourable Exshaw and Muskwa shale reservoirs.

The resulting AVO attribute maps, namely intercept (A), gradient (B) and scaled Poisson's ratio (A+B), shows similar AVO anomaly trends at both reservoir targets. At the Exshaw shale level, the interpreted four normal faults mapped at this level showed some control on the resultant AVO anomalies and separate them in blocks. In comparison, at the Muskwa level the interpreted faults did not show any control on the resultant AVO anomalies. The AVO attribute maps extracted from both levels (Exshaw and Muskwa) showed that they were contaminated by artifacts generated by significant channels within near surface. The extraction of using RMS values for AVO attributes shows it is less sensitive to the channel artifacts than the extraction of the absolute values.

The integration and high correlation of the scaled Poisson's ratio computed from the AVO analysis with the interval  $V_p/V_s$  maps computed at the level of Exshaw and Muskwa reservoir suggest areas of possible increased reservoir potential by these maps. The lower  $V_p/V_s$  interval proved to indicate better porosity development within Triassic Montney shale gas reservoir in HRB (Figure 4.3) (Close et al., 2010), so it is encouraging for the Devonian Exshaw and Muskwa shale gas reservoirs in the same basin.

## **CHAPTER 5: CONCLUSIONS AND RECOMMENDED FUTURE WORK**

In this thesis, a detailed pre-stack and post-stack interpretation of 3D multicomponent seismic dataset from the Horn River Basin was undertaken to highlight possible prospective zones within the Exshaw and Muskwa shale gas reservoirs in the Horn River Basin. The main conclusions drawn from this thesis are:

- Curvature attribute analyses enhanced the structural interpretations from these data, such as faults and fractures and enabled mapping their lateral continuity throughout the seismic volumes. Both horizon and volume-based most-negative curvature was found to be the most useful to map fault and fracture trends in both the Exshaw and Muskwa formations. At the Exshaw level, the curvature shows one main fault trends: northwest-southeast trending normal faults that dip toward the southwest. At the Muskwa level, the curvature images show quite different major fault trends: north-south trending normal fault, northeast-southwest trending reverse faults, and northwest-southeast strike-slip fault.
- The faults are generally better imaged on the PP data volumes than on the PS data volumes and the fractures predicted using curvature attribute are those fractures that are close to the major faults and their trends are generally parallel to the faults.
- Interval  $V_p/V_s$  extraction at both shale reservoir targets showed that higher  $V_p/V_s$  values are mapped in the vicinity of the major faults. These areas of higher  $V_p/V_s$  values are also characterized by reflections with low amplitudes and low instantaneous frequency. The integration of attributes yields an improved overall

structural interpretation. The most negative curvature map highlights the major fault trends and the  $V_p/V_s$  map, the instantaneous frequency map as well as the amplitude maps highlights potentially highly fractured areas within the shale reservoir that have been induced by the major faults. The AVO attribute maps namely intercept (A), gradient (B) and scaled Poisson's ratio (A+B), show similar AVO anomaly trends at both reservoir targets. At the Exshaw shale level, the four normal faults mapped at this level influenced the resultant AVO anomalies and separated them into discrete blocks. In comparison, at the Muskwa level, the interpreted faults did not show any relationship to the AVO anomalies. The AVO attribute maps extracted from both levels (Exshaw and Muskwa) showed that they were contaminated by artifacts generated by channels within near surface. The extraction of RMS values for AVO attributes shows it is less sensitive to the channel artifacts than the extraction of the absolute values.

- The integration and high correlation of the scaled Poisson's ratio computed from the AVO analysis with interval  $V_p/V_s$  maps computed at the level of the Exshaw and Muskwa reservoirs suggest areas of possible increased reservoir potential by these maps. The lower  $V_p/V_s$  interval proved to indicate better porosity development within Triassic Montney shale gas reservoir in HRB, so it is encouraging for the Exshaw and Muskwa in the same basin.

Future work recommendations include calibration of the computed  $V_p/V_s$  generated from this multicomponent seismic data with well data that contain calibrated porosity log that obtained from core and log analysis to confirm the lower  $V_p/V_s$  interval

indicates better porosity. Detection of gas shale using AVO analysis which incorporates the third term (density term) which has been developed By Fatti et al, (1994) and the fluid factor that developed by Smith and Gidlow (1987) is recommended. Fracture detection using P-wave azimuthal anisotropy, and S-wave splitting is also recommended to integrate them with FMI log and curvature results. Last, quantities correlation between the integrated maps like the scaled Poisson's ratio map and the interval  $V_p/V_s$  map are also recommended as future work.

## REFERENCES

- Aki, K., and Richards, P.G., 1980, *Quantitative seismology: Theory and methods*: W. H. Freeman and Co. New York.
- Al-Dossary, S., and K.J. Marfurt, 2006, 3-D volumetric multispectral estimates of reflector curvature and rotation: *Geophysics*, v. 71/5, p. P-41-P51.
- Al Duhailan, M., 2008, *Field Mapping and Seismic Analysis of Fractures*: M.Sc. Thesis, University of Calgary, Department of Geoscience
- Allen, J. L., and M. M. Backus, eds., 1993, *Offset-dependent reflectivity-case studies*: SEG.
- Avseth, P., Draege, A., van Wijngaarden, A.-J., Johansen, T. A., and Jørstad, A., 2008, Shale rock physics and implications for AVO analysis: A North Sea demonstration: *The Leading Edge*, 27, 788–797
- Beaudoin, B., Shaw, J., 2009, *Characterization of the Horn River Basin Thermogenic Shale Gas Play in Northeastern BC*: *Frontiers and Innovation 2009 CSPG CSEG CWLS Convention*
- British Columbia Ministry of Energy and Mines and CBM Solutions. (2005): *Gas shale potential of Devonian strata, northeastern British Columbia*; British Columbia Ministry of Energy, Mines and Petroleum Resources, Resource Development and Geoscience Branch, *Petroleum Geology Special Paper 2005-1*. CD.
- British Columbia Ministry of Energy and Mines and CBM Solutions. (2010): *Ultimate Potential for Unconventional Natural Gas in Northeastern British Columbia's Horn River Basin*; British Columbia Ministry of Energy, Mines and Petroleum, BC MEM/NEB Report: Resources Cat. No. NEB23-165/2011E-PDF: ISBN 978-1-100-18566-8
- Castagna, J.P., M.L. Batzle, and R.L. Eastwood, 1985, Relationships between compressional-wave and shear-wave velocities in elastic silicate rocks: *Geophysics*, 50, 571-581
- Castagna, J. P., and Swan, H.W., and Foster, D. J., 1998, Framework for AVO gradient and intercept interpretation, *Geophysics*, Society of Exploration Geophysicists, 63, 948–956.
- Chacko, S., 1989, Porosity identification using amplitude variations with offset: Examples from South Sumatra: *Geophysics*, 54, 942-951.

- Chopra, S., and Marfurt, K., 2007, Seismic Curvature attributes for mapping faults/fractures, and other stratigraphic features. CSEG Recorder, P37-P41.
- Chopra, S., Marfurt, K., and Alexeev, V., 2006, Practical aspects of curvature computations from seismic horizons. SEG expanded abstract
- Churcher, P.L. and Majid, A.H. 1989. Similarities between the Tangent-Wabamun type play of the Alberta Basin and the Albion-Scipio type play of the Michigan Basin. *Bulletin of Canadian Petroleum Geology*, v. 37, p. 241-245.
- Close, D.I., Stirling, S., Cho, D., and Horn, F., 2010, An integrated workflow for Shale Gas in the Western Canadian Sedimentary Basin: Surface seismic to stimulation: AAPG convention, April 11-14, New Orleans, Louisiana, Search and Discovery article #40569 Web accessed 3rd September 2011  
<http://www.searchanddiscovery.com/documents/2010/40569close/images/close.pdf>
- Currie, J.B., 1974, Study Examines Fracture Porosity and Permeability in Stratigraphic Traps: *Oil and Gas Journal*, June 24, pp. 178–181.
- Draege, A., M. Jakobsen, and T. A. Johansen, 2006a, Rock physics modelling of shale diagenesis: *Petroleum Geoscience*, 12, 49–57.
- Fatti, J.L., Smith, G.C., Vail, P.J., and Levitt, P.R., 1994, Detection of gas in sandstone reservoirs using AVO analysis: a 3-D seismic case history using the Geostack technique: *Geophysics*, 59, 1362-1376.
- Eaton, D. W; Ross, Gerald M; Hope, Jacqueline, 1999. The rise and fall of a cratonic arch; a regional seismic perspective on the Peace River Arch, Alberta. *Bulletin of Canadian Petroleum Geology*, v. 47, p. 346-361.
- Gray, F.F. and Kassube, J.R., 1963, Geology and stratigraphy of Clarke Lake gas field, British Columbia. *Bulletin of the American Association of Petroleum Geologists*. V. 47, p. 467-483.
- Griffin, D.L., 1965, The facies front of the Devonian Slave Point-Elk Point sequence in northeastern British Columbia and the Northwest Territories. *Journal of Canadian Petroleum Technology*, v. 4, p. 13-22.
- Hampson-Russell package, 2007, Geoview, on-line software guide.
- Hunt, L., S., Reynolds, T., Brown, S., Hadley, J., Downton, and S., Chopra, 2010, Quantitative estimate of fracture density variations in the Nordegg with azimuthal AVO and curvature: A case study, *The leading Edge*, 29, 1122-1137

- Jianming, T., Yue, H., and Xiangrong, X., 2009, Application of Converted-Wave 3D/3-C Data for Fracture Detection in a Deep Tight-Gas Reservoir: The Leading Edge, 28, no. 7, 826-837
- Kuuskraa, V. A., and Stevens, S. H., 2009, Worldwide Gas Shales and Unconventional Gas: ARI Status Report
- Li, G., Diaz E., Grader, A., Armbruster, M., and Nur, A., 2009, Digital rock physics for oil sands and gas shales. Canadian Well Logging Society Journal, in press.
- Lines, L.R., and Newrick, R.T., 2004, Fundamentals of Geophysical interpretation, SEG monograph series. SEG Publications, Tulsa, Oklahoma.
- Lynch, S.G., 2008, More than Meets the Eye – A Study in Seismic Visualization: Ph.D Thesis, University of Calgary, Department of Geoscience
- Marfurt K. J. and Chopra S., 2008, 3D Seismic attributes for prospect identification and reservoir characterization, Doodle train course.
- Margrave, G.F., Lawton, D.C., and Stewart, R.R., 1998, Interpreting channel sands with 3C-3D seismic data: The Leading Edge, 17, 509-513.
- Mavko, G., 2010, Rock physics constraints on seismic signatures of fracture <http://www.slideshare.net/timaou01/seismic-signature-of-fractures>
- McClay, K.R., Insley, M.W. and Anderton, R. 1989. Inversions of the Kechika Trough, northeastern British Columbia, Canada. In: Cooper, M.A. and Williams, G.D. (Eds.) Inversion Tectonics Meeting, Geological Society Special Publication 44, p. 235-257.
- McPhail, S., Walsh, W., and Lee, C., 2009, Shale units of the Horn River Formation, Horn River Basin and Cordova Embayment, Northeastern British Columbia: British Columbia Ministry of Energy, Mines and Petroleum Resources
- Morrow, D.W. and Geldsetzer, H.H.J., 1988. Devonian of the eastern Canadian cordillera. In: Devonian of the World. Canadian Society of Petroleum Geology, Memoir 14, v.1, p. 85-121.
- Nelson, R., Geologic Analysis of Naturally Fractured Reservoirs, Contributions in Petroleum geology and engineering, Vol. 1, Gulf Publishing Co., Houston, Texas (2001).
- Nieto, J., Bercha R. and Chan, J., 2009, Shale gas petrophysics- Montney and Muskwa, are they Barnett look-alikes?. Canadian Well Logging Society Journal, in press.

- Richards, B.C. 1989. Upper Kaskaskia Sequence: uppermost Devonian and Lower Carboniferous, Chapter 9. In: Western Canada Sedimentary Basin, a Case History. B.D. Ricketts (ed.). Canadian Society of Petroleum Geologists, p. 165-201.
- Richards, B.C., Barclay, J.E., Bryan, D., Hartling, A., Henderson, C.M. and Hinds, R.C., 1994, Carboniferous strata of the Western Canada Sedimentary Basin. In: Geological Atlas of the Western Canada Sedimentary Basin, G.D. Mossop and I Shetsen, eds., Canadian Society of Petroleum Geologists, p.221-249.
- Roberts, A., 2001, Curvature attributes and their application to 3-D interpreted horizons: First Break, v. 19/2, p. 85-100.
- Ross, G. and Stephenson, R.A. 1989. Crystalline basement; the foundation of the Western Canada Sedimentary Basin. In: Ricketts, B.D. (Ed.), Western Canada Sedimentary Basin; a case history, p. 33-45.
- Rutherford, S.R. and Williams, R.H., 1989, Amplitude-versus-offset variations in gas sands: Geophysics, 54, 680-688.
- Sandberg, C.A., Poole, F.G., Johnson, J.G. 1988. Upper Devonian of Western United States. In: Devonian of the World. N.J. McMillan, A.F. Embrey and D.J. Glass (Eds.), Proceedings of the Canadian Society of Petroleum Geologists International Symposium, Devonian System I. p.183-220.
- Savoy, L.E. and Mountjoy, E.W. 1995. Cratonic-margin and Antler-age foreland basin strata (Middle Devonian to Lower Carboniferous) of the southern Canadian Rocky Mountains and adjacent Plains. In: Stratigraphic Evolution of Foreland Basins. Society of Economic Paleontologists and Mineralogists Special Publication, No. 52, p. 213-231.
- Sheriff, R.E., 2006, Encyclopedic dictionary of applied geophysics: Society of Exploration Geophysicists., 13.
- Shuey, R.T., 1985, A simplification of the Zoeppritz equations: Geophysics, 50, 609-614.
- Smith, G.C. and Gidlow, P.M., 1987, Weighted stacking for rock property estimation and detection of gas: Geophys. Prosp., **35**, 993-1014.
- Stearns, D.W., and Friedman, M., 1972, Reservoirs in fractured rock, in Stratigraphic oil and gas fields: Classification, exploration methods, and case histories: American Association of Petroleum Geologists, Memoir 16, p. 82-106.

- Stearns, D.W., 1968b, "Certain Aspects of Fracture in Naturally Deformed Rocks," in NSF Advanced Science Seminar in Rock Mechanics, R. E. Rieker, Ed., Special Report, Air Force Cambridge Research Laboratories, Bedford, Massachusetts, AD 6693751, pp. 97–118
- Stearns, D.W., and M. Friedman, 1972, "Reservoirs in Fractured Rock," American Association of Petroleum Geology, Memoir 16, pp. 82–100
- Stewart, R. R., Gaiser, J. E., Brown, R. J., and Lawton, D. C., 2003: Converted-wave seismic exploration: Applications: a tutorial: Geophysics, 68, 40-59
- Torrie, J.E. 1973. Northeastern British Columbia. In: Future petroleum provinces of Canada, Canadian Society of Petroleum Geology, Memoir 1, p. 151-186.
- Varga R M., 2009, Using multicomponent seismic data to delineate hydrocarbon reservoirs: 2D-3C Willesden Green, Alberta and 3D-3C Manitou Lake, Saskatchewan: M.Sc.Thesis, University of Calgary, Department of Geoscience
- Vetrici D. G., and Stewart R. R., 1996, 3-D seismic attributes: CREWES Research Report.
- Xu R. C., and Stewart R.R, 2006, Delineating a sand channel using 3C-3D seismic data: Ross Lake heavy oilfield, Saskatchewan: CSEG Recorder, Special edition, 87-89.
- Zhang Z., 2010, Assessing attenuation, fractures, and anisotropy using logs, vertical seismic profile, and three-component seismic data: heavy oilfield and potash mining examples: Ph.D Thesis, University of Calgary, Department of Geoscience